STUDIES ON GRAPHENE-PEROVSKITE $LaFeO_3$ INTERFACE

Thesis submitted to the
University of Calicut for the partial fulfillment of
the requirements for the award of the degree of

DOCTOR OF PHILOSOPHY IN PHYSICS

Under the Faculty of Science

by

VIDYARAJAN N.

DEPARTMENT OF PHYSICS
UNIVERSITY OF CALICUT
KERALA, INDIA 673 635

OCTOBER 2018

STUDIES ON GRAPHENE-PEROVSKITE $LaFeO_3$ INTERFACE

Ph.D. Thesis in Physics

Author:

VIDYARAJAN N.
Department of Physics
University of Calicut
Calicut University (PO) – 673635, Kerala, India.
Email: vidyarajan1206@gmail.com

Under the guidance of

Dr. Libu K. Alexander
Assistant Professor
Department of Physics
University of Calicut
Calicut University (PO) – 673635, Kerala, India.
Email: lka@uoc.ac.in

UNIVERSITY OF CALICUT
DEPARTMENT OF PHYSICS

Dr. LIBU K. ALEXANDER
Assistant professor
Department of Physics

Calicut University P.O
Kerala, India. 673 635
Tel: 0494-2407416(O)
+919446376861(M)
email: lka@uoc.ac.in

CERTIFICATE

Certified that the work presented in the thesis, entitled **''STUDIES ON GRAPHENE-PEROVSKITE $LaFeO_3$ INTERFACE''** is based on the authentic record of research carried out by **Mrs. Vidyarajan N.** under my guidance in the Department of Physics, University of Calicut, Calicut University P.O, Kerala-673635 and this work has not been included in any other thesis submitted previously for the award of any degree.

Calicut University
31 October 2018

Dr. Libu K. Alexander

UNIVERSITY OF CALICUT
DEPARTMENT OF PHYSICS

Dr. LIBU K. ALEXANDER
Assistant professor
Department of Physics

Calicut University P.O
Kerala, India. 673 635
Tel: 0494-2407416(O)
+919446376861(M)
email: lka@uoc.ac.in

CERTIFICATE

Certified that the work presented in the thesis, entitled " STUDIES ON GRAPHENE-PEROVSKITE LaFeO3 INTERFACE" is based on the authentic record of research carried out by Ms. Vidyarajan N. under my guidance in the epartment of Physics, University of Calicut,Calciut university P.O. Kerala-673635 and this work has not been included in any other thesis submitted previously for the award of any degree. Also certified that the corrections suggested by the adjudicators have been incorporated in this revised thesis.

Calicut University
20 July 2019

Dr. Libu K.Alexander

DECLARATION

Certified that the work presented in this thesis, entitled **''STUDIES ON GRAPHENE-PEROVSKITE $LaFeO_3$ INTERFACE''** is based on the original research work done by me under the supervision and guidance of Dr. Libu K. Alexander, Assistant professor, Department of physics, University of Calicut, University P.O, Kerala-673635 and has not been included in any other thesis submitted previously for the award of any degree.

Calicut University
31 October 2018

Vidyarajan N.

ACKNOWLEDGEMENT

I owe my deepest sense of gratitude to my mentor Dr. Libu K .Alexander, Assistant Professor, Department of Physics, University of Calicut, Kerala , India for accepting me as part of his group and introducing me to this wonderful area of research. He is always patient, supportive, insightful and inspiring to me. He is a man who is completely dedicated for excellence. Dr. Libu K. Alexander is also worth special thanks for providing a research environment which promotes independent thought and creativity. I am really indebted for his invaluable suggestions, advice and support throughout my Ph. D. work which helped me to improve my skill sets and ability to think creatively. I would like to thank him for making my dreams come true.

I would like to give a special thanks to the head of the Department, Prof. (Dr.) P P Pradyumnan for his substantial support and cooperation both as a HOD and as an eminent material scientist. I am also thankful to all the former heads of the Department, the research advisory committee members and other faculty members of the Department of Physics for their valuable suggestions and support during my research period.

I would like to thank Prof (Dr.) Abraham Joseph, Dean of faculty of science for giving me the permission to work on his electrochemical workstation. I express my gratitude to Dr. T.N Narayanan (TIFR- Hyderabad) for gas sensing measurements and Dr. Sivadasan (IGCAR-Kalpakkam) for his valuable suggestion regarding Raman measurements and analysis.

I am really content to thank my lab mates Dr. Ahammed Raseen Nanakkal, Bintu Thomas, Anju K, Sravandas P, and Geeshpath G K for their valuable support and cooperation which helped widely in my academic fields during my Ph.D. I acknowledge with gratitude, the researchers Anju Paulson, Muhammed Sabeer, Jemshihas, Shabeeba and all the non- teaching staffs in the Department of physics. I am in debt to Anupama R Prasad, Department of Chemistry for her support during my electrochemical measurements.

I am much fortunate to have a friend like Usha K. and Dr. Anand P.B. (Rice University, USA) for being with me through thick and thin. Thanking Sreepriya M.K, for the cherished moment that we shared in the campus and Hostel.

I express my sincere thanks to UGC - SAP (BSR-RFSMS) for granting me fellowship during my Ph.D. period. I also thank FIST for assisting Department projects. I acknowledge INUP at CENSE IISC Bangalore for characterizations.

I express my sincere gratitude to my family members for their constant support throughout my life.

Vidyarajan N.

CONTENTS

LIST OF TABLES

LIST OF FIGURES

ABBREVIATIONS USED IN THE THESIS

CNT	:	Carbon nanotube
CV	:	Cyclic Voltammetry
CVD	:	Chemical vapour deposition
DPV	:	Differential Pulse Voltammetry
E_U	:	Urbach energy
GLFAL	:	Graphene-$LaFe_{0.8}Al_{0.2}O_3$ nanocomposite
GLFCR	:	Graphene-$LaFe_{0.8}Cr_{0.2}O_3$ nanocomposite
GLFO	:	Graphene-$LaFeO_3$ nanocomposite
GLFO-1	:	Graphene-$LaFeO_3$ nanocomposite with GO to LFO ratio 1:10
GLFO-5	:	Graphene-$LaFeO_3$ nanocomposite with GO to LFO ratio 5:10
GLFO-10	:	Graphene-$LaFeO_3$ nanocomposite with GO to LFO ratio 10:10
GO	:	Graphene oxide
MWCNT	:	Multi-walled carbon nanotube
NIR	:	Near infrared
ORR	:	Oxygen reduction reaction
RGO	:	Reduced graphene oxide
RhB	:	Rhodamine B
UV	:	Ultraviolet
Vis	:	Visible

PUBLICATIONS

1. **N. Vidyarajan**, L. K. Alexander, "Strain induced optical properties of perovskite $LaFeO_3$". *Material Research Express 6(2019) 015610, IOP publishing*: DOI:10.1088/2053-1591/aae857.
2. **N. Vidyarajan**, L. K. Alexander "Electrochemical sensing of modified ABO_3 perovskite: $LaFe_{0.8}$ $R_{0.2}O_3$ (R= Cr, Co, Al)". AIP Conference Proceedings 1849, 020027 (2017); DOI: 10.1063/1.4984174.
3. **N. Vidyarajan**, L. K. Alexander, Abraham Joseph. "Interface with reduced graphene oxide as a non-invasive platform for inducing distortion in orthorhombic perovskite" (Under review-arXiv:1808.04105 [cond-mat])
4. A.R Nanakkal, **Vidyarajan N**. and L.K. Alexander, Electrolytic syntheis and characterization of graphene-Cu_2O nanocomposite, Proceedings book: ISBN 81-86366-88-1(KSCSTE)

International/National Conferences

1. Third International Conference on Nanomaterials: Synthesis, Characterisation, and Applications "ICN 2018" May 11-05-2018 at M G University, Kottayam. Paper presented on the topic "Low temperature gas sensing properties of reduced graphene oxide incorporated perovskite nanocomposite".
2. Three days Golden Jubilee National seminar on Science and Technology New materials for a sustainable future (STNM 2018), Feb 7-9, 2018. Paper presented on the topic "Reduced graphene oxide induced strain effect on perovskite$LaFeO_3$".

3. 29th Kerala Science Congress at Marthoma College-Tiruvalla. Paper presented in the category of " Best paper Contest" on the topic- Temperature shielding effect of ZnO nanoparticle on different roofing materials, Vidyarajan N., L.K.Alexander, Ajith M.C.
4. A conference on light-OPTICS'-2017, NIT Calicut–Paper presented on the topic "Electrochemical sensing of modified ABO_3 perovskite: $LaFe_{0.8}R_{0.2}O_3$(R= Cr, Co, Al)".
5. INUP IISE Bangalore- Hands own training –October-2014.
6. 2nd IEEE International Conference on Emerging Electronics: Indian Institute of Science, Bangalore, December 3-6, 2014
7. National seminar on "Interaction programme for Ph.D. Scholars" conducted by Academic Staff College, University of Calicut from 13-03-2013 to 19-03-2013.
8. National Workshop on 'Spectroscopic techniques and Instrumentation' organized by Physics Department and Nanoscience Department, NIT-Calicut.

UNIVERSITY OF CALICUT
DEPARTMENT OF PHYSICS

Dr. LIBU K. ALEXANDER
Assistant professor
Department of Physics

Calicut University P.O
Kerala, India. 673 635
Tel: 0494-2407416(O)
+919446376861(M)
email: lka@uoc.ac.in

CERTIFICATE

Certified that the work presented in the thesis, entitled " STUDIES ON GRAPHENE-PEROVSKITE LaFeO3 INTERFACE" is based on the authentic record of research carried out by Ms. Vidyarajan N. under my guidance in the epartment of Physics, University of Calicut,Calciut university P.O. Kerala-673635 and this work has not been included in any other thesis submitted previously for the award of any degree. Also certified that the corrections suggested by the adjudicators have been incorporated in this revised thesis.

Calicut University
20 July 2019

Dr. Libu K.Alexander

CHAPTER 1

INTRODUCTION

This chapter discusses a general introduction to perovskite, graphene and graphene nanocomposite. The motivation, objective of the study and an overview of the experimental work are also discussed in this chapter.

1.1 Overview of Perovskite Nanomaterials

The rapid development of technology in diverse fields such as optoelectronics, microelectronics, photonics, and catalysis has led to the discovery and development of many novel materials [1,2]. In the case of nanomaterials, predictions and formulation of a steady state structure which exhibits stable physical and chemical properties is a daunting problem. But there are stable structures, which are amenable to chemical substitutions and form a sphere of technologically transformative materials such as perovskites, spinels, and garnet etc. These adaptable frameworks have an important role in the discovery of new materials for functional applications. In the aforementioned crystals, the properties can be varied by elemental substitution method which gives an insight into the structure-function relations. Among fascinating mineral crystals, perovskite earned the distinction of "chemical chameleons".

The perovskite based homologue series like Ruddlesden-Popper ($A_{n+1}B_nO_{3n+1}$), Dion-Jacobson ($A_nB_nO_{3n+1}$), and Aurivillius ($Bi_2A_{n-1}B_nO_{3n+3}$) etc can form numerous oxide compounds [3–5]. Depending on the stoichiometry of the constituent atoms perovskite can exist in different forms such as ABO_3, A_2BO_4-layered perovskite, $A_2BB'O_6$ double perovskite, and $A_2A'B_2B'O_9$ triple perovskite. These perovskites can accommodate over 50% of the elements in its lattice sites. In general ABX_3 formula, *A* and *B* represent metal cations and *X* represents the anions. *A*-site cations are usually bigger and more electropositive than one located at *B*-site, while the *X*-site is commonly occupied by oxide (O_2^-) or halides (Cl^-, Br^-, F^-) [6]. During the past few years, many efforts have been made on the experimental and theoretical investigations on perovskite solids especially in ABO_3 class.

The typical crystal structure of perovskite oxide is cubic in nature where *A* cation is located in between eight BO_6 octahedra, while *B* site atom is

surrounded by 6-fold coordination by oxygen atoms. The co-substitution at the three sites provides opportunity to discover new phases with a variety of composition as well as structural diversity. The structural stability of a perovskite is expressed in terms of tolerance factor (τ), which gives the relation using ionic radii of cations (r_A,r_B) and anions (r_O) and expressed as $\tau = \frac{(r_A+r_O)}{\sqrt{2}(r_B+r_O)}$. The ideal cubic structure has $\tau = 1$, where $\tau < 1$ shows orthorhombic structure and $\tau > 1$ represent the tetragonal shape. Structural diversity mainly arises due to the distortion in the crystal structure by octahedral tilting or Jahn-Teller effect. The Physicochemcial peroperties of perovkite materials are dependent on the crystal structure, defect on the lattice, exposed lattice plane morphology, size of the particle, pore size distribution and surface area [7,8] .

Nowadays hybrid perovskites are synthesized in an attempt to combine positive properties of both inorganic (electron mobility) and organic materials (photoresistivity) into a single component. The general formula of a hybrid perovskite is $(R\mathrm{NH_3})_2BX_4$, where *B* site is occupied with divalent cations, *R* is the organic part and *X* is halogen. Instead of single layer perovskite, it is possible to synthesize hybrid perovskite with different layer orientations by controlling the crystallization process. It can also be derived from the layers of three dimensional ABX_3 structure [9]. Currently, perovskite plays an important role in many modern applications. Lead-based organohalide is considered to be a promising material in solution based solar cells [10]. Various perovskite applications include sensors, catalysis, electrodes, solar cells, lasers, fuel cells and spintronics [11].

The structural properties of the perovskite are greatly influenced by the synthesis techniques. In addition to the generally used solid state reaction methods, several wet chemical methods were also introduced to improve the homogeneity as well as to reduce the preparation temperature [12]. The

detailed description on fabrication of perovskite nanomaterials is discussed in Chapter-3.

1.2 Properties of Perovskite Materials

Perovskite materials, especially in the class of ABO_3 exhibit some interesting properties which include ferroelectricity, ferromagnetism, superconductivity, thermal conductivity, fluorescence, and high temperature thermoelectric power.

1.2.1 Magnetic Properties

In an ideal cubic perovskite structure, the *B* site atom is surrounded by oxygen atoms and forms a *B-O-B* angle such that this configuration favors superexchange interactions between magnetic B^{3+} ions. The *B-O-B* arrangement usually leads to the antiparallel coupling of the nearest neighbour magnetic moment. In $A_2BB'O_6$, the *B* atoms are in two sub lattice, in such condition spin arrangement will differ. If *B*'atom is diamagnetic B^{3+} can align antiferromagnetically and a longer range superexchange interaction through *B-O-B'-O-B* occurs.

The $LnFeO_3$ (Ln=Lanthanides) are widely used as a technologically important magnetic material. A slight canting in the magnetic moment of iron can cause a weak spontaneous magnetic moment to the system. If it is not present, the compound shows antiferromagnetic nature. For an orthorhombic cell, the easy magnetization is along *a* or *c* axis in the crystal structure and helps us to use this in memory device application [13]. In the case of $LnMnO_3$, the material is generally showing antiferromagnetic nature but the concentration of Mn^{4+} in the range of 25 % to 30% shows ferromagnetic behavior. In $LnMnO_3$, three kind of interactions are possible (1) Between Mn^{3+} a very weak interaction exists (2) A negative interaction is happening among Mn^{4+} (3) A strong positive interaction is possible between Mn^{3+} and

Mn^{4+} . A similar kind of trend is observed among Co^{3+} and Co^{4+}. If the *B* site atom is Cr or Fe, it shows antiferromagnetic nature.

1.2.2 Electrical Properties

Rare-earth ortho perovskite containing transition metals show a wide variety of electrical properties. The collective d-electron behavior in $LaNiO_3$ and $LaTiO_3$ shows a metallic conductivity whereas, $LnCrO_3$ (Lanthanide chromite series) shows a semiconducting nature. In the chromite series, the conductivity has two regions, at low temperature, the activation energy increases along the rare-earth series. At high temperature the value is found to be a constant (0.23 eV). In $LaMnO_3$, conductivity is a function of temperature. In the vicinity of 720 K, it shows an abrupt change in conductivity as well as magnetic susceptibility. In the case of $LaCoO_3$, the electrical conductance is bit complex. It shows a variety of conductive behavior in different temperature region. Upto 400 K, $LaCoO_3$ is a semiconductor whereas, a rapid increase in conductivity is observed till 823 K. A region between 823 K to 1200 K shows a flat maximum and above 1200 K the compound behavior transformed to metallic in nature. A similar trend is observed in Sr-doped cobaltite. The variation in conductivity is associated with the change in oxidation state of the *B* site ions in the crystal structure.

1.2.3 Optical Properties

Perovskites are used as a model system for the studies in UV-Vis-NIR region. From the optical studies, magnetic ordering in the *B* site atom along with the rare earth ion can be evaluated [14]. Varying the optical properties of *B* site atom with partially filled or completely empty d-orbitals are widely explored. $SrTiO_3$ with empty d-band shows a luminescence spectrum which is independent of synthesis condition and contamination. The emission peak is centered at 500 nm with stock shift about 7000 cm^{-1}. The energy band

formation is due to the corner sharing of titanate octahedra which decreases the first absorption transition energy and in the excited state, the titanate becomes mobile. This condition can be explained on the basis of free and delocalized excitons. The absorption characteristics of $CaTiO_3$ are similar to that of $SrTiO_3$ with a shift of absorption to higher wavelength [15]. Depending on temperature the electro-optical coefficients of $KaTaO_3$, $BaTiO_3$, and $SrTiO_3$ are constant. The properties of $BaTiO_3$ and $SrTiO_3$ are applied in infrared windows.

In recent years, luminescent properties of the perovskites were extensively studied. They are considered to be a good candidate for field emission displays (FED) and plasma display panels (PDP) [16,17]. Rare-earth doped phosphors are widely studied and some of them are used in displays. The low cost environment friendly $BaZrO_3$ shows photoluminescence in the visible region. The optical properties make perovskite material a promising candidate in green photocatalysis, solid-state lightning, and in optoelectronic applications.

The other properties of perovskite like colossal magnetoresistance, dielectric properties, superconductivity, piezoelectricity, and ferroelectricity are also extensively reported [16].

1.3 Application of Perovskite Nanomaterials

1.3.1 Electrochemical Applications

The efficient energy storage devices became a priority in the real world where energy shortage is a major problem. The hybrid properties of conventional capacitors as well as batteries, supercapacitors ensure environmental protection and can be used in portable electronics. Due to the unique structure and physicochemical properties, perovskite is used as efficient energy conversion materials in metal-air batteries, hybrid solar cells, fuel cells

etc. Eska *et al.* reported that the energy stored in perovskite supercapacitors are mainly due to valency change in B site atom by the absorption of hydrogen in the form of protons [18]. Moreover, the number of valence state, high discharge capacity, as well as electrochemical activity of Fe, makes it to be a good candidate for the electrode. Zijiong Li *et al.* reports electrochemical properties of tubular $LaFeO_3$ with a specific capacitance of 313.21 Fg^{-1} at a current density of 0.8 Ag^{-1}. It shows the reduction of specific capacitance upto 13.9% after 5000 cycles [12]. Henao *et al.* report the electrochemical activity of a layered $La_2Ti_2O_7$ perovskite as a negative electrode in Ni/Oxide rechargeable batteries. It reports maximum hydrogen intake capacity as 224 $mAhg^{-1}$ [19]. Different lanthanide composites were investigated for application as effective electrode material for the batteries. Kaabi *et al.* used the perovskite $LaGaO_3$ as a secondary electrode in Ni-MH batteries with a discharge capacity of 220 $mAhg^{-1}$ [20]. Yuan *et al.* report the electrochemical activity of $LaFeO_3$- RGO nanocomposite with improved electrical conductivity. Compared to pure $LaFeO_3$, the composite showed an enhanced electrochemical activity. The maximum discharge characteristics showed a variation from 209.5 mAh g^{-1} to 334.6 $mAhg^{-1}$ [21].

1.3.2 Catalytic Application

Catalysis helps to address some of the societal and environmental issues, like reduction of fossil fuels emission and production of sustainable chemicals and fuels. In reaction pathways catalyst stabilizes the reaction intermediates. Catalyst reduces the energy barrier of the transition state and speeds up the reaction between two intermediates. Noble metals are widely studied as a catalyst in many applications. But the search for an abundant as well as low cost material ends up in perovskite nanomaterials. Perovskites are widely using in the reactions of oxidation of toxic gases, reduction of NO_x, air purification, and electrolysis for the generation of sustainable fuels [22]. The reactions which can be mediated through perovskite includes, oxidation of small molecules CO, hydrocarbons, NO_x, H_2 production from

photoelectrochemical splitting of water, reduction of CO_2, N_2, and O_2 [23,24]. The chemical versatility, flexibility in the crystal as well as electronic structure, enables perovskite to be a good, selective, stable, and highly active catalyst for chemical reactions. As an efficient photocatalyst for water splitting application, $SrTiO_3$ doped with Ru, Rh and Ir with Pt cocatalyst is used. Chen *et al.* reported the Cu doped ABO_3 as a visible light driven photocatalyst for H_2 production [25]. Kudo *et al.* fabricated a series of co-doped $SrTiO_3$ with a combination of Cr, Sb, Ta, and Ni for the visible light driven photocatalysis for H_2 production [26,27]. There are several other reports on perovskite combinations which show an enhanced yield of H_2 from water splitting, methanol oxidation *etc*. Acharya *et al.* report the effective usage of graphene in $LaFeO_3$-RGO nanocomposite for the generation of H_2 from water splitting reaction [28].

1.3.3 Optoelectronic Applications

Perovskite materials became a promising candidate in potentially portable and efficient optoelectronic devices. Hybrid organic-inorganic perovskite material with ABX_3 structural formula emerged as a revolutionary class in light harvesting material. Here *A* is monovalent ion (methylammonium ion, Cs, or formamidinium) *B* is divalent metal cation and *X* is halide. In the case of solar cells, power efficiency of perovskite, device is increased to more than 22%. This property is obtained with a device formed out of solution process method. Kojima *et al.* developed a solar cell based on $MAPbX_3/TiO_2$ using lithium halide and halogen as redox reagents and achieved 3.13% and 3.81% efficiency for X= Br and I respectively [29]. The hybrid perovskites are mostly used in light emitting diodes, photodetectors, and laser applications. Mali *et al*. report the efficiency of 11.46% for $MAPbBr_3$ with different sizes using poly triarylamine a high hole mobility polymer[30]. Inorganic perovskite shows excellent lasing action with a lower lasing threshold. The large absorption coefficient, long carrier diffusion length, higher gain cross-section, and slow radioactive decay makes perovskite a good optical gain –

media for lasing application. Xing *et al.* report that a high lasing threshold of 20, 60, 11 $\mu J/cm^2$ for $MAPbBr_3$, $MAPbIxCl_{3-x}$, $MAPbI_3$ perovskite, and a tunable lasing wavelength is due to the Fabry-Perot mode cavities in the nano wire structure of perovskite [31].

Perovskites are really an efficient material for many applications. But some of its inherent properties such as low intrinsic current, photocorrosion, poor lifetime and agglomeration during charge-discharge analysis etc limit its utility to an extent. In order to overcome the problems, one of the methods is to modify the perovskite with a highly active material. Here the active material chosen is a carbon derivative such as graphene.

1.4 Overview of Graphene

The search for various allotropes of carbon with altering dimensionalities has led to numerous interdisciplinary applications [32]. Graphite is the most common form of carbon, which consists of stacked layers in a hexagonal structure mediated by van der Waal forces. Fullerene - a combination of 60 carbon atoms arranged in 20 hexagons and 12 pentagons form spherical in shape - was discovered by Kroto and his co-workers in 1985. The quasi-one-dimensional form of carbon is carbon nanotube (CNT) which is isolated by Iijima in 1991 [33]. Graphene is made up of carbon atoms bound together in a network of repeating hexagons within a single plane just one atom thick [34]. Among these carbon allotropes, graphene have achieved a great level of attention for its interesting properties. Graphene is the first example of 2D atomic crystals. In 2004 Novoselov and Geim of Manchester University UK, isolated graphene using scotch-tape method and this ground breaking experiment is honored with Nobel prize in physics in 2010 [1]. Literary, graphene is the mother of all other graphitic materials with different dimensionalities. A graphene sheet can be rolled to form carbon nanotube, wrapped to form fullerene and 3-D stacking to form graphite (Fig. 1.1) [35]. Graphene became a super material due to its unique physical properties. The electronic structure of graphene is different from the usual 3-D materials.

Long-range π-conjugation in the structure made graphene an attractive material for theoretical as well as experimental studies. It is the thinnest and the strongest material ever measured. Excellent electrical, thermal, mechanical, electronic and optical properties enable graphene distinctly different from all other carbon allotropes [36]. In the field of research, graphene experiences a boundless growth and it is heralded as the next-generation material for nanoelectronics devices due to its tremendous electronic characteristics [37]. Electrons in graphene behave like massless relativistic particles which obey a linear dispersion relation resulting in peculiar electronic properties. The graphene-based electronic platform can potentially transform post complementary metal oxide semiconducting electronics because of its unprecedented high carrier mobility (200000 cm^2/V s), high thermal conductivity and electrical conductivity [38].

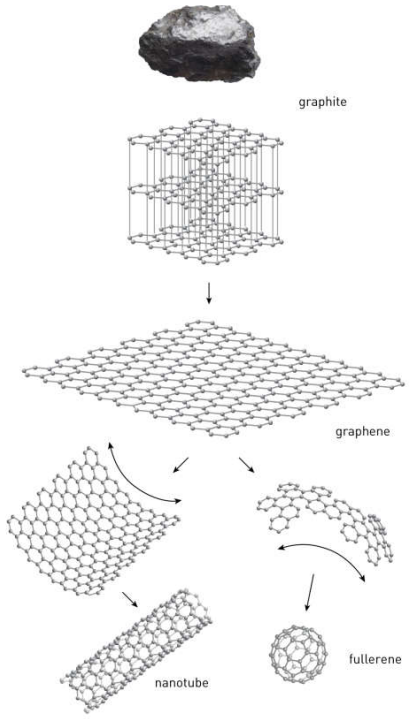

Fig. 1.1 Schematic representation of different allotropes of carbon derived from the extended honeycomb lattice structure. The image is adapted from [39]

Graphene is also used in the field of energy storage applications where a large surface area is needed for long-lasting batteries. In optoelectronic applications like solar cells and transparent conducting displays, graphene is used as an electron trapper as well as a channel for charge carriers. Application of graphene is diversified in the fields of corrosion prevention, circuit boards, medicinal technologies, water purification, and decomposition, capacitors, high-speed and radio frequency logic devices, electrochemical sensors, thermally and electrically conductive reinforced composites etc [40–43].

Graphene is usually produced as a mixture of monolayers, bi-layers, and multilayers [44]. The common techniques employed for the synthesis of graphene includes mechanical exfoliation of graphite [45], epitaxial growth by chemical vapour deposition (CVD) [46], thermal decomposition of SiC [47], wet chemical synthesis from graphite particles, liquid phase exfoliation, electrochemical approach and oxidation of graphite and so on [44,48,49]. Graphene and chemically modified graphene can be obtained from colloidal suspensions made out of graphite and derivatives of graphite (e.g. GO) respectively. The chemical method is considered to be useful and well suited four chemical functionalisation due to the possibility of versatility and high volume production [50].

1.5 Graphene Oxide

The research in the area of graphene related and graphene-like materials are also increased tremendously. The graphene derivatisations tailor their properties like resistivity, electronic structure, optical transparency, luminescence, surface energy and magnetic properties for different applications. There are number of materials which are known as derivatives of graphene such as Graphane, Fluorinated graphene (Fluorographene), Graphene oxide (GO), Graphyne and graphdiyne. Among these materials

graphene oxide is generally used as a precursor for the preparation of chemically modified graphene/ reduced graphene oxide. Graphene oxide is a single layer of graphite oxide formed from the oxidation of graphite. It is used as the potential starting material for the synthesis of graphene. It can be considered as the compound with a large number of oxygen species (C/O ratio ~ 2) in various bonding conditions such as epoxy, hydroxyl, carbonyl, and carboxyl groups. The degree of oxidation determines the nature of graphene oxide (varying the nature from semiconductor to an insulator), optical, and electronic properties [51–54]. Reduction of graphene oxide restores the sp^2 C-C bond by removing oxygen functional groups and forms more or less pristine graphene. Tuning of graphene oxide properties is mainly targeted on its chemical structure, reduction reaction time, electronic structures, and chemical functionalization [55].

The main advantage of graphene oxide is the hydrophilicity, which makes a stable solution in polar as well as other organic solvents. The surface moieties reduce the platelet-platelet interaction and make it hydrophilic which differentiate GO from other non-oxidized counterpart of 2D material [56]. GO has been used as a host matrix for the intercalation of other linear molecule. The exhibited properties of GO is based on the structure of the compound. There are several models of GO proposed by Hoffman, Ruess, Scholz-Boehm, and Nakajima-Matsuo. But the widely used model is proposed by Anton Lerf and Jacek Klinowski [57,58]. Fig. 1.2 shows different models of GO.

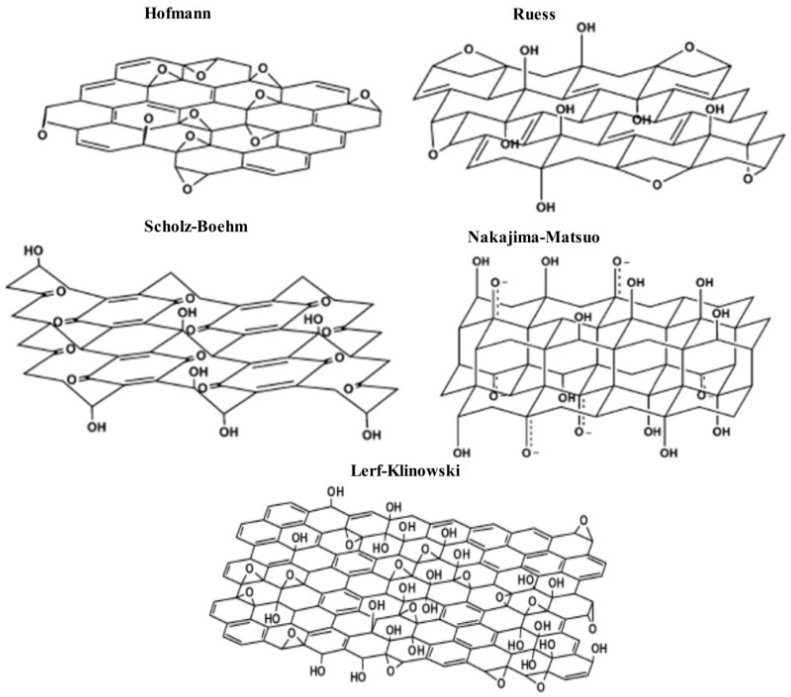

Fig. 1.2 Structural models of GO: image adapted from [58]

Surface functional groups on GO act as anchoring sites which immobilize the functionalised nanomaterials. GO acts as an insulator with a sheet resistance of the order of 10^{12} Ωsq^{-1} [59]. By varying the extent of oxidation and sheet thickness, the optical properties of GO can be controlled. The optical absorption of GO mainly arise due to the π-π^* transitions [60,61]. The intrinsic strength and Young's modulus shows a range of 76-293 MPa and 6-42 GPa respectively [62].

Widely used method for the preparation of GO is proposed by Hummer and Offman, which is derived from Staudenmaier method. The oxidation followed by reduction yields chemically modified graphene in large amount compared to other techniques. This method has a drawback. The harsh environment for the production of GO disrupt the conjugation of graphene and an additional step is needed to revert it back to graphene form,

though it could not be fully accomplished. Fortunately, the oxygenated functional groups expand the structure / chemical diversity of GO by extending it to further modification which effectively tailors the physical and chemical properties. As a consequence, GO and GO-based composites have potential applications in the field of energy storage, environmental protection and electrochemical applications [63].

1.6 Graphene–Nanocomposites

The motivation for the studies in graphene-nanocomposite is the desire to apply the favorable properties of graphene with another dispersing matrix (second phase) [64,65]. The main advantage of composite formation is that it utilises the unique properties of the individual components for enhancement of the property of composite and makes it useful for further applications. The graphene is used for the formation of nanocomposite because of the following properties [66].

1. Planar structure: Comparing to other graphite allotropes, graphene has the basal planar structure, which enables to load nanomaterials in the range or larger than the diameter of carbon nanotube (CNT) [67].

2. High surface area: Higher surface area improves the interfacial contact with other dispersing medium and thus prevents the aggregation of the secondary phase. However, the large surface area of graphene sheet tends to form irreversible aggregates, but the nanomaterials act as the spacers between the graphene sheets and resist the aggregation [68–70].

3. Electrical properties: As a zero band gap material, the charge carrier mobility of graphene is reported to be 15000 $cm^2V^{-1}s^{-1}$ [71] and it is nearly independent of temperature. This is very important in the case of nanocomposite, where graphene is used as an electron carrier.

Graphene can perform better in the application that involves charge transfer processes e.g. sensors, supercapacitors, and electrocatalysis *etc*.

4. Optical properties: Transparent conductive films made out of graphene nanocomposite effectively utilize the optical as well as electronic properties of graphene. Graphene based transparent conductive films have an application in the field of solar cells, optoelectronics, and other advanced electronics [72,73].

5. Thermal properties: Thermal conductivity measured by non-contact confocal micro Raman analysis shows a value of 5000 $Wm^{-1}K^{-1}$ for a free-standing graphene sheet [74]. The high thermal conductivity of graphene nanocomposite is important in the field of electronic devices or catalytic reactions, where heat release is a major problem e.g. lithium-ion batteries, fuel cells etc.

6. Mechanical properties: It is reported that defect-free graphene has Young's modulus of 1.0TPa and fracture strength of 130GPa. Jeon *et al*. report that Au decorated graphene sheets show an enhanced mechanical stability in the form of composite and retain its property under the thermal and mechanical fluctuations [75].

7. Low cost procedure for the production: Graphene and its derivatives can readily form stable colloidal solution in various solvents. This enables to use graphene directly for the applications through solution processing technique. Also, solution processing method uses graphite as the raw material, so production cost for the graphene nanocomposite in large quantities can be reduced.

1.7 Application of Graphene Nanocomposites

Due to the synergetic effect between dispersing phase and matrix, graphene nanocomposites preserve the intrinsic as well as favourable properties of the individual components. Some of the important applications of graphene nanocomposite are as follows.

1.7.1 Catalysis

Graphene nanocomposites have been used as an active catalyst in chemical, electrochemical as well as photochemical reactions. Cross-coupling (C-C) reactions have been widely employed in the synthesis of organic polymers, which has applications in the chemical and pharmaceutical industries. Graphene incorporated nanocomposites provide significant advances in C-C chemistry. Noble metal loaded graphene nanocomposites show enhanced catalytic activity, selectivity, and recyclability. Mulhaupt *et al.* reported the catalytic activity of RGO-Pd nanocomposite with turnover frequency 39000 hr^{-1} and < 1ppm leaching of Pd in Suzuki-Miyaura coupling reactions [76]. Wang *et al.* used GO-Pd catalyst for the Heck reactions. In which both selectivity and conversion were reported to be 100% when K_2CO_3 was used as the base in the reaction between iodobenzene and methyl acrylate [77]. Graphene nanocomposites are also used in many environmental protection reactions and energy conversion reactions e.g oxygen reduction reactions (ORR), water splitting, Fischer−Tropsch synthesis (FTS), CO_2 reduction, water treatment, and air purification. Li *et al*. report PtM (Ni, Co)/RGO nanocomposite for ORR. The authors claim that the interaction with PtM with RGO is the reason for enhanced activity of the material [78]. Fu *et al.* reports that porous and nonporous carbon nanofiber along with graphene-Pt (Pt/G-PCNF) is a better candidate for ORR. Compared to commercially available Pt/C (JM20) catalyst, Pt/G-PCNF shows higher onset potential of 38 mV, twice higher mass activity (0.8V) and better stability. One dimensional PCNF and 2D graphene act as a spacer in which

high intrinsic surface area of graphene is fully utilised for the reactions which result in higher activity of the composite [79]. Wide reports on nitrogen (N) boron (B) sulfur (S), selenium (Se), halogen, Ag/N-RGO, nitrogen-doped graphene, N-P-RGO etc show a better catalytic activity than commercially available ones [80–85].

For the environmental applications like CO_2 reduction, graphene incorporated nanocomposites are used. Combination of CuO-ZnO-ZrO_2−Al_2O_3/RGO (CZZA/RGO) shows a high yield of methanol by the reduction reaction of CO_2. Large surface area, high H_2 and CO_2 adsorption on the surface of RGO lead to the higher activity of the composite [86]. Li *et al.* report the selective reduction reaction of CO_2 to ethylene C_2H_4 over Cu decorated pyridinic-N rich graphene (p-NG). The detailed description about the role of each component in the composites shows that p-NG could catalyze CO_2 reduction to formate, however combining with Cu, p-NG serve as an absorber of CO_2 and proton. This facilitates hydrogenation and C-C reactions for the formation of C_2H_4 [87].

Owing to the high surface area and electron mobility, graphene is considered to be a high quality support for the application as a channel. Graphene restricts the recombination of electrons and holes in the photocatalytic activity studies. In the application of photo activated catalysis, graphene handles the role as an electron acceptor, electron transporter, co-catalyst, photocatalyst etc [88]. Graphene nanocomposites as photocatalysts are widely explored. A.R. Nanakkal *et al.* utilized the properties of RGO for tuning the band gap and prevent the recombination of photoexcited electrons in $BiVO_4$ [89]. Also, H_2 production from water splitting under visible light irradiation has been achieved by graphene nanocomposites [90].

1.7.2 Energy Storage and Conversion

Graphene based materials have been explored as a promising alternative for electrode materials in energy-related devices. Superior electrical conductivity, high surface area, chemical stability, mechanical strength, thermal conductivity, and broad electrochemical window enables graphene based materials for energy storing applications [66]. The specific capacitance of graphene in the aqueous electrolyte is reported to be 135 Fg^{-1}. But the agglomeration of graphene nanosheets prevents the usage of pristine graphene in many applications. Incorporation of metal oxide not only prevents the aggregation but also contributes an additional pseudo-capacitance to the graphene composites increasing the supercapacitance. By far, a wide range of metal compounds has been investigated for the supercapacitor application which contains, ZnO, Mn_3O_4, MnO_2, Co_3O_4, SnO_2, NiO, CeO_2, $NiCo_2O_4$, RuO_2. $Co(OH)_2$, Fe_3O_4, Bi_2O_3 *etc.* [91–102].

Due to the large surface to volume ratio and high conductive nature, graphene possesses high lithium storage capacity. Using graphene nanocomposite, one can utilize the maximum surface area available for the energy storage. A wide range of nanomaterials of oxides, halogens, and chalcogenides, like SnSe, CuO, $LiTi_5O_{12}$, $Co(OH)_2$, Mn_3O_4 ,CoO, *etc*. have been anchored on graphene sheets for the application as anode material for LIBs [103–109].

1.7.3 Sensors

Rapid development in graphene research paved the way for the progress of analytical science. The large surface area, high carrier mobility, and conductivity of graphene implanted novel functions into analytical sensing systems. Graphene and its derivatives are widely using as gas sensors, electrochemical sensors, and biological sensors. Among difference gas sensors, graphene based gas sensors have intensively studied due to its rapid and selective detection. But the challenge

includes the relatively weak and unstable sensing response of pristine graphene. In order to overcome the limitations of graphene as a sensor, the nanomaterials like Pt, Pd, PtPd alloy, ZnO, ZnS, SnO_2 were incorporated for the detection of H_2, H_2S, ethanol, propanol, NO_2, and CO [90,110–112].

Special configuration, ballistic electron conductivity, number and positions of oxygen moieties etc help to accelerate and promote electron during electrochemical detection. Because of the rapid electron transfer kinetics at the basal plane, graphene acts as a nanoconnector between the analyte and the electrode surface which results in good sensing experience. Wang *et al.* fabricated flower like RGO for the detection of dopamine. It showed higher activity than multi-walled carbon nanotube (MWCNT) and a good selectivity for dopamine among interference materials like Ascorbic acid and Urea [113]. Literature shows number of research works where graphene nanocomposites are used to detect various water pollutant heavy metals (arsenic, lead, and Cr), biomolecules (neuron transmitter dopamine, H_2O_2, glucose, ascorbic acid, uric acid, proteins, histidine, pestidine, NADH, cholesterol) and ammonium etc using electrochemical sensing mechanism, [114–120]. Many of the biosensors were using the electrochemical techniques like amperometry, voltammetry and electrochemiluminescence for the detection processes.

1.7.4 Optical Applications

The transparent conductive electrodes (TCE) are important in modern optoelectronic devices. Graphene has an important role in the formation of thin film electrodes for TCE applications. Wide surface area, electrical conductivity with optical transparency leads to the applications of graphene related materials in optoelectronic applications. Photodetector application utilizes the high charge mobility and a short lifetime of carriers in graphene for high frequency, ultrafast photodetection. But for pristine graphene the photoresistivity is low, so in order to improve the resistivity, several

semiconducting quantum dots and nanorods are introduced on graphene sheets. CdS, PbS, and ZnO nanorods were widely studied for the enhanced absorption in the visible and UV region. Graphene can play different roles in photovoltaic applications including TCE, active materials in solar cells, and counter electrodes in dye-sensitized solar cells [121,122]. The nonlinear optical properties of graphene are mainly due to the linear electronic dispersion with zero bandgap, broad band absorption,vand ultrafast carrier dynamics. Graphene and its derivatives are effectively used as a saturable absorber in ultrafast lasers [123]. Sun *et al*. report that graphene incorporated with a polymer such as poly vinyl alcohol is a good alternative for pristine graphene as a saturable absorber [124].

On detailed review and comparison between graphene and graphene nanocomposites, it is observed that graphene nanocomposite has a better future in many of the applications. In the present work, we are focusing on the effect of graphene on inorganic metal oxide nanocomposite and its related applications. Here we have chosen perovskite nanomaterial as the dispersing phase on graphene for the detailed study.

1.8 Motivation of the Thesis

As discussed in section 1.3.3 some of the inherent properties restrict the applications of perovskites. In order to improve the properties of a perovskite, graphene can provide an amazing environment. As discussed in section 1.6 and 1.7 graphene metal oxide nanocomposite shows enhanced properties. Also the mechanism leading to the synergistic effect between graphene and metal oxide counterpart in nanocomposite form is not unveiled yet. In this context, **the motivation of the thesis is comprehended as "Utilize the amazing environment offered by graphene interface to tune the properties of a perovskite material and understand the mechanism of the interaction in detail"**. In order to study the detailed mechanism of

interaction of graphene with a metal oxide in nanocomposite, perovskite can be the best model. Since perovskite shows the chemical variation in the form of change in its properties. Based on the motivation we intended to (a) Study the exact mechanism of interfacing effect between graphene and $LaFeO_3$ perovskite (b) Study the interfacing effect on different properties of $LaFeO_3$ perovskite.

1.9 Objectives of the Thesis

The objectives of the thesis are based on the motivation **"Utilize the amazing environment offered by graphene interface to tune the properties of a perovskite material and understand the mechanism of the interaction in detail"**. According to the motivation, the thesis is categorized into four-fold objectives :

- Fabrication of graphene perovskite nanocomposite.
- Study the effect of varied concentration of graphene-perovskite interface by utilizing electrochemical conductance as a tool.
- Study the effect of interface with graphene on the optical properties of a perovskite.
- Study the impact of interface with graphene on the sensing and capacitive nature of a perovskite.

1.10 Overview of the Experimental Work

Experimental works have been carried out in accordance with the objectives of the thesis. Chapters 3, 4, 5 and 6 explain different experiments carried out and discuss conclusions drawn as part of the thesis while Chapter 7 concludes the works. Chapter 2 deals with the different characterizations used in the present work. Chapter 3 describes the synthesis mechanism adopted for the

fabrication of graphene perovskite interface. The prime focus of the fourth Chapter is the interaction of graphene with $LaFeO_3$ and its induced distortion effect in the crystal structure of the perovskite. Electrochemical conductance is used as a tool to find the effect of interface on the behaviour of perovskite nanocomposite. The distortion is inferred on the basis of XRD-Rietveld refinement and Raman spectroscopic data. The enhanced electrochemical conductivity of the material is understood in terms of the effect of non lattice oxygen on the perovskite structure. Chapter 5 describes the strain induced by graphene on perovskite crystal structure and its influence on optical as well as photocatalytic application. The variation in lifetime and dye degradation efficiency of the photoexcited carriers are discussed in terms of the effect of intermediate bands associated with the nanocomposite. Studies on the electrochemical sensing mechanism and the capacitive action of the composite also show the effect of graphene on perovskite which is described in Chapter 6. The H_2O_2 sensing mechanism of graphene perovskite composite shows that, the electrode materials have high selectivity towards analyte among other interfering materials. Chapter 7 comprises the conclusions and future perspectives of this study.

1.11 References

[1] K.S. Novoselov, Science. 306 (2004) 666–669.

[2] K.S. Novoselov, V.I. Fal′ko, L. Colombo, Nature. 490 (2012) 192–200.

[3] R.E. Schaak, T.E. Mallouk, Chemistry of Materials. 12 (2000) 3427–3434.

[4] Y. Tsunoda, W. Sugimoto, Y. Sugahara, Chemistry of Materials. 15 (2003) 632–635.

[5] S. Uma, A.R. Raju, J. Gopalakrishnan, J. Mater. Chem. 3 (1993) 709–713.

[6] Zhiguo Xia and Kenneth R. Poeppelmeier, Acc. Chem. Res. 50 (2017) 1222−1230. .

[7] S.G. Hur, T.W. Kim, S.J. Hwang, J.H. Choy, Journal of Photochemistry and Photobiology A: Chemistry. 183 (2006) 176–181.

[8] T. Arakawa, H. Kurachi, J. Shiokawa, Journal of Materials Science. 20 (1985) 1207–1210.

[9] D.B. Mitzi, Chemistry of Materials. 8 (1996) 791–800.

[10] Z. Deng, F. Wei, S. Sun, Journal of Materials Chemistry A. 4 (2016) 12025–12029.

[11] www.perovskite-info.com/perovskite-introduction .

[12] Z. Li, W. Zhang, C. Yuan, Y. Su, RSC Advances. 7 (2017) 12931–12937.

[13] K.A. Gschneidner, L. Eyring, M.B. Maple, eds., Handbook on the physics and chemistry of rare earths. Vol. 26:1. ed, North-Holland Publ, Amsterdam, 1999.

[14] A. Tiranov, A. Ortu, S. Welinski, Physical Review B. 98 (2018)195110-12 .

[15] G. Blasse, Progress in Solid State Chemistry. 18 (1988) 79–171.

[16] W.F. Zhang, J. Tang, J. Ye, Chemical Physics Letters. 418 (2006) 174–178.

[17] Y. Pan, Q. Su, H. Xu, Journal of Solid State Chemistry. 174 (2003) 69–73.

[18] T. Esaka, Solid State Ionics. 166 (2004) 351–357.

[19] J. Henao, Y. Pacheco, O. Sotelo, Journal of Materials Research and Technology 8 (2018) 759-765.

[20] A. Kaabi, M. Tliha, A. Dhahri, C. Khaldi, 2016 7th International Renewable Energy Congress (IREC) 2016, 1–5.

[21] Y. Yuan, Z. Dong, Y. Li, Progress in Natural Science: Materials International. 27 (2017) 88–92.
[22] S. Royer, D. Duprez, ChemCatChem. 3 (2011) 24–65.
[23] J. Hwang, R.R. Rao, L. Giordano, Y. Katayama, Y. Yu, Science. 358 (2017) 751–756.
[24] M.A. Peña, J.L.G. Fierro, Chemical Reviews. 101 (2001) 1981–2018.
[25] H. Zhang, G. Chen, Y. Li, International Journal of Hydrogen Energy. 35 (2010) 2713–2716.
[26] H. Kato, A. Kudo, The Journal of Physical Chemistry B. 106 (2002) 5029–5034.
[27] J. Shi, L. Guo, Progress in Natural Science: Materials International. 22 (2012) 592–615.
[28] S. Acharya, D.K. Padhi, K.M. Parida, Catalysis Today. (2017)(In Press).
[29] A. Kojima, K. Teshima, Y. Shirai, T. Miyasaka, Journal of the American Chemical Society. 131 (2009) 6050–6051.
[30] S.S. Mali, C.S. Shim, C.K. Hong, NPG Asia Materials. 7 (2015) e208–e208.
[31] J. Xing, X.F. Liu, Q. Zhang, Nano Letters. 15 (2015) 4571–4577.
[32] Ye Xiao, The Optical Characterisation of Graphene, Imperial College London, 2013.
[33] Scientific back ground on the nobel prize in physics 2010, Graphene. https://6702d.https.cdn.softlayer.net/assets/globalassets-priser-nobel-2010-sciback_fy_10.pdf
[34] A.K. Geim, P. Kim, Carbon Wonderland, Scientific American. 298 (2008) 90–97.
[35] A.K. Geim, K.S. Novoselov, The rise of graphene, Nature Materials. 6 (2007) 183–191.
[36] Y. Zhu, S. Murali, W. Cai, Advanced Materials. 22 (2010) 3906–3924.
[37] Juliet L Defino, The State University of New Jersey, 2012.
[38] K.P. Loh, Q. Bao, P.K. Ang, J. Yang, Journal of Materials Chemistry. 20 (2010) 2277-2289.
[39] https://kva.se/en/pressrum/pressmeddelanden/nobelpriset-i-fysik-2010.
[40] K. Kostarelos, K.S. Novoselov, Nature Nanotechnology. 9 (2014) 744–745.
[41] J.H. Ahn, B.H. Hong, Nature Nanotechnology. 9 (2014) 737–738.
[42] R. Ruoff, Nature Nanotechnology. 3 (2008) 10–11.

[43] J. Liu,Nature Nanotechnology. 9 (2014) 739–741.
[44] C.T.J. Low, F.C. Walsh, M.H. Chakrabarti, Carbon. 54 (2013) 1–21.
[45] K.I. Bolotin, K.J. Sikes, Z. Jiang, Solid State Communications. 146 (2008) 351–355.
[46] Y. Zhang, L. Zhang, C. Zhou, Accounts of Chemical Research. 46 (2013) 2329–2339.
[47] N. Mishra, J. Boeckl, N. Motta, Physica Status Solidi (a). 213 (2016) 2277–2289.
[48] Y.L. Zhong, Z. Tian, G.P. Simon, Materials Today. 18 (2015) 73–78.
[49] H.C. Lee, W.W. Liu, S.P. Chai, RSC Advances. 7 (2017) 15644–15693.
[50] S. Park, R.S. Ruoff, Nature Nanotechnology. 4 (2009) 217–224.
[51] C. Zhang, W. Lv, X. Xie, Carbon. 62 (2013) 11–24.
[52] C. Soldano, A. Mahmood, E. Dujardin, Carbon. 48 (2010) 2127–2150.
[53] X. Jia, J. Campos-Delgado, M. Terrones, Nanoscale. 3 (2011) 86–95.
[54] M.J. Allen, V.C. Tung, R.B. Kaner, Chemical Reviews. 110 (2010) 132–145.
[55] M. Inagaki, F. Kang, Journal of Materials Chemistry A. 2 (2014) 13193–13206.
[56] R.R. Amirov, J. Shayimova, Z. Nasirova, Carbon. 116 (2017) 356–365.
[57] H. He, T. Riedl, A. Lerf, J. Phys. Chem. 100 (1996) 19954–19958.
[58] D.R. Dreyer, S. Park, C.W. Bielawski, Chem. Soc. Rev. 39 (2010) 228–240.
[59] H.A. Becerril, J. Mao, Z. Liu, ACS Nano. 2 (2008) 463–470.
[60] J. Robertson, Materials Science and Engineering: R: Reports. 37 (2002) 129–281.
[61] S. Vempati, T. Uyar, Phys. Chem. Chem. Phys. 16 (2014) 21183–21203.
[62] Y. Gao, L.Q. Liu, S.Z. Zu, ACS Nano. 5 (2011) 2134–2141.
[63] F. Li, X. Jiang, J. Zhao, Nano Energy. 16 (2015) 488–515.
[64] E.T. Thostenson, Z. Ren, T.W. Chou, Composites Science and Technology. 61 (2001) 1899–1912.
[65] H. Qian, E.S. Greenhalgh, M.S.P. Shaffer,J. Mater. Chem. 20 (2010) 4751–4762.
[66] S. Bai, X. Shen, RSC Adv. 2 (2012) 64–98.
[67] K. Zhou, Y. Zhu, X. Yang, C. Li, New J. Chem. 34 (2010) 2950–2955.
[68] Y. Si, E.T. Samulski, Chem. Mater. 20 (2008) 6792–6797.
[69] S. Stankovich, D.A. Dikin, R.D. Piner, Carbon. 45 (2007) 1558–1565.
[70] Z. Jin, D. Nackashi, W. Lu, Chem. Mater. 22 (2010) 5695–5699.

[71] K.S. Novoselov, A.K. Geim, S.V. Morozov, Nature. 438 (2005) 197–200.
[72] V.C. Tung, L.M. Chen, M.J. Allen, Nano Lett. 9 (2009) 1949–1955.
[73] T.K. Hong, D.W. Lee, H.J. Choi, ACS Nano. 4 (2010) 3861–3868.
[74] A.A. Balandin, S. Ghosh, W. Bao, Nano Letters. 8 (2008) 902–907.
[75] K.J. Jeon, Z. Lee, Chemical Communications. 47 (2011) 3610-3612.
[76] G.M. Scheuermann, L. Rumi, P. Steurer, Journal of the American Chemical Society. 131 (2009) 8262–8270.
[77] Z. Tang, S. Shen, J. Zhuang, Angewandte Chemie International Edition. 49 (2010) 4603–4607.
[78] J. Li, X. Fu, Z. Mao, Nanoscale Research Letters. 11 (2016) 1-8.
[79] K. Fu, Y. Wang, L. Mao, Electrochimica Acta. 215 (2016) 427–434.
[80] E. Bayram, G. Yilmaz, S. Mukerjee, Applied Catalysis B: Environmental. 192 (2016) 26–34.
[81] L.T. Soo, K.S. Loh, A.B. Mohamad, Journal of Power Sources. 324 (2016) 412–420.
[82] X. Xu, Z. Zhang, L. Qiu, Nature Nanotechnology. 11 (2016) 930–935.
[83] L. Qu, Y. Liu, J.B. Baek, ACS Nano. 4 (2010) 1321–1326.
[84] A.M. El-Sawy, I.M. Mosa, D. Su, Advanced Energy Materials. 6 (2016).
[85] K. Kakaei, A. Balavandi, Journal of Colloid and Interface Science. 463 (2016) 46–54.
[86] Y.J. Fan, S.F. Wu, Journal of CO2 Utilization. 16 (2016) 150–156.
[87] Q. Li, W. Zhu, J. Fu, Nano Energy. 24 (2016) 1–9.
[88] M. Hu, Z. Yao, X. Wang, Industrial & Engineering Chemistry Research. 56 (2017) 3477–3502.
[89] A.R. Nanakkal, L.K. Alexander,Journal of Materials Science. 52 (2017) 7997–8006.
[90] Q. Li, B. Guo, J. Yu, Journal of the American Chemical Society. 133 (2011) 10878–10884.
[91] W. Zhou, J. Liu, T. Chen, Physical Chemistry Chemical Physics. 13 (2011) 14462-14465.
[92] J. Yan, T. Wei, W. Qiao, Electrochimica Acta. 55 (2010) 6973–6978.
[93] B. Wang, J. Park, C. Wang, Electrochimica Acta. 55 (2010) 6812–6817.
[94] Z. Gao, J. Wang, Z. Li, Chemistry of Materials. 23 (2011) 3509–3516.
[95] L. Wang, D. Wang, X.Y. Dong, Chemical Communications. 47 (2011) 3556-3558.

[96] H.W. Wang, Z.A. Hu, Y.Q. Chang, Journal of Materials Chemistry. 21 (2011) 10504-10511.
[97] J.W. Lee, T. Ahn, D. Soundararajan, Chemical Communications. 47 (2011) 6305-6307.
[98] B. Li, H. Cao, G. Yin, Journal of Materials Chemistry. 21 (2011) 10645-10648.
[99] Y. Wang, C.X. Guo, J. Liu, Dalton Transactions. 40 (2011) 6388-6391.
[100] Y.L. Chen, Z.A. Hu, Y.Q. Chang, The Journal of Physical Chemistry C. 115 (2011) 2563–2571.
[101] Y. Zhang, H. Li, L. Pan, Journal of Electroanalytical Chemistry. 634 (2009) 68–71.
[102] T. Lu, Y. Zhang, H. Li, Electrochimica Acta. 55 (2010) 4170–4173.
[103] S.M. Paek, E. Yoo, I. Honma, Nano Letters. 9 (2009) 72–75.
[104] Y.J. Mai, X.L. Wang, J.Y. Xiang, Electrochimica Acta. 56 (2011) 2306–2311.
[105] J. Choi, J. Jin, I.G. Jung, Chemical Communications. 47 (2011) 5241-5243.
[106] Y.S. He, D.W. Bai, X. Yang, Electrochemistry Communications. 12 (2010) 570–573.
[107] L. Shen, C. Yuan, H. Luo, Nanoscale. 3 (2011) 572–574.
[108] J. Zhu, Y.K. Sharma, Z. Zeng, The Journal of Physical Chemistry C. 115 (2011) 8400–8406.
[109] J. Zhu, T. Zhu, X. Zhou, Y. Zhang, Nanoscale. 3 (2011) 1084–1089.
[110] A. Kaniyoor, R. Imran Jafri, T. Arockiadoss, Nanoscale. 1 (2009) 382-386.
[111] H.Y. Jeong, D.S. Lee, H.K. Choi, Applied Physics Letters. 96 (2010) 213105-3.
[112] J.L. Johnson, A. Behnam, S.J. Pearton, Advanced Materials. 22 (2010) 4877–4880.
[113] H. Wang, F. Ren, R. Yue, Colloids and Surfaces A: Physicochemical and Engineering Aspects. 448 (2014) 181–185.
[114] R.A. Dar, N.G. Khare, D.P. Cole, RSC Adv. 4 (2014) 14432–14440.
[115] L. Yang, D. Liu, J. Huang, Sensors and Actuators B: Chemical. 193 (2014) 166–172.
[116] J. Liang, Z. Chen, L. Guo, Chemical Communications. 47 (2011) 5476-5478.
[117] Y. Wang, S. Zhang, D. Du, Journal of Materials Chemistry. 21 (2011) 5319-5325

[118] R.S. Dey, C.R. Raj, The Journal of Physical Chemistry C. 114 (2010) 21427–21433.
[119] S. Guo, D. Wen, Y. Zhai, ACS Nano. 4 (2010) 3959–3968.
[120] K. Zhou, Y. Zhu, X. Yang, Electrochimica Acta. 55 (2010) 3055–3060.
[121] X. Wang, L. Zhi, K. Müllen, Nano Letters. 8 (2008) 323–327.
[122] H. Chang, X. Lv, H. Zhang, Electrochemistry Communications. 12 (2010) 483–487.
[123] Q. Bao, H. Zhang, Y. Wang, Advanced Functional Materials. 19 (2009) 3077–3083.
[124] Z. Sun, T. Hasan, F. Torrisi, ACS Nano. 4 (2010) 803–810.

CHAPTER 2

EXPERIMETNAL TECHNIQUES

This chapter describes various experimental techniques used for the analysis of synthesized samples.

The structural features and properties of the interface between graphene and perovskite were extensively studied using different sophisticated analysing techniques. In the present work, mainly focused characterization techniques include X-ray diffraction, Rietveld refinement method and Raman spectroscopy for the structural determination. Morphological evaluation is done by Field emission scanning electron microscope (FESEM). X-ray photoelectron spectroscopy (XPS) is used for the elemental composition analysis. In optical studies, UV-Vis DRS spectroscopy, fluorescence with lifetime measurements were carried out. For the electrochemical investigations Cyclicvoltammetry (CV), Chronoamperometry, Differential Pulse Voltammetry (DPV) and Galvanostatic charge-discharge (GCD) were used.

2.1 X-Ray Diffraction Analysis

The diffraction of light occurs when it is scattered by a periodic array of long-range order producing a constructive interference at specific angles. The atoms in crystals are arranged in a periodic array and thus can diffract light. The X-ray diffraction on the crystalline surface is occurring due to the similar range in X-ray wavelength with that of atomic spacing in the crystal *i.e.*, of the order of 10^{-10} m. Two different phenomena are happening while x-rays interact with matter (i) Scattering from each individual atom (ii) Interference of the scattered beam. The geometrical condition that must be satisfied for the diffraction is formulated by Bragg. Geometrically, a crystal made up of families of lattice planes which will reflect the X-rays incident on the plane. When the reflected rays which are in phase, reach the detector will produce a strong diffraction peak. The schematic diagram of X-ray diffraction is shown Fig. 2.1.The relation between the incident X-ray wavelength (λ), the spacing between the planes (d) and the angle of incidence (θ) is

$$n\lambda = 2d\sin\theta \quad [1]$$

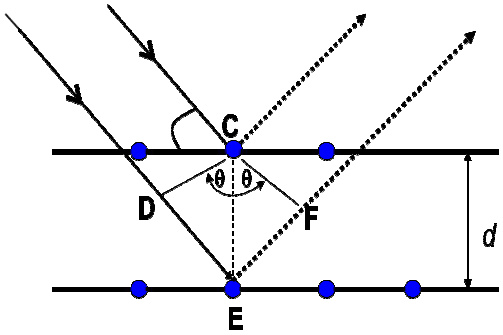

Fig. 2.1 Schematic diagram of X-ray diffraction from the lattice planes

The essential parts of the diffractometer shown in Fig. 2.2(a) includes (i) X-ray tube (ii) Incident beam and receiving side optics (iii) Goniometer (iv) Sample holder and (v) Detector. X-rays produced from the source pass through two different divergent slits. Among the two divergent slits one is located between the X-ray source and the specimen, and the second one is at the specimen and the detector. The divergent slits limit the scattered (non-diffracted) radiation, reduce background noise and it also collimate the radiation. Goniometer is a platform that holds and moves the sample, optics, detector and/or the tube. The detector counts the number of X-rays scattered by the sample [2,3]. The X-ray diffractometer used for the powder sample analysis using wavelength (λ= CuKα – 1.541Å) is shown in Fig. 2.2 (b).

Fig. 2.2 (a) Image of different components of X-ray diffractometer [image adapted from [4]] (b) Image of X-ray diffractometer used in the thesis.

Application of X-ray diffraction technique: The scattering of X-rays from atoms produces a diffraction pattern, which contains information about

- Atomic arrangement within the crystals
- Crystalline positions of different atoms
- The degree of order (crystallinity) and
- The nature of forces that hold them together.

2.1.1 Rietveld Refinement

Rietveld pattern fitting is a method used to refine the crystal structure. From X-ray and neutron powder diffraction data, Rietveld refinement extracts the crystal information. Technologically interesting materials are mostly available in the polycrystalline form rather than in single crystal. So it is important to find the structural parameters of the prepared powders. The Rietveld refinement method refines the user selected parameters to minimize the difference between observed data and the model chose. The common limitation of powder diffraction is (i) Systematic overlapping of diffraction peaks due to symmetry conditions (ii) Accidental overlapping because of limited experimental resolution (iii) Considerable background and (iv) Non-

random distribution of the crystallites in the specimen generally known as preferred orientation [5,6]. In order to overcome the above mentioned problems related to diffraction can be resolved by Rietveld refinement method.

The underlying idea in Rietveld refinement is that it considers the entire powder diffraction pattern using a mixture of refinable parameters. That way the problem encountered by peak overlap in diffraction pattern is resolved [7]. The Rietveld function optimize the model function by minimizing the weighed sum of squared differences between the observed and computed intensity value i.e.,

$$\Sigma_i w_i (y_{c,i} - y_{o,i})^2 \text{ where } w_i = \frac{1}{\sigma^2[y_{o,i}]}.$$

The symbol σ is defined as $\sigma_{y_o,i}^2 = \langle (y_{o,i} - \langle y_{o,i} \rangle^2 \rangle$ known as standard uncertainty. Here y_c is the computed value of intensity, whereas y_O is the observed intensity value.

The quality of refinement is characterized by R-factor. The most used discrepancy index is weighed profile R-factor (R_{wp}) - it is directly obtained from the square root of the quantity to be minimized. The expression for R_{wp} can be written as

$$R_{wp}^2 = \Sigma_i w_i (y_{c,i} - y_{o,i})^2 / \Sigma_i w_i \left(y_{O_i}\right)^2 [8].$$

The parameters that are adjusted throughout the least square refinement is (i) Lattice parameter (a, b, c, α, β, γ) (ii) Atomic positions (x, y, z) (iii) Atomic site occupancy (iv) Atomic thermal vibrational parameter (isotropic or anisotropic) (v) Parameters from Cagliotti formula (U,V,W) (vi) Preferred orientation (vii) Background function (viii) 2θ Zero correction (ix) Overall scale factor (x) Overall isotropic thermal B. The input value requires for the refinement are (i) Starting and ending of 2θ value, (ii) Step in which

2θ is measured, (iii) Wavelength and (iv) Initial values of all the parameter that can be adjusted [5].

2.2 Raman Spectroscopy

Raman spectroscopy is one of the important non-destructive characterizations of nanomaterial. It is based on the interaction of light with matter. Fig. 2.3 shows the different types of radiation associated with the interactions of light with matter. In a Raman experiment, if the sample is transparent, most of the light falling on the sample will transmit, remaining fraction of light undergoes two types of scattering namely Rayleigh (elastic scattering) and Raman scattering (inelastic scattering). The inelastic scattering of light by matter helps to probe the structure of gases, liquids, and amorphous as well as crystalline solids. The Raman spectrum is generally formed out of Stokes lines with relatively higher intensity than Anti-Stocks lines. Inelastically scattered light is collected and ploted as Raman spectrum. The spectrum consists the intensity of inelastically scattered light as a function of the wave number. Wave number shift δν is one of the critical parameters in the Raman spectrum. Raman shift is defined as the difference in wave number between observed radiations to that of the source used.

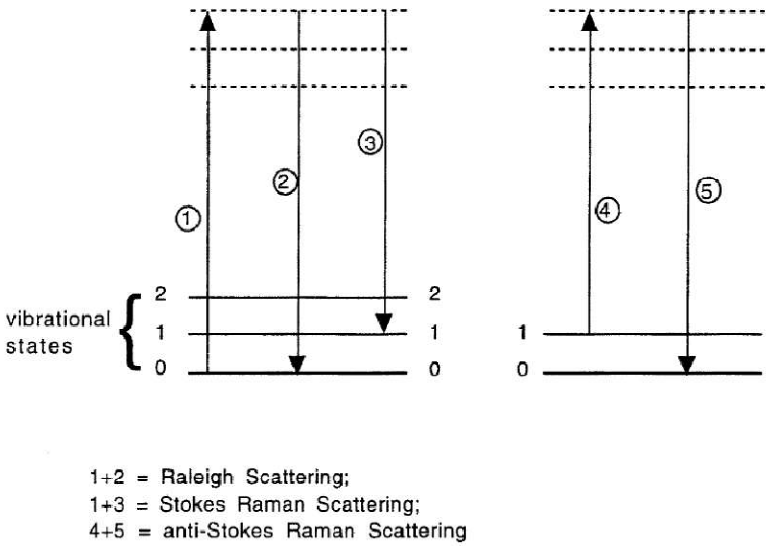

Fig. 2.3 A schematic representation of Raman lines [9]

Raman spectra consist of the vibrational modes of a solid. The total number of peaks in the spectrum is related to the number of symmetry allowed *i.e.*, Raman active modes. Raman activity is a function of the point group symmetry of a molecule and the space group symmetry of a crystalline solid. So it is considered to be the fingerprint of the scattering material. Raman can provide information including the strength of interatomic and intermolecular bonds, the mechanical strain present in a solid, the composition of multicomponent matter, the degree of crystallinity of a solid, and the effects of pressure and temperature on phase transformations [9].

The instrumentation for Raman scattering experiments is shown in Fig 2.4. Raman instrument consists of (i) A monochromatic light source (usually 532 green laser) for the excitation (ii) Optical equipment parts converge the laser beam on the sample and collect the scattered light (iii) Spectrometer is a wavelength selector which analyze the scattered light and (iv) A detector to collect the signal. If the exciting and analyzing light is manipulated with optical filters and polarizers, further complementary information on the sample can be derived [3,10].

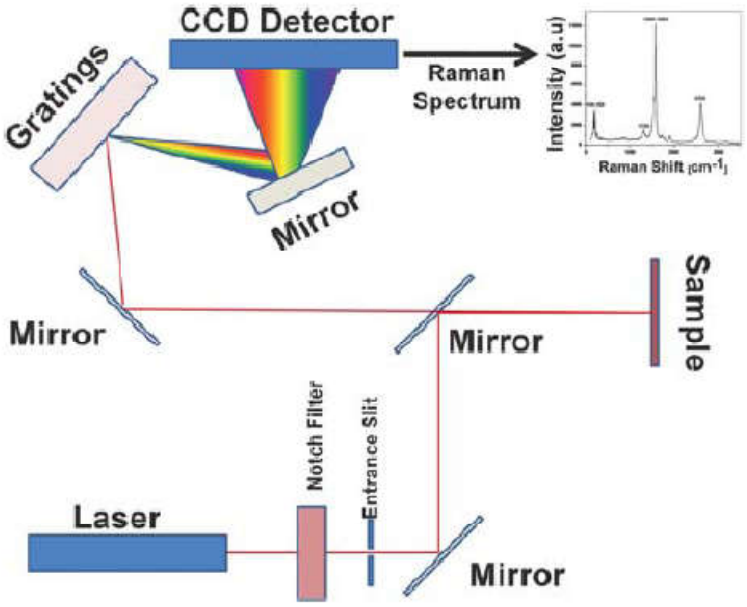

Fig. 2.4 Schematic representation of Raman spectrometer : image is taken from [11]

Raman spectra are widely used to probe carbon based materials. It is considered to be the finger print for graphene analysis [12]. In graphene, the Raman shift in D and G band gives the nature of synthesized graphene sheet. The relation between I_{2D} / I_G gives the number of layers in the synthesized sample [13]. Fig. 2.5 shows the Raman instrument used for the analysis. For our experiments we used micro Raman with 532 nm green laser (Jasco NRS 4100) situated at our laboratory and the equipment at CENSE IISC Bangalore (HORIBA, Lab RAM HR JOBNYVON).

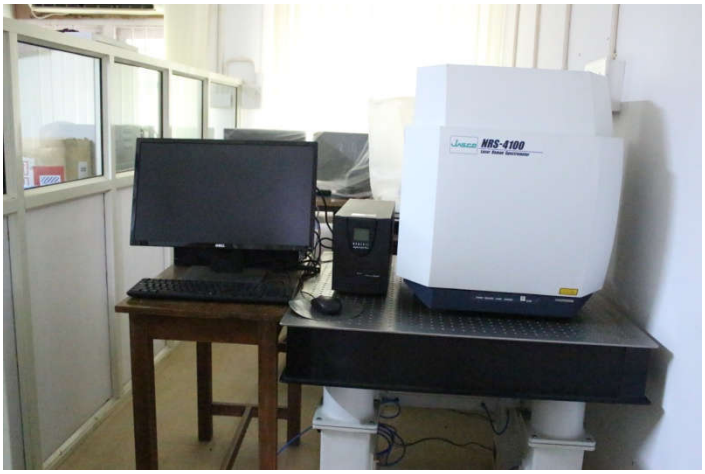

Fig. 2.5 Micro Raman instrument used for part of this thesis.

The strength of Raman analysis is

(i) It is a non-destructive technique

(ii) Easily identifies the chemical structure

(iii) Solid /liquides/ gas can be analyzed

(iv) Small amount of sample is needed for the analysis.

2.3 Optical Studies

2.3.1 UV-Vis-NIR Spectrophotometer - Diffuse Reflectance Spectra

A reflectance spectrum from the powdered samples is obtained by the analysis of surface reflected electromagnetic radiation as a function of frequency ν (usually in wave number (cm^{-1})) or wavelength (λ in nm). Two different types of reflection namely specular and diffuse can occur when light is irradiated on the surface. Specular reflection is associated with a mirror-like smooth and polished surface where as diffuse reflection is linked to surface texture like powders. If the dimension of the particle is large compared to the wavelength of irradiation, then the phenomenon like reflection, refraction, and diffraction occurs. If the orientation of crystal surfaces is in all directions, the reflected light from the surface also diverges. That is diffuse reflectance is defined by the condition that angular distribution of the reflected radiation is independent of the angle of incidence. Diffuse reflectance is commonly measured in UV-Vis-NIR and mid-IR region to obtain molecular spectroscopic information. The schematic diagram of diffuse reflectance from the crystal surface is shown in Fig. 2.6(a). Samples which undergoes diffuse reflectance during measurement absorbs and scatters radiation simultaneously. Kubelka-Munk theory is often used to describe and analyze the diffuse reflectance spectra of the powdered sample. Using Kubelka-Munck function one can calculate the optical band gap of the powder sample.

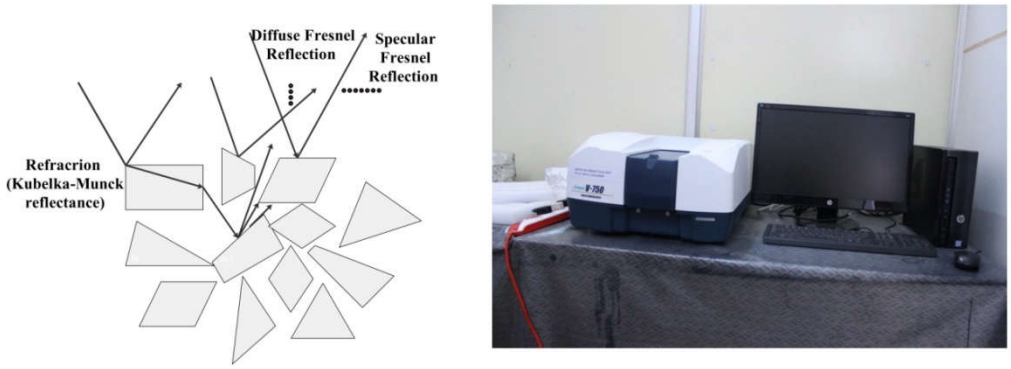

Fig. 2.6 (a) Schematic diagram of optical phenomenon involved in diffuse reflectance: image is taken from [14] (b) UV-Vis spectrophotometer used in this study.

Kubelka-Munk function linearly relates the analyte concentration with the diffuse reflectance of the sample.

$$F(R) = \frac{(1-R)^2}{2R} = \frac{K}{S} = 2.303\frac{\varepsilon C}{S}$$

Where K is the absorption coefficient, S is the scattering coefficient, R is the percentage of reflectance, ε is the absorptivity and C is the analyte concentration [14]. Factors affecting UV-Vis-NIR DRS spectra are (i) Particle size (ii) Refractive index (iii) Homogeneity of the sample and (iv) Packing [15].

The major component of UV-Vis-NIR diffuse reflectance spectrophotometer is (i) A light source (usually Xe light) (ii) An integrating sphere (hollow enclosure with walls coated with diffusely reflecting material, usually $BaSO_4$ or PTFE) (iii) Sample holder (centre mount cuvette style sample holder and clip and jaw type center mount sample holder) and (iv) Detector (generally photomultiplier tube) [16]. Fig. 2.6(b) shows the UV-Vis-NIR spectrophotometer used in the present study.

2.3.2 Fluorescence Studies

The phenomenon of luminescence is linked to the absorption of energy by the molecule in the form of photons. In the case of luminescence the transfer of electron to higher level due to the absorption of light by the molecule occur at fast pace, a typical time interval of the order of 10^{-15} sec. Luminescence is the emission of light associated with the de excitation of charge carriers from the excited states to the ground state. Depending on the nature of the excited state, luminescence can be formally divided into fluorescence and phosphorescence. In the case of fluorescence the electrons in the excited singlet state are oppositely paired with the second electrons in the ground-state orbitals. So the excitation is spin-allowed and emission occurs rapidly with a lifetime of the order of 10^{-9} sec. Phosphorescence is the emission associated with the triply excited state. In this state, the electron has the same spin orientation as that of the ground state and it forbid the transitions of electrons. So in the case of phosphorescence the emission rates are very slow of the order of 10^{-3} to 10^{-1} sec [17]. The process of fluorescence and phosphorescence is shown in the Jablonski diagram as given in Fig. 2.7, which usually discusses the light absorption and emissions in molecules.

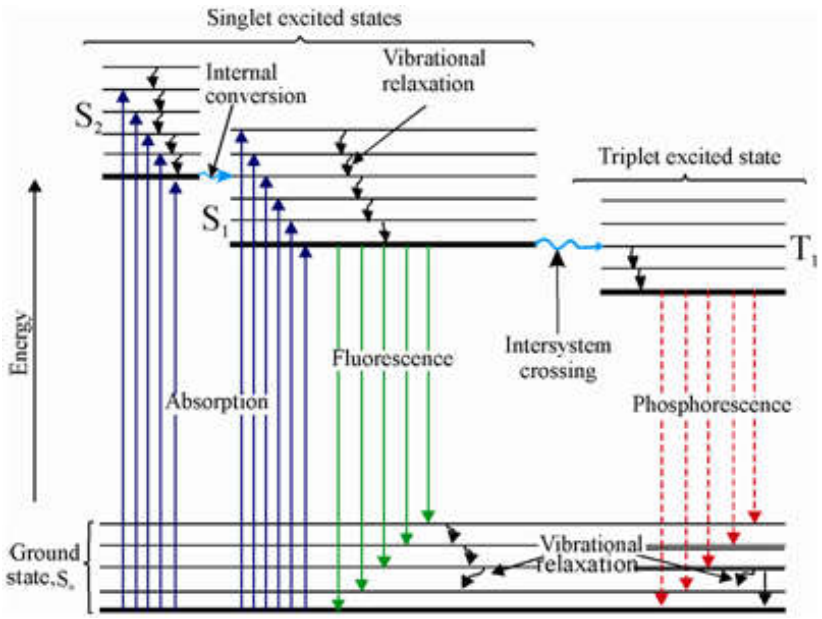

Fig. 2.7 Jablonski diagram showing fluorescence and phosphorescence [18]

Considering the Jablonski diagram fluorescence energy of emission is typically less than that of absorption. The major reason for the Stock shift in fluorescence is the rapid decay of photoexcited electrons to the higher vibrational level of S_0. The stock shift can also be due to the solvent effects, excited state reaction, complex formation, and energy transfer.

2.3.3 Fluorescence Lifetime Measurements

The fluorescence lifetime is one of the important characteristics of a fluorophore. Lifetime determines the time required for the fluorophore to interact or diffuse in its environment *i.e.*, the average time of the electron spends in the excited state prior to return to the ground state. The average lifetime can be calculated in two different ways.

(1) Intensity average - It is defined as the average lifetime of a collection of different excited state population. The lifetime of each population is weighed by the relative contribution of that population to the total fluorescence [19]. Average lifetime is calculated using the expression $\tau_{avg} = \frac{\sum a_i \tau_i^2}{\sum a_i \tau_i}$ where a_i is the amplitude fraction and τ_i is the lifetime.

(2) Amplitude average - It is defined as $\tau_{avg} = \frac{\sum a_i \tau_i}{\sum a_i}$. This is the lifetime of a fluorophore if it had the same steady-state fluorescence as that of others with several lifetimes. The weighed factor used in the calculation is the amplitude fraction [19]. In the present work we are using amplitude averaging for the lifetime measurements.

The main components of spectrofluorometer are (i) Light source (ii) Monochromators and (iii) Detector. High intensity Xenon lamp with radiation ranging from 235 nm is used as the exciting source. Monochromators are used to select both emission and excitation wavelength. The excitation

monochromator contains two gratings which are concave in nature to reduce the stray light. Fluorescence is detected with a photomultiplier tube and it is quantified with appropriate electronic devices.There is an optical module which surrounds the sample holder in the fluorometer. The main components of the optical module are shutters, beam splitter, and polarizers which are used to control the excited and emitted wavelength. The schematic diagram of spectrofluorometer is shown in Fig. 2.8.

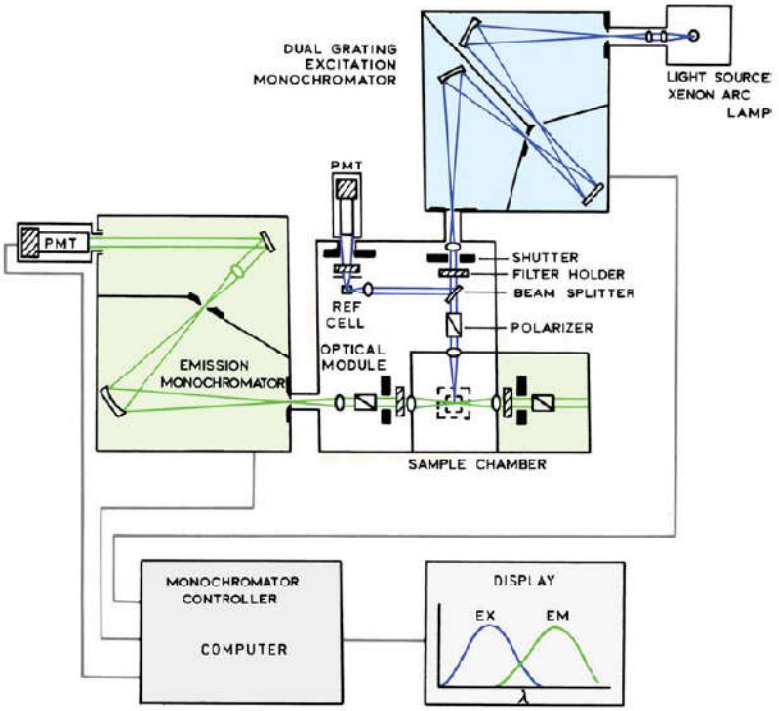

Fig. 2.8 Schematic image of spectrofluorometer: image is adapted from [17]

Advantages of fluorescence measurements are

- Sensitivity: The limit of detection of a fluorometer depends on the properties of the analyte used. Fluorescence achieves a high level of sensitivity with detectability of the order of parts per billion or even parts per trillion.

- Specificity: In general photometers, most of the materials absorb the incident light such that it is difficult to differentiate the analyte from

the interference materials. But fluorometers are more specific because fewer materials undergo fluorescence.

- Simplicity and speed: The fluorescence technique is relatively a simple technique. The sensitivity and specificity of this technique reduce the time for the sample preparation and the analysis of the spectra [20].

2.4 X-Ray Photoelectron Spectroscopy (XPS)

Solid materials can interact with the surroundings through their surfaces. The physical and chemical compositions of the surface determine the nature of the interactions. An atom can eject electrons on absorption of X-ray photon. The kinetic energy of the ejected eletron depends on its binding energy and the energy of incident photon. By analyzing the kinetic energy of the emitted electrons the following conclusion can be obtained

- Element near to the material surface
- The chemical state of the element
- The binding energy of the electron

Binding energy of the electron depends upon the chemical environment of the material, the nature of the element and the orbital from which the electrons are emitted.

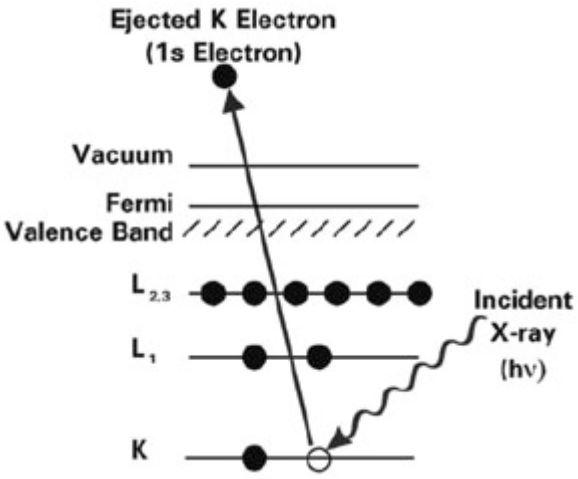

Fig. 2.9 Schematic images of electron ejection from core shells of an atom [21]

The analytical information derived from XPS is the kinetic energy of the emitted electrons from the surface of the sample while irradiating with monochromatic X-rays. XPS is a quantitative technique because the cross-section for the emission of a photoelectron is not dependent on the chemical environment of the atom. XPS can be probe the sample from the top ~ 1-10 nm and it is suitable for any type of materials ranging from metals to biological samples [22].

The XPS hardware consists of (a) Ultra-high vacuum chamber (b) X-ray Source (c) Flood gun (d) Transfer lenses (e) Analyzer and (f) Ion gun. Fig. 2.10 shows the XPS used in this study [23]. Vacuum chamber keeps the system contaminant free and allows a longer path for photoelectrons. The Aluminium electrode with photon energy 1486.6 eV is used as an X-ray source in XPS. Flood gun is necessary for analyzing nonconducting and polymer samples. For non conducting samples it acts as surfaces which counter acts on the build-up charges. In the case of analyzer, generally hemispherical energy analyzer is used in XPS. The main objective of transfer lenses is that it focuses and slows down the photoelectrons emitted by the

samples. For the depth profiling cleaning and milling of the surface are essential and for that ion guns are using.

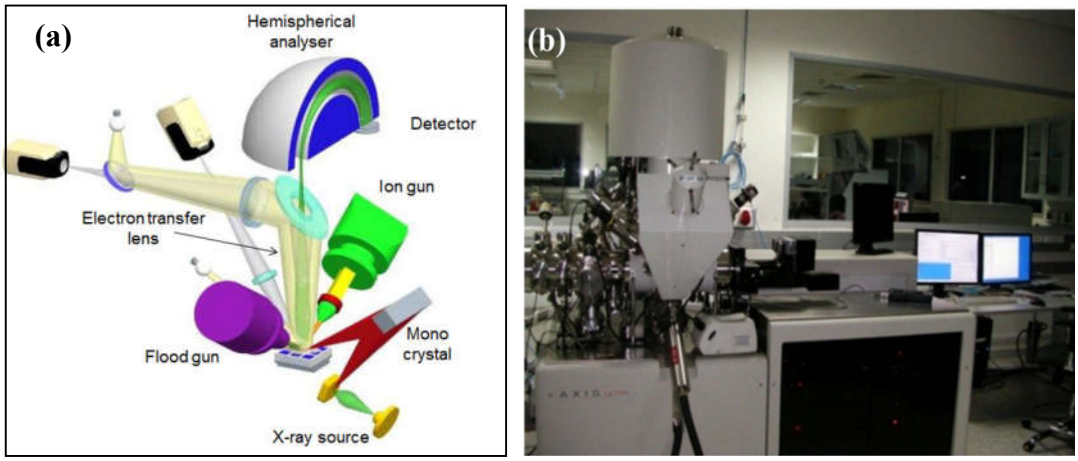

Fig. 2.10 (a) Schematic of XPS system [23] (b) XPS used in the present work [picture curtesy: CENSE IISc Banglore]

Advantages of XPS studies are:

- Non-destructive technique
- Surface-sensitive (10-100 Å)
- Quantitative measurements can be done
- Provide information about chemical bonding

2.5. Electron Microscope

In general, microscopes consists of several parts which includes a source for illumination, a condenser lens to converge the beam from the source to the sample, an objective lens to magnify the image and a projector lens to project the image onto an image plane. The wave nature of electron is used to obtain the image of the sample in an electron microscope. The lenses used in electron microscopes are electromagnetic in nature. Among electron microscopes two major forms are Scanning electron microscope (SEM) and

Transmission electron microscope (TEM). Here we used scanning electron microscopy is used for the analysis of dispersed phase of LFO on RGO.

2.5.1 Scanning Electron Microscopy (SEM)

SEM is used to form a high resolution surface image of the specimen using electrons instead of light. When a high energy electron beam interacts with the matter, it will generate backscattered electrons, X-rays, secondary electrons and Auger electrons. The ejected electrons are detected and these signals contain information about the sample under investigation [24]. The schematic diagram showing the working principle of SEM is given in Fig. 2.11.

The main parts of the scanning electron microscope are i) Electron gun ii) Electron lens iii) Scan coils and iv) Electron detectors. Electron sources produce a stable beam of electrons. Generally, there are two types of electron sources thermionic and field emission emitters. Tungsten or lanthanum hexa borates (LaB_6) are commonly used as thermionic emitters. In the case of field emission emitters, a tungsten tip is subjected to a very high potential to produce electron beams. FESEM images are used for the high resolution and contrast nanomaterial images. The condenser lenses focus the electron beams with an energy typically in the range 0.2 keV to 40 keV to a spot having the diameter of 0.4 to 5 nm . The position of the electron beam on the sample is controlled by scan coils situated above the objective lens. The objective aperture limits the angular spread "α" of the electrons. The focused beam is scanned in raster fashion over the sample surface in a rectangular manner. The interaction of electron beam and sample produce electrons which are detected using electron detectors.

The specimen can be viewed as a function of secondary electrons or back scattered electrons (BSE). The low energy secondary electrons are

formed by the irradiation of beam on the surface or from the subsurface down to 30 nm. Secondary electron detection gives the shape and topographical information about the sample. High energy back scattered electrons are emitted from a depth of 1 μm. Since it dependents on the nuclear reaction, BSE is very sensitive to the atomic number. The yield of BSE depends on the atomic number of the constituent atom. So the heavy atoms appear to be bright in such images. Thus this image is suitable for observing the compositional differences [24,25].

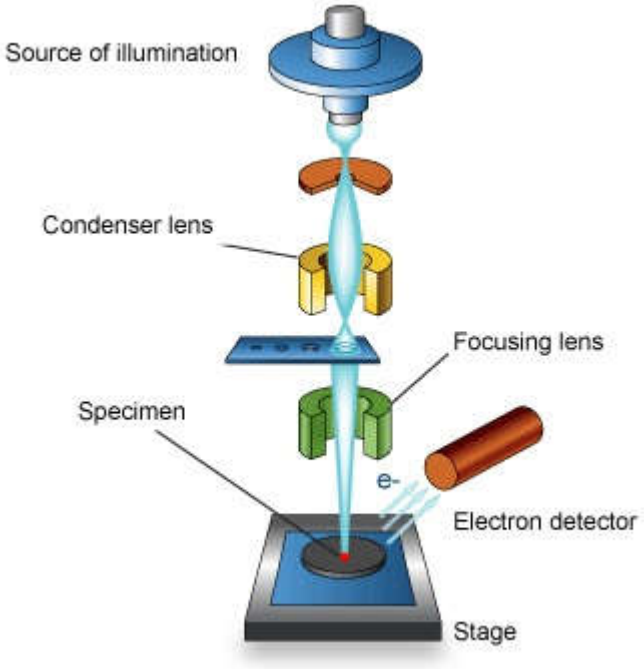

Fig. 2.11 The basic layout of a FESEM instrument [26].

2.6 Electrochemical Characterization

Electron transfer plays an elementary role in directing the pathways of chemical reactions. It is difficult to probe the number of electrons involved and the speed of electron transfer in traditional experimental methods like spectroscopy [27]. To explore the reactions involving electron transfer mechanism electrochemistry is considered to be a powerful tool [28]. It

relates to the flow of electrons to the chemical changes. Electrochemistry measures the relationship between electrical parameters such as current, potential, charge that of chemical variables [29]. It is commonly employed to investigate the oxidation and reduction processes of the species. Electrochemistry is widely using in the area of corrosion of metals, electrochemical and biological sensors, voltammetric reaction mechanism, catalytic studies, *etc.* [30]. There are several methods for electrochemical measurements. In this thesis voltage controlled method is used (*e.g.* Cyclic voltammetry, Differential pulse voltammetry and Chronoamperometry *etc*.). The electrochemical measurements are generally carried in three electrode systems.

Three electrode system

Schematic illustration of a typical three-electrode system is shown in Fig. 2.12. It consists of three electrodes named as Working electrode (WE), Reference electrode (RE) and Counter electrode (CE). The current flows between WE and CE where RE is used to measure the applied potential related to a stable reference reaction.

Working Electrode: A working electrode carries out the desired electrochemical reactions. The applied potential on the working electrode is controlled by the potentiostat in terms of the reference electrode. Since the electrochemical reactions are taking place on the surface of WE, the surface area should be clean and well defined. Here the graphite electrode modified with graphene nanocomposite is used as the working electrode.

Reference Electrode: This electrode is used as the reference point against which the potential of other electrodes are measured. Commercially available reference electrodes are standard hydrogen electrode, saturated calomel

electrode, standard hydrogen electrode, and Ag/AgCl electrode etc. In the present study Ag/AgCl is used as the reference electrode.

Counter Electrode: The counter electrode is used to complete the electrical circuit. When a potential is applied to the WE, oxidation or reduction of analyte will take place on the surface. CE by passes the produced current without passing through RE. In order to achieve this task CE will swing between higher potentials. To ensure the inhibition of the kinetics of reaction occurring at CE with WE, the surface area of the counter electrode is kept higher than that of the working electrode. Platinum wire is used as a counter electrode in the present case.

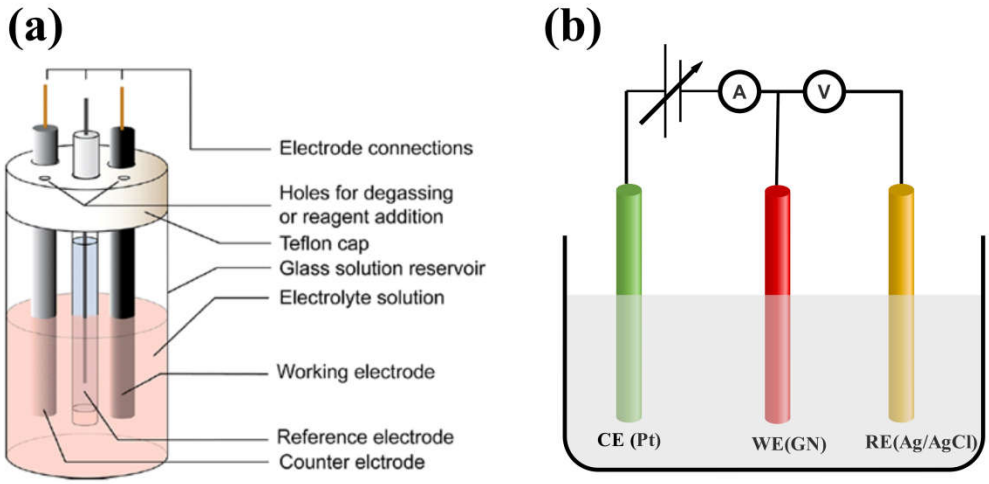

Fig. 2.12 (a) Schematic representation of the three electrode system [29] (b) Connection between three electrodes.

2.6.1 Cyclic Voltammetry

Cyclic Voltammetry (CV) is widely used to acquire the qualitative information about the electrochemical reactions. CV gives the information on redox process, heterogeneous electron-transfer reactions, and adsorption process. It provides a rapid location of the redox potential of the electroactive

species [31]. In order to obtain the cyclic voltammogram, a linear sweep potential is applied to the working electrode. Potential is sweeping in between two limits E1 and E2 on the WE. As the potential is swept, the current flowing through the electrode either oxidize or reduce the analyte. This current is proportional to the concentration of the analyte. So CV is used for the analytical determination of the concentration of the species.

2.6.2 Differential Pulse Voltammetry (DPV)

Differential pulse voltammetry was proposed by Barker and Gardner [32]. DPV gives greater sensitivity, higher resolution, and differentiation of various species. For analytical determination DPV is useful. The differential measurements can distinguish a Faradic current from a capacitive one. From initial to final potential, the applied waveform in DPV is a combination of pulse and a staircase. The current is measured before applying the pulse and at the end of the pulse. The difference in current at these two points is plotted against the potential. The current peak intensity is related to the concentration of the active species under investigation [31].

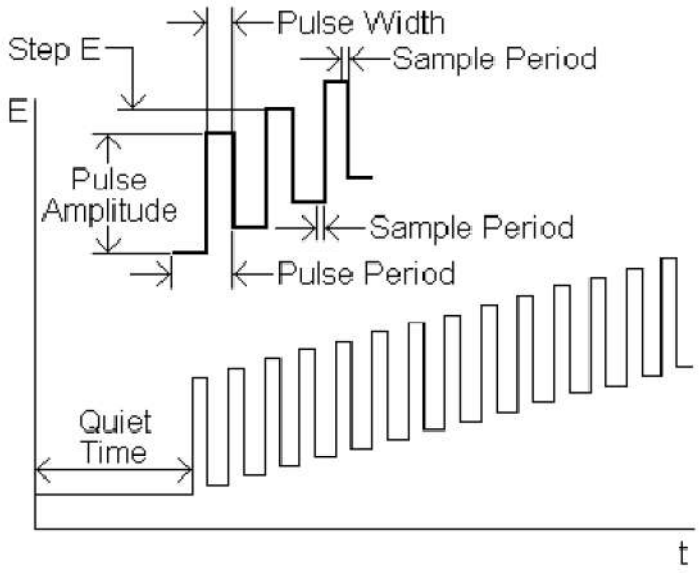

Fig. 2.13 Potential waveform of differential pulse voltammetry [33]

2.6.3 Chronoamperometry

Chronoamperometry is an electrochemical analysis in which the potential of the WE is stepped from initial potential (E_i) to final potential (E_f). The resulting current at the WE is causing from the potential step which is monitored as a function of time. Chronoamperometry is done on a three electrode system and a typical chronoamperogram potential waveform is shown in Fig. 2.14 [33].

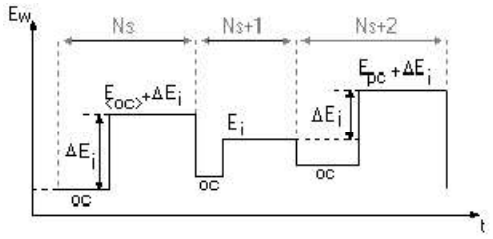

Fig. 2.14 Potential waveform of Chronoamperometry [31]

In this chapter I have elaborated about the fundamentals, mechanism and applications of the equipments used in this thesis work. Now in the corresponding Chapter 3-6, the make and the experimental conditions of the used equipments will be mentioned.

2.7 References

[1] C. Kittel, Introduction to solid state physics, 7th ed, Wiley, New York, 1996.
[2] Cullity, B.D, Elements of X-Ray Diffraction, Addison-Wesley, 1960.
[3] Kulkarni, Sulabha, Nanotechnology: Principles and Practices, 3rd ed., Springer International Publishing ,2015.
[4] http://www.xrpd.eu/.
[5] Prof. Dr. Georg Will, Powder Diffraction: The Rietveld Method and the Two Stage Method to Determine and Refine Crystal Structures from Powder Diffraction Data, Springer, 2006.
[6] Haowei Zhang, a study of the crystal structure of y3cd9zn2 using x-ray powder diffraction, The Pennsylvania State University, 2015.
[7] L.B. McCusker, R.B.V. Dreele, D.E. Cox, Rietveld refinement guidelines, J. Appl. Cryst. 32, (1999),36-50.
[8] B.H. Toby, Powder Diffraction. 21 ,(2006), 67–70.
[9] E.N. Kaufmann, ed., Characterization of materials, John Wiley and Sons, Hoboken, NJ, 2003.
[10] J.R. Ferraro, K. Nakamoto, C.W. Brown, Introductory Raman spectroscopy, 2nd ed, Academic Press, Amsterdam ; Boston, 2003.
[11] A. Biswas, T. Wang, A.S. Biris, Single metal nanoparticle spectroscopy: optical characterization of individual nanosystems for biomedical applications, Nanoscale. 2, (2010), 1560-1572.
[12] A.C. Ferrari, Solid State Communications. 143 ,(2007), 47–57.
[13] H.J. Kim, S.M. Lee, Y.S. Oh, Scientific Reports. 4 ,(2014), 5176-10.
[14] F.M. Mirabella, ed., Modern techniques in applied molecular spectroscopy, Wiley, New York, 1998.
[15] PIKE Technologies, Diffuse Reflectance – Theory and Applications,
[16] Walter Stanley Stiles, Gunter Wyszecki, Color Science: Concepts and Methods, Quantitative Data and Formulae, 2nd Edition, Wiley, 1969.
[17] J.R. Lakowicz, Principles of fluorescence spectroscopy, 3rd ed, Springer, New York, 2006.
[18] https://www.quora.com/What-is-the-Jablonski-diagram.
[19] A. Sillen, Y. Engelborghs, Photochemistry and Photobiology. 67 ,(1998), 475–486.
[20] http://www.turnerdesigns.com/general-fluorometer-faq/article/726-advantages-of-fluorescence-measurement.
[21] https://xpssimplified.com/whatisxps-photoemission.php.
[22] XPS Surface Analysis | Anderson Materials Evaluation, Inc. http://www.andersonmaterials.com/xps.html.
[23] https://www.axt.com.au/xps-surface-characterisation
[24] T. PRADEEP, Textbook of nanoscience and nanotechnology, McGraw Hill Education (India) Private Limited, 2012.
[25] M.F. Ashby, P.J. Ferreira, D. Schodek, Nanomaterials, nanotechnologies and design: an introduction for engineers and architects, Elsevier/Butterworth Heinemann, Amsterdam, 2009.
[26] https://myscope.training/legacy/images/sem/layout-and-function.png.

[27] Sharath Shankar, S, Development of neurotransmitter sensor using chemically modified carbon paste electrode by voltammetric investigations, Kuvempu University, 2012.
[28] A.J. Bard, L.R. Faulkner, Electrochemical methods: fundamentals and applications, 2nd ed, Wiley, New York, 2001.
[29] N. Elgrishi, K.J. Rountree, B.D. McCarthy, Journal of Chemical Education. 95 (2018), 197–206.
[30] Yan Zhou, Molecular Electrochemistry, University of Hull, 2012.
[31] BioLogic, EC-Lab Software: Techniques and Applications,
[32] D.B. Hibbert, Introduction to electrochemistry, Macmillan, Basingstoke, 1993.
[33] Radhakrishnan, S, Application of conducting polymers for DNA sensors, Alagappa University, 2013.

CHAPTER 3

Fabrication of Graphene perovskite interface

This chapter discusses the materials and methods for the fabrication of graphene perovskite interface. The exact chemical methods adopted for the synthesis of graphene perovskite nanocomposite are discussed in detail. A short discussion about the primary characterisations of doped LFO graphene nanocomposite is also given in this chapter.

In order to study the mechanism of interaction between graphene and metal oxide, graphene perovskite nanocomposites were fabricated. The dispersing phase on the graphene surface is taken as $LaFeO_3$ and its derivatives. Here partial substitution at *B* site is carried out with two different elements Al and Cr. The syntheses as well as preliminary characterisation of doped perovskite graphene nanocomposite are also given.

3.1 Preparation of perovskite nanomaterials

Solid state chemistry offers a variety of pathways for the synthesis of nanoparticles. The synthesis route plays an important role in deciding surface morphology, grain size, surface area, chemical and physical properties of the synthesised material [1,2].

Solid state reaction or shake and bake method is usually used for the synthesis of ceramic materials. In which, the reaction mechanism involves a higher temperature to trigger the slow solid-solid diffusion [3–5]. Here the particles posses' low kinetics and high temperature such that it forms a less homogeneous large grain size particles with a low surface area. The reaction mechanism restricts the applications of solid state synthesised nanoparticles in the field where high surface area is desirable (*e.g.* gas sensors, catalysis). Modification in this method by mechanochemical processing before calcination at high temperature yields single phase perovskite which is used in electroceramic applications [6]. Other preparative methods for perovskite materials are wet chemical method which includes (a) co-precipitation method (b) combustion method (c) impregnation method (d) spray pyrolysis (e) sol-gel/pechini method and (f) hydrothermal method [7–12]. In principle, all these synthesis routes can be used to obtain substituted perovskite materials but suffer some drawbacks. Complexity in the procedure, expensive precursors or high energy cost for thermal treatment prevents most of the synthesis route to prepare substituted perovskite materials [13]. Among the

wet synthesis route, combustion method is considered as one of the promising methods for the preparation of perovskite material. This method consists of a highly exothermic self combustion reaction between a fuel and the oxidant such that it produces enough heat to obtain ceramic powders. Also, it provides much faster reaction time and lowers calcination temperature leading to the formation of homogenous powder in nanometer scale [14]. In the current work, we have adopted citric acid mediated combustion method for the synthesis of perovskite $LaFeO_3$ and $LaFe_{0.8}R_{0.2}O_3$ (R = Al, Cr) nanomaterials.

3.1.1 Synthesis of perovskite $LaFeO_3$ (LFO)

LFO was synthesised by citric acid mediated solution method in which metal nitrate $La(NO_3)_3.6H_2O$ (99%-Alfa Aesar) and $Fe(NO_3)_3.9H_2O$(98%-Alfa Aesar) was mixed with citric acid in the molar ratio of 1:1:2. In the typical experiment, stochiometric amount of metal precursors were dissolved in 25 ml distilled water under constant stirring condition. Into this solution, the citric acid dissolved in 25 ml distilled water was added dropwise. The reaction mixture was stirred magnetically for 2 hours keeping the temperature at 50^0 C. The resultant orange color solution was kept in hot air oven at 80^0 C overnight and this was subjected to calcination at 800^0 C for 2 hours. The obtained powder ground well and used for further analysis. Thus the synthesis mechanism involved in the formation of LFO can be summarized as follows

$$La(NO_3)_3 \cdot 6H_2O + Fe(NO_3)_3.9H_2O + C_6H_8O_7 \longrightarrow LaFeO_3 + 6\,CO_2 + 3N_2 + nH_2O.$$

Crystalline nature and the phase purity of the sample were confirmed by XRD and Raman spectroscopy analysis. The detailed analysis of the samples are explained in Chapter 4.

3.1.2 Synthesis of perovskite $LaFe_{0.8}R_{0.2}O_3$ (LFR, R = Al, Cr)

Wet chemical citric acid mediated combustion method is employed for the preparation of $LaFe_{0.8}R_{0.2}O_3$ with R = Al and Cr samples. The similar synthesis conditions of LFO are applied to the formation of doped compounds.

In the case of $LaFe_{0.8}Al_{0.2}O_3$ (LFAL) synthesis, along with the metal precursors of LFO, stochiometric amount of $Al(NO_3).9H_2O$ (98%-Alfa Aesar) is added to the mixture and follows the reaction conditions of LFO.

To form $LaFe_{0.8}Cr_{0.2}O_3$ (LFCR), stotichiometric amount of $Cr(NO_3)_3.9H_2O$ (99.9%-Alfa Aesar) is added along with LFO precursors and follows the reaction condition as that of lanthanum orthoferrite. The obtained powder of LFAL and LFCR were ground well and used for further analysis.

3.2 Synthesis methods of Graphene oxide

Graphene can be synthesised by different methods as discussed in the introduction section 1.4. The yield of pristine graphene in the method like mechanical exfoliation and other technique is in picogram quantities. Chemical oxidation of graphite followed by exfoliation and reduction produces large quantities of graphene known as chemically modified graphene (CMG/Reduced graphene oxide (RGO)). During the last decade, study on RGO composites has been an emerging topic of research. The active functional groups render RGO to be a suitable candidate for many applications [15–17]. The synthesis mechanism of graphite oxide was proposed by Hummer and Offeman which is a modified form of Straudenmaire reaction method [18,19].The important steps involved in the preparation of graphite oxide using Hummer's method are

1. Oxidation of graphite with H_2SO_4, $NaNO_3$, and $KMnO_4$
2. Exclusion of excess $KMnO_4$ by adding H_2O_2 (it forms water soluble $MnSO_4$)
3. Washing with methanol/ ethanol

There are several other methods for the synthesis of graphite oxide, which includes (i) Brodie method: Pioneer work in oxidation of graphite uses fuming HNO_3 with $KClO_3$ (ii) Electrochemical oxidation method: Here, the oxidation is carried out by H_2SO_4 or HNO_3 with ammonia solution [20–22] (iii) Improved chemical synthesis technique : A mixture of H_2SO_4 - H_3PO_4 is used for the high yield of graphite oxide. The advantages of this technique include control on the reaction temperature and production of nontoxic gases as by-products [23].

Depending on the starting material and synthesis conditions, spectrum of oxygen functional groups can attach to the basal plane of graphene. Some of the proposed chemical formulae for GO by varying the ratios of oxygen functional groups such as carboxylic, carbonyl, epoxy andhydroxyl *etc*. are $C_8O_{3.5–4.3}H_{2.5–2.9}$, $C_8O_{3.78–5.05}H_{2.9–\ 4.4}$, $C_8O_{2.54}H_{3.91,}$ and $C_8O_{4.61}H_{6.70}$ [24–26]. The fluctuation in oxygen functional groups can be viewed as a change in color from gray to golden in Brodie method [26].

3.2.1 Synthesis of Graphene oxide (GO)

In the present work, GO was synthesised by modified Hummer's method. The typical experimental procedure pursued is as follows: 2 gm of graphite flake (325 mesh, 99.8%, Alfa Aesar) was mixed with 1 gm of sodium nitrate ($NaNO_3$) (98%, Alfa Aesar). The mixture was transferred to a 500 ml beaker containing con. Sulfuric acid (H_2SO_4, 96 ml) kept in an ice bath. The mixture was stirred well for 30 minutes. Then 8 gm of potassium permanganate ($KMnO_4$) (Merck) was added slowly to the solution under vigorous stirring conditions by maintaining the reaction temperature below 20^0C. The mixture was kept under constant stirring for about 18 hours at temperature < 30^0C (using cold water supply). Then the mixture was kept aside for a period of time to complete the reaction. Then the solution made up to 250 ml by adding sufficient amount of water into it. To remove the excess of $KMnO_4$, 5 ml of 30 % of H_2O_2 was added to the solution, which gave a brilliant yellow colour

to the mixture. The solution was kept at constant stirring for 2 hours to complete the reaction and a washing process was carried out. The washing process of yellow solution involves centrifugation with (1) 10% aqueous HCl solution (2) ethanol and finally (3) with water. After washing, the resultant liquid suspension became brown in colour. The obtained colloid was dried below 60^0C to make a free-standing layer of graphite oxide. In order to obtain graphene oxide, the synthesised graphite oxide was ultrasonicated in distilled water. Using XRD (2θ peak at around 10^0) and Raman spectra (D and G band) the formation of graphene oxide can be confirmed.

3.2.2 Reduction of graphene oxide

Reduction of GO is the process which restore the structure and properties of graphene. The compound which was obtained after the reduction of GO is termed as Reduced Graphene Oxide (RGO). Different strategies employed for the reduction results in varied properties as well as applications of RGO. During the reduction process, the oxygen derivatives are removed from the surface of GO and the graphene conjugated structure is restored. The advantages of RGO include the abundantly available cost effective precursor (graphite) for its synthesis and the property of hydrophilicity, which makes a stable solution and helps to use in large-scale applications [27].

There are different strategies for the synthesis of RGO in which some of them are

1) Thermal reduction:

During the rapid heating process oxygen functional groups on GO decomposes into gases and produce a huge pressure in between the stacked layers. This will reduce and exfoliate the sheets [28–31].

2) Microwave-photo reduction:

In this method reduction can be done by commercially available microwave. Here substance can be heated uniformly and rapidly so that RGO is produced within a few minutes in an ambient condition [28,32]. In flash reduction method, a single close-up flash from the Xenon arc lamp on freestanding GO could reduce the sheet effectively. At a close distance of <2 mm the photoenergy emitted by the flash lamp is 9 times higher than the thermal energy needed to heat GO over 100^0C. So the effective deoxygenation could be done by the flash irradiation method [33,34].

3) Chemical reduction:

Different strong reducing agents like hydrazine hydrate, metal hydrides (sodium hydride, $NaBH_4$ and $LiAlH_4$ *etc*) can be used to reduce GO. Reports show that using Ascorbic acid (Vitamin C), Hydrogen Iodide (HI), Hydroquinone, Urea, thio urea, and hot strong alkaline solutions can also be used for the reduction reactions [35–42]. Green reduction route like rose water treatment is also reported in the literature [43]. In the aforementioned methods, reduction using hydrazine hydrate, HI and $NaBH_4$ is reported to be the best candidate for the reduction of GO for device applications.

4) Electrochemical reduction:

In this method, efficient reduction of GO is accomplished by the electrochemical removal of oxygen functionalities. GO sheet is placed in a voltammetric cell containing a buffer solution at an ambient temperature. When the voltage is swept in a potential range, GO is reduced by the electron exchange between GO and the electrode. As a merit, there is no need of harmful chemical reducing agent for this process [44–46].

5) Hydrothermal/Solvothermal reduction:

This process is carried out in a sealed container in order to raise the temperature of solvent above the boiling point. The overheated supercritical

water (SC) acts as a reducing agent and provides a green chemistry alternative to the organic solvents [47,48]. SC water has strong electrolytic solvent power as that of the polar organic molecules with a high concentration of ions, diffusion coefficient, and dielectric constant. The behaviour of SC water triggers bond cleavage reactions. In hydrothermal processes, the reduction process of GO is similar to H^+ catalyzed dehydration of an alcohol. Here water provides H^+ ions for the protonation of OH. The dehydration can occur at intramolecular as well as intermolecular level on the edges and basal plane of GO. In intramolecular dehydration, edge site H and OH terminate and consequently recover the π bonding. By the principle of microreversibility, all the oxygen groups cannot be removed from GO. The residual negative charge on the RGO causes the dispersibility in water [49]. Fig. 3.1(A) shows the dehydration mechanism in intramolecular and intermolecular GO sheets.The mechanism of reduction at different temperatures is also shown in Fig. 3.1(B).

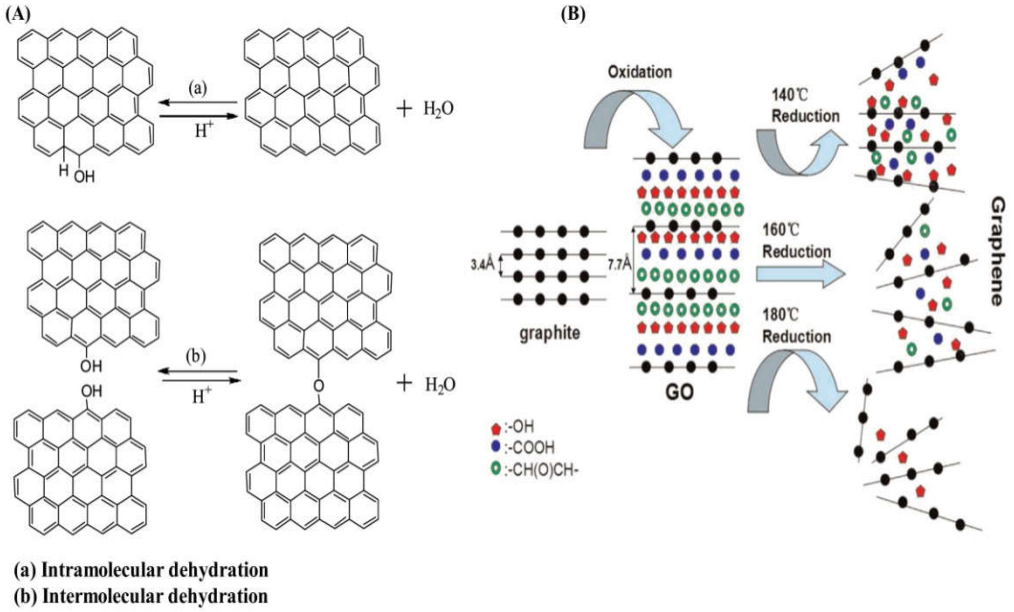

Fig. 3.1(A) Schematic representation of dehydration mechanism [49] (B) Hydrothermal mechanism of reduction of GO at different tempearature [50].

pH has a very important role in the reduction of GO. In the acidic media due to the protonation of O^- and COO^- the zeta potential of GO becomes very small [38,50]. When the zeta potential reduces, the strength of electrostatic repulsion between the sheets could not overcome the aggregation of GO. In the agglomerated state, GO tends to undergo intermolecular dehydration catalysed by H^+. Then the sheets could couple through an ether linkage. In alkaline media, presence of negatively charged O^- and COO^- increases the Zeta potential. The increased electrostatic repulsion prevents the aggregation between GO sheets and thus reduction is mediated through intramolecular dehydration [49].

Moderate reductions through hydrothermal process possess a highly dispersible RGO, which is required for graphene applications. In the *exsitu* synthesis of graphene metal oxide nanocomposite, metal oxide nanoparticles are rafted to the surface of GO during the reduction process. Subsequent hydrolysis functionalise the nanoparticles with RGO. Fig. 3.2 shows the typical hydrothermal autoclave used for the synthesis.

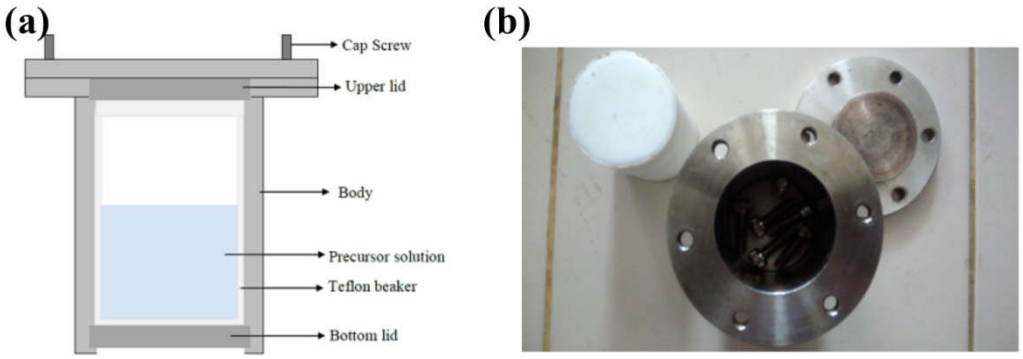

Fig. 3.2 (a) Schematic representation of autoclave (b) Autoclave used in the present study

6) Multistep reduction process:

In order to optimise the reduction process for special applications, multi-step reduction has been proposed. Eda *et al.* report that pretreatment with hydrazine will reduce the annealing temperature to produced good GO films [51]. Similarly, Gao *et al.* proposed three-step reduction processes with steps (a) deoxygenation with sodium borohydride (b) dehydration with con.H_2SO_4 and (c) thermal annealing at 1100^0 C. Through this process, the estimated oxygen content is less than 0.5 wt% and the C/O ratio of RGO is 246, which is the highest value reported [52].

Considering all the above reaction mechanisms, in the present study, we have adopted hydrothermal-a green channel reduction and functionalisation of GO-method for the combined reduction and functionalisation of graphene oxide.

3.3 Functionalisation of Graphene with a metal oxide.

Number of strategies has been proposed for the fabrication of graphene metal oxide nanocomposites. The procedures have been broadly classified into two, (i) *Insitu* functionalisation and (ii) *Exsitu* functionalisation.

3.3.1 *Insitu* functionalisation: This approach involves the formation of nanocrystallites directly on the surface of pristine or functionalised graphene. *Insitu* functionalisation comprises of a variety of synthesis procedures and supports surfactant free production of nanoparticles. Some of the insitu synthesis routes are solution deposition, direct decomposition of precursors, hydrothermal/solvothermal technique, gas phase deposition, sol-gel and template method [53].

3.3.2 *Exsitu* functionalisation: In this method, metal oxides were synthesised in advance and attached to the surface of graphene *via* covalent or non-covalent interactions. The distribution of metal nanoparticles on the surface of graphene is depending on the type of functionalisation and strength of

interaction between graphene and inorganic nanomaterials. The main advantage of this method can be considered as it overcomes the incompatibilities between nanomaterial synthesis and formation of the nanocomposite. A better distribution of particles, size, and presence of the second phase can be controlled in this method [53,54].

In this work, a one-pot hydrothermal route is adopted for the combined reduction and effective functionalisation of graphene with LFO nanoparticles. A detailed description of hydrothermal method for the reduction of graphene oxide is given in section 3.2.2.

3.4 Fabrication of Graphene-Perovskite interface

3.4.1 Synthesis of Graphene- $LaFeO_3$ nanocomposite (GLFO)

GLFO nanocomposite has been prepared by *exsitu* synthesis under hydrothermal condition. Varying the concentration of GO, three interfaces have been synthesised. The typical procedure for the preparation of GLFO nanocomposite can be explained as follows: In 75 ml of water, GO is dispersed using ultrasonicator and into this 0.1 gm of LFO is added. The mass ratio between GO to LFO is varied as 1:10, 5:10 and 10:10 and named as GLFO-1, GLFO-5, and GLFO-10 respectively. The 75 ml mixture is poured into a Teflon beaker of 100 ml capacity and heated in a hydrothermal furnace at 180^0 C for 6 hours. The resultant solution was centrifuged and washed. The solution was further dried at 60^0C and the obtained powder was used for analysis.

3.4.2 Fabrication of graphene-$LaFe_{0.8}R_{0.2}O_3$ interfaces (GLFR).

GLFR nanocomposite has been prepared by *exsitu* synthesis under hydrothermal condition. The procedure used for the synthesis of GLFO is followed for the fabrication of GLFR composites. In a typical procedure instead of adding LFO, Al or Cr doped LFRO is added to the varying the concentration of GO. The weight ratio between GO to LFR is varied as 1:10,

5:10 and 10:10 and named as GLFR-1, GLFR-5, and GLFR-10 where R= Al or Cr. The resultant grey colour solution was centrifuged, washed and dried at 60^0C. The powders are used for further analysis.

3.5 Characterisation of GLFR composite

Three different series of samples were synthesised for the analysis (GLFO, GLFAL and GLFCR). The Chapter 4 will be detailing the characterization and studies on LFO and GLFO samples. The analysis done for the understanding of effective functionalisation between LFCR/LFAL with graphene is discussed in the following sections.

3.5.1 Graphene- $LaFe_{0.8}Al_{0.2}O_3$ (GLFAL)

X-ray diffraction patterns were taken for the analysis of crystalline nature and phase purity of the prepared samples. Fig. 3.3 shows the XRD patterns of LFAL and GLFAL composites. The samples were found to be of pure phase. All the peaks in XRD pattern of LFAL is indexed with orthorhombic *pbnm* crystal structure [JCPDS (01-078-4429)].

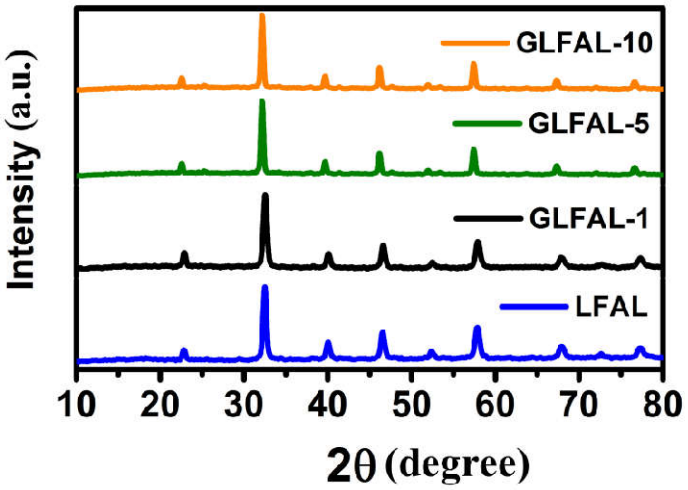

Fig. 3.3 XRD pattern of (a) LFAL (b) GLFAL-1 (c) GLFAL-5 and (d) GLFAL-10

The dispersed phase of LFAL on RGO is evaluated by FESEM analysis. The Fig. 3.4 shows that an effective dispersion of LFAL over RGO is happened through one pot hydrothermal method.

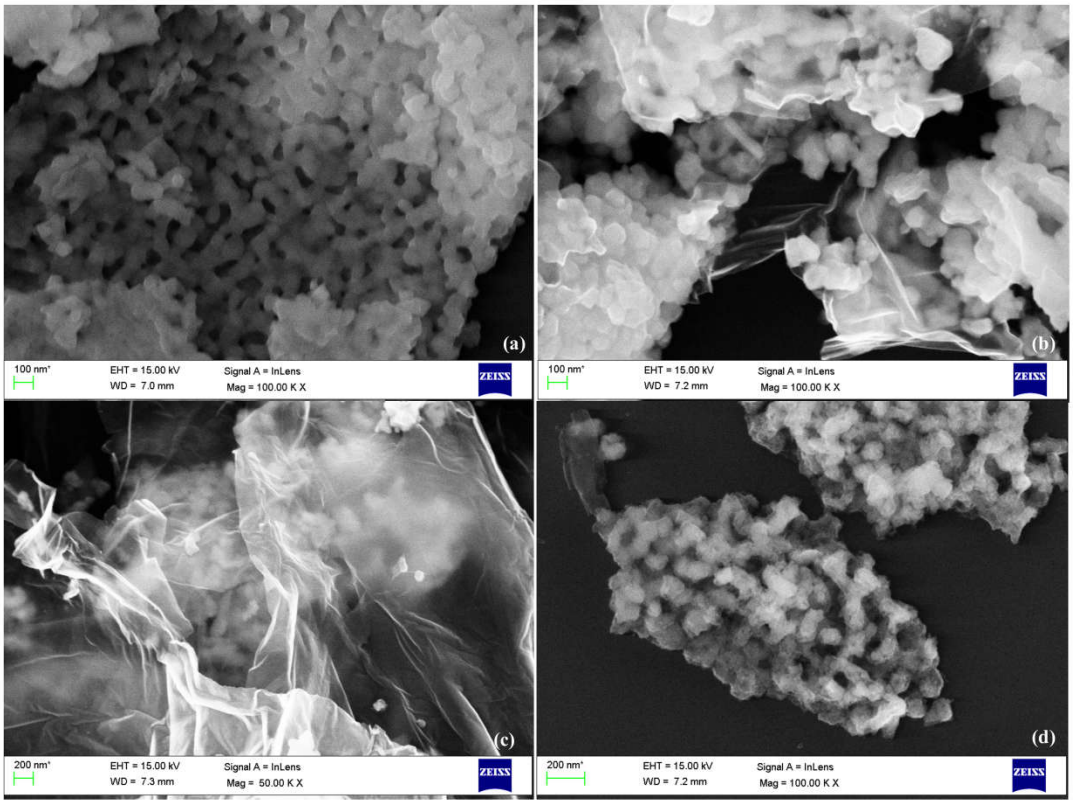

Fig. 3.4 FESEM images of (a) LFAL (b) GLFAL-1 (c) GLFAL-5 and (d) GLFAL-10

In order to further investigate on the structure of GLFAL, Raman spectroscopic analysis has been carried out and it is shown in Fig. 3.5.

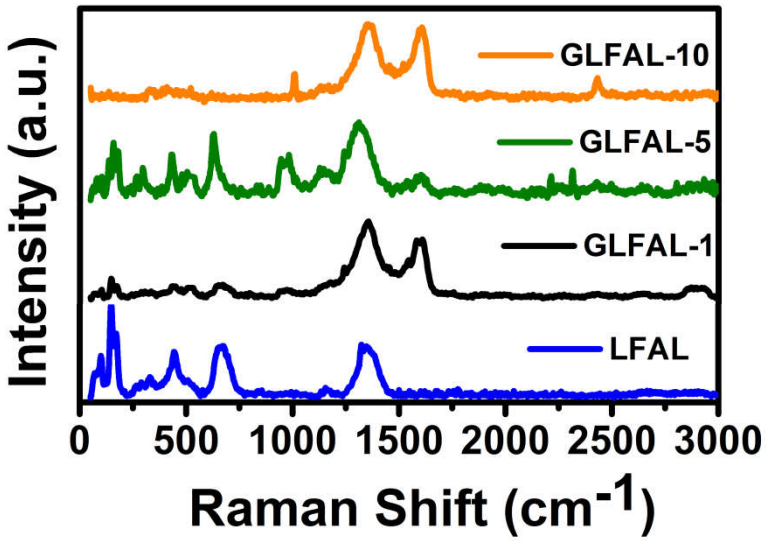

Fig. 3.5 Raman spectra of LFAL, GLFAL-1, GLFAL-5 and GLFAL-10. (The inconsistency in data demands further analysis)

The structural characterisation of GLFAL along with FESEM analysis shows that an effective functionalisation between graphene and LFAL has been established through the one-pot hydrothermal method. But the Raman spectroscopic data shows some inconsistency and it need further analysis.

3.5.2 Characterisation of GLFCR

The XRD patterns of GLCR as shown in Fig. 3.6 indicate a high crystalline nature and purity of the synthesised samples. The samples were found to be of pure phase. The crystal structure of LFCR and GLFCR is indexed with orthorhombic *pbnm* crystal structure with JCPDS (01-078-4429).

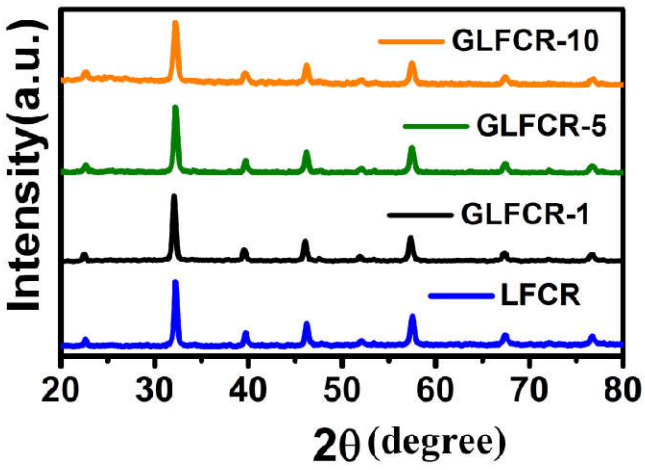

Fig. 3.6 XRD pattern of LFCR, GLFCR-1, GLFCR-5 and GLFCR-10

Fig. 3.7 shows the morphological evaluation of LFCR on graphene matrix.

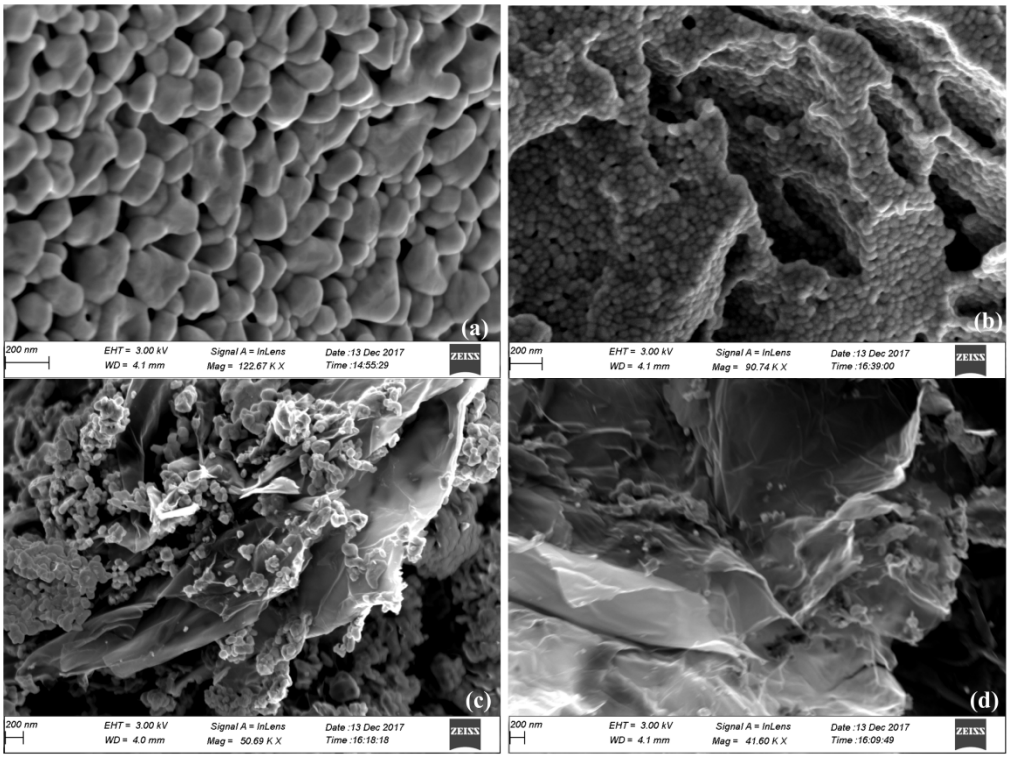

Fig. 3.7 FESEM images of (a) LFCR (b) GLFCR-1 (c) GLFCR-5 and (d) GLFCR-10

For the studies of effective linkage between graphene and LFCR, the sample is further characterised with Raman spectroscopic analysis. Fig. 3.8 shows that an additional peak at 683 cm^{-1} is prominent in LFCR compared to LFAL.

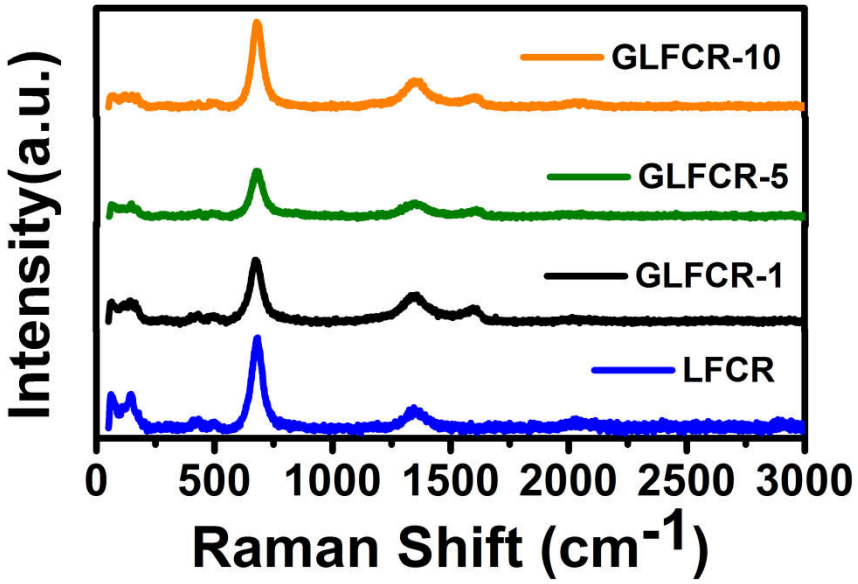

Fig. 3.8 Raman spectra of LFCR, GLFCR-1, GLFCR-5 and GLFCR-10.

The doping at *B* site has a significant role in the characteristics of perovskite nanomaterials. The structural analysis evidently shows that the effect of interface offered by graphene on the hetroatoms in *B* site of the perovskite is different. So a detailed analysis is needed for the fundamental understanding of the combined effect of doping the perovskite and the interfacing effect offered by graphene on LFO composite. As a stepping stone to the aforementioned analysis, this thesis discusses about the interfacing effect of Graphene-$LaFeO_3$ nanocomposite.

3.6 Summary

Varied concentrations of the interface between Graphene and LFO were successfully synthesised using chemical method**.** The synthesis could be briefed as, GO was prepared by the modified Hummer's method and LFO by citric acid mediated solution method. The detailed description of the synthesis conditions is given in section 3.1.1 and 3.2.1. The Graphene–Lanthanum iron oxide (GLFO) nanocomposite was synthesised by one-pot hydrothermal process. The elaborated synthesis technique for the functionalisation of graphene to LFO is given in section 3.4.1. The prepared GO was dispersed in water subsequently LFO was mixed with the GO solution in different weight ratios. The gram equivalent ratios of GO to LFO was 1:10, 5:10, and 10:10 and were named as GLFO-1, GLFO-5, and GLFO-10 respectively. The solution mixture was subjected to hydrothermal treatment at 180^0 C for 6 hours. The hydrothermal process lead to combined reduction and functionalisation of graphene oxide (GO). The black precipitate obtained was separated by centrifugation and dried at 60^0 C. The synthesised samples were characterised using XRD, Raman spectroscopy, FESEM, XPS, and Electrochemical analysis. The preliminary structural characterisation of GLFR composites shows the presence of phase pure sample. The variation in Raman peaks associated with the Al and Cr doped Lanthanum orthoferrite indicate the change in vibrational modes of *B*-O bonds in the crystal structure. The inconsistency in data demands further analysis on Raman spectra of the GLFR composites.

3.7 References

[1] A.K. Cheetham, P. Day, eds., Solid state chemistry: techniques, Clarendon Press; Oxford University Press, New York, 1987.

[2] C.N.R. Rao, J. Gopalakrishnan, New directions in solid state chemistry, 2nd ed, Cambridge University Press, New York, 1997.

[3] H. Fukuoka, T. Isami, S. Yamanaka, Chemistry Letters. 26 (1997) 703–704.

[4] A. Safari, R.K. Panda, V.F. Janas, Key Engineering Materials. 122–124 (1996) 35–70.

[5] Y. Inaguma, C. Liquan, M. Itoh, Solid State Communications. 86 (1993) 689–693.

[6] M. Senna, Journal of the European Ceramic Society. 25 (2005) 1977–1984.

[7] K.C. Patil, S.T. Aruna, T. Mimani, Current Opinion in Solid State and Materials Science. 6 (2002) 507–512.

[8] X. Qi, J. Zhou, Z. Yue, Z. Gui, L. Li, Ceramics International. 29 (2003) 347–349.

[9] S. Royer, F. Bérubé, S. Kaliaguine, Applied Catalysis A: General. 282 (2005) 273–284.

[10] D. Segal, Chemical synthesis of advanced ceramic materials, Cambridge University Press, Cambridge [England]; New York, 1989.

[11] J. Sfeir, S. Vaucher, P. Holtappels, Journal of the European Ceramic Society. 25 (2005) 1991–1995.

[12] J. Zhu, H. Li, L. Zhong, ACS Catalysis. 4 (2014) 2917–2940.

[13] C. Cristiani, G. Dotelli, M. Mariani, Chemical. Papers. 67 (2013) 526–531.

[14] A. Ecija, K. Vidal, A. Larrañaga, Advances in Crystallization Processes. (2012).

[15] Z. Sun, D.K. James, J.M. Tour, The Journal of Physical Chemistry Letters. 2 (2011) 2425–2432.

[16] D.R. Dreyer, S. Park, C.W. Bielawski, Chemical Society Reviews. 39 (2010) 228–240.

[17] S. Park, R.S. Ruoff, Nature Nanotechnology. 4 (2009) 217–224.

[18] W.S. Hummers, R.E. Offeman, Journal of the American Chemical Society. 80 (1958) 1339–1339.

[19] L. Staudenmaier, Berichte der deutschen chemischen Gesellschaft. 31 (1898) 1481–1487.

[20] M. Toyoda, A. Shimizu, H. Iwata, Carbon. 39 (2001) 1697–1707.

[22] W.G. Weng, G.H. Chen, D.J. Wu, Synthetic Metals. 139 (2003) 221–225.

[22] F. Kang, Y. Leng, T.Y. Zhang, Carbon. 35 (1997) 1089–1096.

[23] D.C. Marcano, D.V. Kosynkin, J.M. Berlin, ACS Nano. 4 (2010) 4806–4814.

[24] W. Scholz, H.P. Boehm, Zeitschrift for anorganische und allgemeine Chemie. 369 (1969) 327–340.

[25] T. Nakajima, Y. Matsuo, Carbon. 32 (1994) 469–475.

[26] T. Szabó, O. Berkesi, P. Forgó, Chemistry of Materials. 18 (2006) 2740–2749.

[27] S. Pei, H.M. Cheng, Carbon. 50 (2012) 3210–3228.

[28] Z.S. Wu, W. Ren, L. Gao, Carbon. 47 (2009) 493–499.

[30] M.J. McAllister, J.L. Li, D.H. Adamson, Chemistry of Materials. 19 (2007) 4396–4404.

[31] Z.S. Wu, W. Ren, L. Gao, ACS Nano. 3 (2009) 411–417.

[31] H.C. Schniepp, J.L. Li, M.J. McAllister, The Journal of Physical Chemistry B. 110 (2006) 8535–8539.

[32] H.M.A. Hassan, V. Abdelsayed, A.E.R.S. Khder, Journal of Material Chemistry. 19 (2009) 3832–3837.

[34] Y. Zhang, L. Guo, S. Wei, Nano Today. 5 (2010) 15–20.

[34] L.J. Cote, R. Cruz-Silva, J. Huang, Journal of the American Chemical Society. 131 (2009) 11027–11032.

[36] D. Yang, A. Velamakanni, G. Bozoklu, Carbon. 47 (2009) 145–152.

[37] M. Periasamy, M. Thirumalaikumar, Journal of Organometallic Chemistry. 609 (2000) 137–151.

[38] S. Pei, J. Zhao, J. Du, Carbon. 48 (2010) 4466–4474.

[38] X. Fan, W. Peng, Y. Li, Advanced Materials. 20 (2008) 4490–4493.

[39] G. Wang, J. Yang, J. Park, The Journal of Physical Chemistry C. 112 (2008) 8192–8195.

[40] X. Zhou, J. Zhang, H. Wu, The Journal of Physical Chemistry C. 115 (2011) 11957–11961.

[41] M.J. Fernández-Merino, L. Guardia, J.I. Paredes, The Journal of Physical Chemistry C. 114 (2010) 6426–6432.

[42] I.K. Moon, J. Lee, R.S. Ruoff, Nature Communications. 1 (2010) 1–6.

[43] B. Haghighi, M.A. Tabrizi, RSC Advances. 3 (2013) 13365.

[44] M. Zhou, Y. Wang, Y. Zhai, Chemistry – A European Journal. 15 (2009) 6116–6120.

[46] S.J. An, Y. Zhu, S.H. Lee,The Journal of Physical Chemistry Letters. 1 (2010) 1259–1263.

[46] Z. Wang, X. Zhou, J. Zhang, Journal of Physical Chemistry C. 113 (2009) 14071–14075.

[47] H. Wang, J.T. Robinson, X. Li, Journal of the American Chemical Society.131 (2009) 9910–9911.

[48] G. Demazeau, Journal of Material Chemistry. 9 (1999) 15–18.

[49] Y. Zhou, Q. Bao, L.A.L. Tang, Chemistry of Materials. 21 (2009) 2950–2956.

[50] D. Li, M.B. Müller, S. Gilje, Nature Nanotechnology. 3 (2008) 101–105.

[51] G. Eda, G. Fanchini, M. Chhowalla, Nature Nanotechnology. 3 (2008) 270–274.

[52] W. Gao, L.B. Alemany, L. Ci, P.M. Ajayan, Nature Chemistry.1 (2009) 403–408.

[53] S. Bai, X. Shen, RSC Advances. 2 (2012) 64–98.

[54] F.A. He, J.T. Fan, F. Song, Nanoscale. 3 (2011) 1182-1188

CHAPTER 4

Interaction Mechanism of Graphene-Lanthanum Orthoferrite Interface

The structural variations in perovskite crystals regulated by external forces could result in novel properties. Regulation in the structure of perovskite, driven by a non-invasive platform, especially like reduced graphene oxide (RGO) hold lot of significance in technological applications. Here, the control of structural distortion in a perovskite, $LaFeO_3$, impelled solely by interface with RGO and demonstration of the effect using a critical parameter - electrochemical conductivity is reported.

4.1 Introduction

Perovskites, an adaptable crystalline framework are extremely attractive regarding the fundamental and technological aspects. The variety of properties in electric, magnetic and structural fields is based on the ability of the perovskites to accommodate a wide range of elements, oxidation states, and stoichiometries irrespective of the size of the cations. Properties can be modified by varying the concentration of constituent phases of the nanocomposite, which in turn gives an insight into the correlation between structure and the functional properties. The strong electron-lattice correlation in the perovskite metal oxides implies that structural distortion can lead to variation in physicochemical properties [1–3]. The distortion in the BO_6 octahedra, embedded within the crystal lattice, tuned by changing size (bond length (B-O)), shape (no. of unequal bonds) and connectivity, can affect different properties of the perovskite compounds [4]. The chemical substitution within the lattice and the exertion of pressure during formation of the crystals are reported as leading strategies for changing the size and shape of the octahedra [5–9]. Epitaxial strain effect is reported to be one of the mechanisms to alter the connectivity between the octahedral frameworks [10,11]. The variation in three-dimensionally connected BO_6 octahedra by the aforementioned methods, in turn, leads to distortion in the global crystal structure of the material. Still, one of the attractive and challenging areas in engineering the functionality of a perovskite is to finely regulate the structural distortion without changing the constituents of the perovskite.

Graphene formed out of oxidation-exfoliation-reduction of graphite, create reaction sites like hydroxyl, carboxyl, carbonyl and epoxy groups, enabling a platform for engineering wide range of functionalities. Because of the

attractive features such as catalytic behavior, sensing activity, thermoelectric properties and photovoltaic enhancement, nowadays serious attempts are made to engineer the electrical characteristics of graphene-perovskite hybrid materials [12–16]. But a clear understanding about fundamental parameters driving the intriguing changes in characteristic properties of the dispersed phase in graphene-perovskite nanocomposite is to be developed.

Here, by utilising the surface properties, functionalisation of Reduced Graphene Oxide (RGO) with one of the significant member from orthoferrite perovskite family $LaFeO_3$ (LFO) has been carried out. This work attempts to study and develop a basic understanding of the impact of density of graphene interface on LFO using a critical parameter - electrochemical conductivity. The investigation led to unravel the link between the changes in chemical sensitivity parameters with interface dependent structural distortion induced on perovskite. The structural variation is established using Rietveld refinement and Raman spectroscopy. The distortion affects the oxygen concentration within the lattice, which is quantified using X-ray Photoelectron Spectroscopy (XPS). A fundamental understanding of the origin of the distortion accomplished in LFO is discussed.

4.2 Experimental Details

4.2.1 Sample Preparation

The detailed description about the adopted synthesis mechanism is explained in Chapter 3 (section 3.1.1, 3.2.1 and 3.4.1). As detailed in section 3.4.1 the nomenclature of the different samples are GLFO-1, GLFO-5 and GLFO-10 where the mass ratio between GO to LFO is varied as 1:10, 5:10 and 10:10 respectively.

4.2.2 Characterization

X-ray diffraction (XRD, CuKα Rigaku-600) and Raman spectroscopy (HORIBA-532 nm laser) were used for the structural investigation. The morphological examination was done using field emission scanning electron microscopy (FESEM) (GEMINI-ZEISS). The electrochemical workstation (BIOLOGIC SP-150) was used for the study of electrochemical conductivity. For all electrochemical measurements, a three electrode configuration was used with Pt as the counter electrode and saturated calomel electrode as reference. The details of the set up are given in section 2.6.The graphite working electrode was drop casted with 5 μL (concentration: 2 mg/ml) of graphene nanocomposite and dried at 80^0C. The current variation driven by nanocomposite coating was investigated with ammonium (AM) ions using differential pulse voltammetry (DPV) studies. Using X-ray photoelectron spectroscopy (XPS- Kratos Analytical HR Axis ultra analyzer), the concentration of element with different oxidation state were quantified in order to study the oxygen distribution in the nanocomposite.

4.3 Result

4.3.1 X-ray Diffraction Analysis

The XRD pattern of crystalline LFO and GO is shown in Fig. 4.1 (a). The characteristic peak of GO centered at 10.2^0 is indexed as (0 0 1) plane. Crystalline LFO was completely indexed in agreement to the orthorhombic *Pbnm* structure having highest intensity for (121) plane [JCPDS (01-078-4429)] [17]. Fig. 4.1 (b) also shows the XRD patterns of graphene-LFO nanocomposites (GLFO). In GLFO-10, the presence of an additional phase of Fe_2O_3 is identified. In order to understand the RGO concentration dependent dynamics of the crystalline structure, Rietveld refinements were carried out

on LFO and GLFO compounds. The fits are shown in Fig. 4.2. Refinement on entire GLFO composite has been done based on *Pbnm* space group which has a lower symmetry than cubic *Pm3m*. The unit cell parameters obtained by refinement are shown in Table 4.1. The table suggests a significant dependence of the lattice parameter on the RGO concentration.

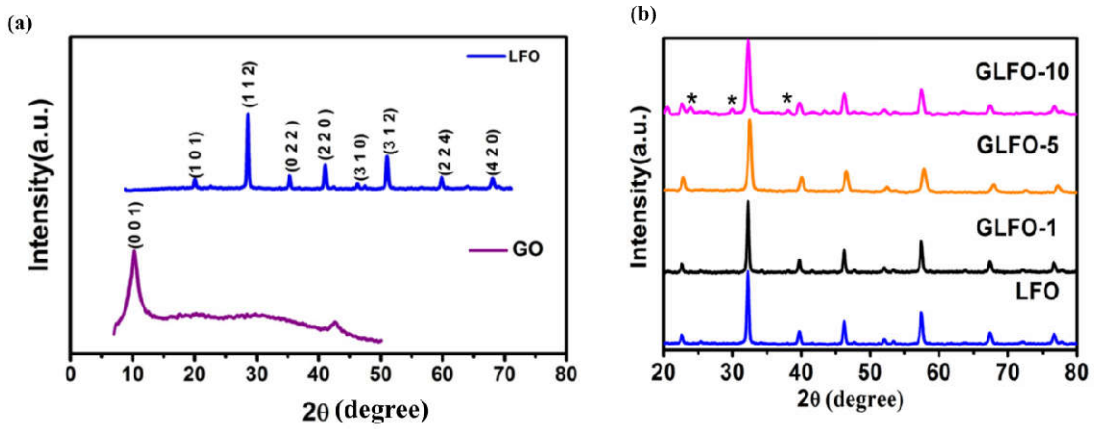

Fig. 4.1 XRD pattern of (a) GO and LFO (b) GLFO composites. The asterisk symbol peak in GLFO-10 indicates the presence of Fe_2O_3.

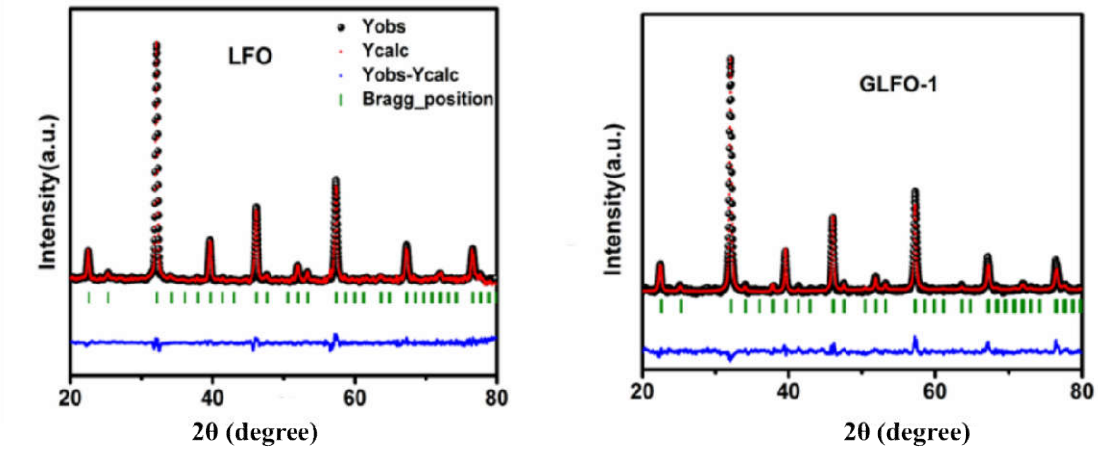

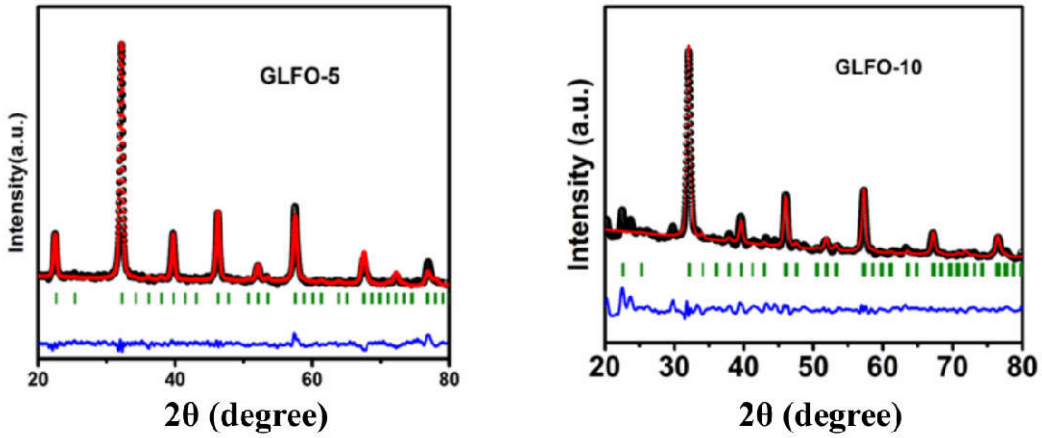

Fig. 4.2 Rietveld refinement patterns of LFO, GLFO-1, GLFO-5 and GLFO-10

Table 4.1 Rietveld refined parameters for LFO and GLFO composites

Parameters	LFO	GLFO-1	GLFO-5	GLFO-10
a (A^0)	5.56(7)	5.57(4)	5.55(4)	5.55(9)
b (A^0)	5.56(3)	5.57(7)	5.54(9)	5.57(6)
c (A^0)	7.86(8)	7.87(3)	7.85(1)	7.89(2)

4.3.2 Raman Spectroscopic Analysis

Raman spectroscopy is an efficient tool for the investigation of structural distortion and oxygen motion in the crystal structure. The orthorhombic structure with a *Pbnm* space group has total 24 Raman active modes, which are $7A_g \oplus 7B_{1g} \oplus 5B_{2g} \oplus 5B_{3g}$ [18].The Raman peaks obtained from crystalline LFO are shown in Fig. 4.3 (a). The main peaks of LFO at 431 cm^{-1} and 626 cm^{-1} originated from the stretching of the Fe-O bond. The symmetry corresponding to these peaks are A_g and B_{1g} respectively [19,20]. The band around 1304 cm^{-1} in LFO arises because of the second order vibration of the mode 626 cm^{-1} originated from the two-phonon scattering of O^{2-}. The Raman peak of LFO at ~1136 cm^{-1} is a mixture of B_{1g} excitations at 2(152+414) cm^{-1}. The variation in peak corresponding to A_g and B_{1g} peak in GLFO composite is shown in Fig. 4.3 (d). In GLFO-5 the peaks corresponding to A_g got shifted to 442 cm^{-1} and the B_{1g} peak is broadened and shifted to 678 cm^{-1}. Again, as

seen in Fig. 4.3 (b), the Fe-O bond vibration peaks show maximum shift for GLFO-5. Lattice strain due to expansion or compression of crystal structure leads to a shift in Raman peaks. Similarly, the broad peak around 1140 cm^{-1} in GLFO is a combination of 2(147+426) cm^{-1} peaks . An additional peak at 520 cm^{-1} in GLFO-5 is due to the silicon substrate. Among GLFO composites, the maximum lattice compression is expected for GLFO-5 as suggested by the highest shift. The broadened peak at 678 cm^{-1} shows splitting (as deconvoluted in Fig. 4.3 (c). The RGO concentration dependent changes in Raman peaks at 431 and 626 cm^{-1} originates from dissimilar distortions in the crystal structure.

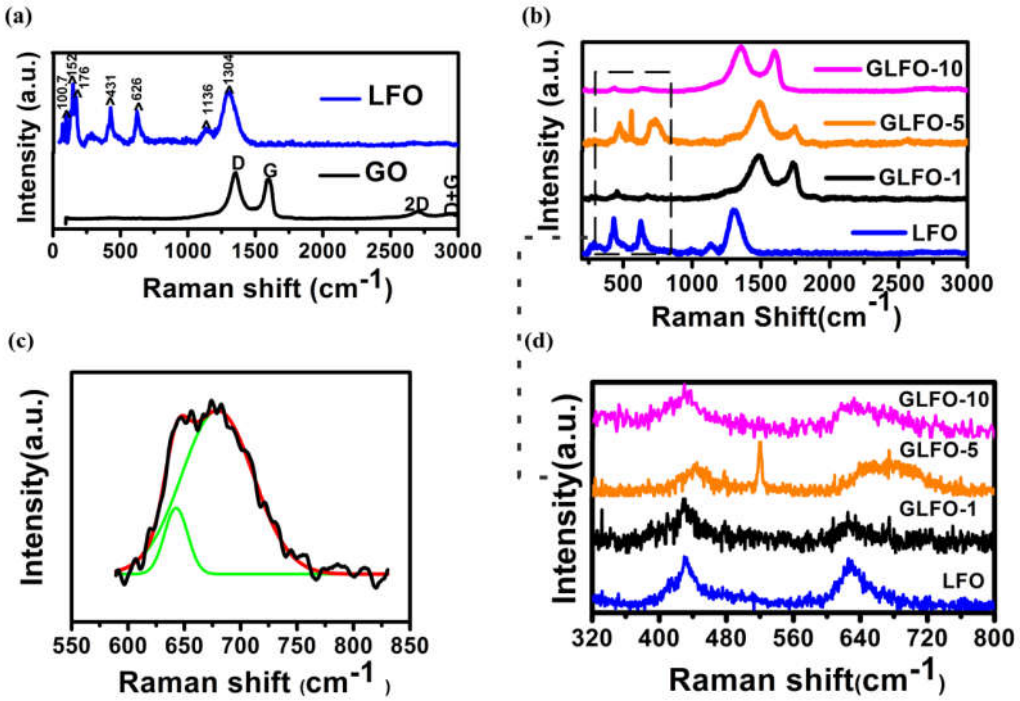

Fig. 4.3 Raman spectra of **(a)** LFO and GO **(b)** GLFO composite **(c)** deconvoluted Raman peak corresponding to Fe-O stretching bonds in GLFO-5 centered at 678 cm^{-1} and **(d)** Shift and broadening observed in Fe-O stretching vibration peaks of GLFO nanocomposites.

[Note: On the GLFO composites we have not taken the relative intensity between the peaks of LFO components and RGO components as significant information. The reason being that in micro Raman, we concentrate on a microscopic area. The selected microscopic area may not represent the compositional homogeneity in any nanocomposite structure.]

4.3.3. Scanning Electron Microscopy

The indication of effective functionalisation of LFO on RGO from the structural parameter (XRD) and the shift in Raman peaks is verified by FESEM analysis. The FESEM images of as synthesized LFO, GLFO-1, GLFO-5 and GLFO-10 nanocomposites are shown in Fig. 4.4 which evidently shows that LFO is successfully anchored on RGO.

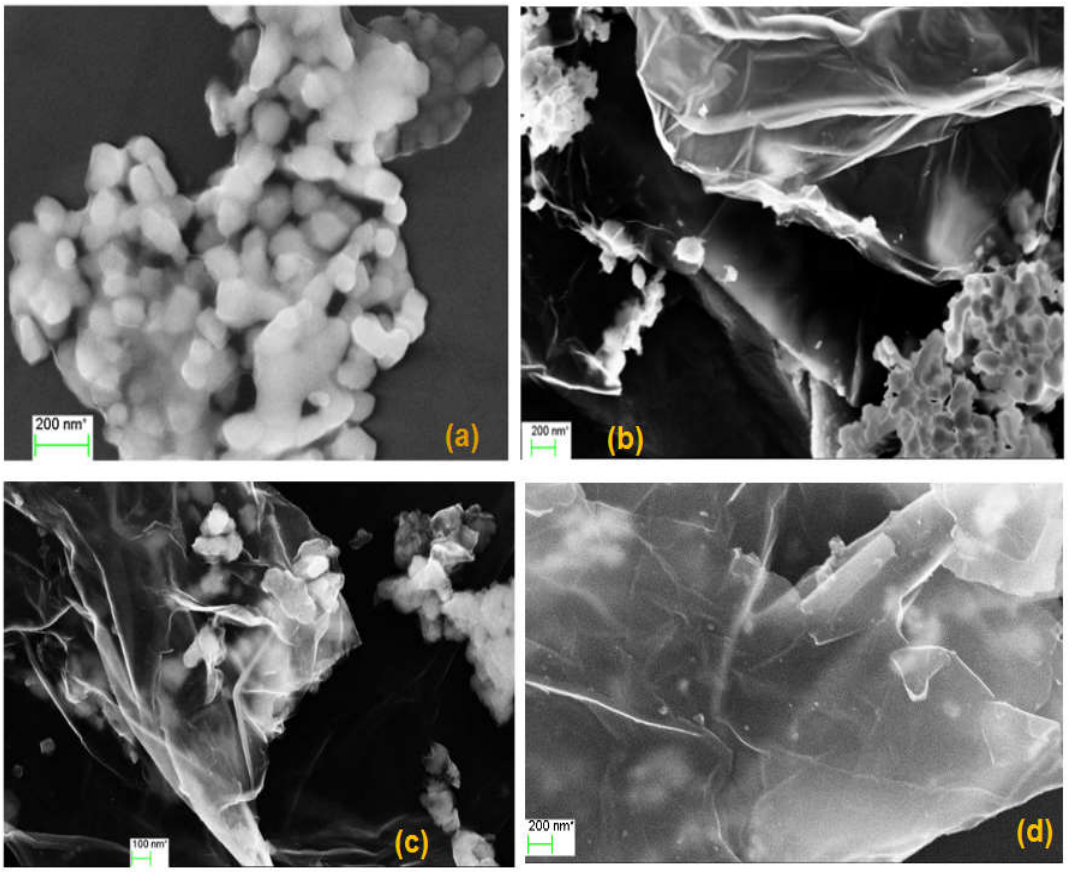

Fig. 4.4 FESEM images of **(a)** LFO **(b)** GLFO-1 **(c)** GLFO-5 and **(d)** GLFO-10

Thus, a graphene concentration dependent structural variation in GLFO composites is suggested by XRD pattern and confirmed by Raman spectroscopic analysis. Recently Yinlong Zhu *et al.* have studied the mechanism of tuning the cation deficiency in $LaFeO_3$ by utilising electrochemical investigations (OER and ORR) [21]. Also, Mefford *et al.*

have explored the effect of bond covalency on doped $LaCoO_3$ by studying effective electrolysis of water [22]. Therefore, the electrochemical investigations can be hypothesised as a technique to demonstrate the curious structural variations in GLFO composites.

4.3.4. Electrochemical Analysis

The electrochemical behavior of the RGO modified LFO was investigated by cyclic voltammetry (CV). The analysis was done in acetate buffer (0.1 M, pH 4.6) using three electrode assembly. The influence of ammonium (5m M AM) on the electrochemical behavior of modified electrodes (acetate buffer; scan rate: 50mV/s) is portrayed in Fig. 4.5. As seen, a higher activity is shown by the RGO nanocomposite (GLFO) modified electrodes compared to LFO. This can be attributed to the higher surface area and defect density offered by RGO and the consequent increase in the electronic transfer between the analyte and the electrode.

Among the different modified electrodes, the peak current exhibited an increasing trend from LFO up to GLFO-5 and then got dropped down in GLFO-10. Thus GLFO-5 shows a peak electrochemical activity towards the detection of ammonium. Fig. 4.5 (b) compares the CV of GLFO-5 with and without ammonium ions. The area under the curve shows an enhanced current density for GLFO-5 in presence of ammonium ions. The electrocatalytic action of GLFO-5 was further investigated at different scan rates in acetate buffer. As Fig. 4.5(c) shows, the redox peak current due to the diffusion controlled processes increase as the scan rate increases. To find out the current through the electrode, differential pulse voltammetry analysis has been carried out under 5mM ammonium solution and it is shown in Fig. 4.5 (d).

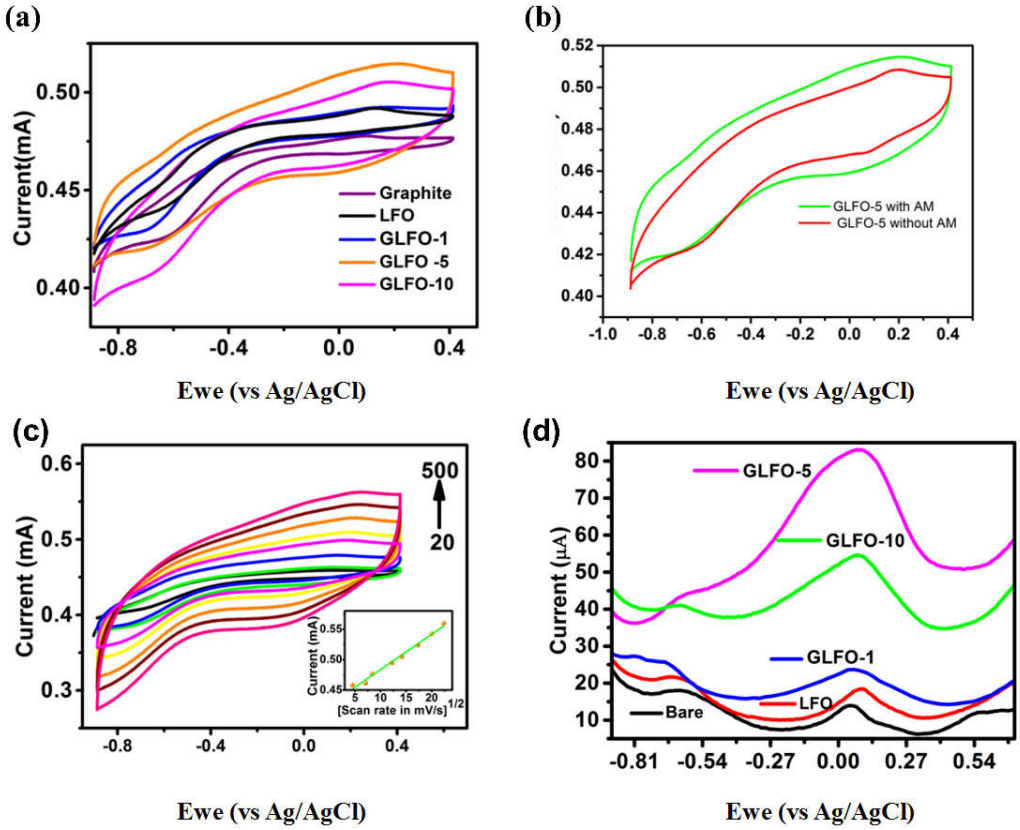

Fig. 4.5 (a) Cyclic Voltammograms (CV) of Graphite, LFO, GLFO-1, GLFO-5 and GLFO-10 electrodes in 5m M AM **(b)** CV of GLFO-5 with and without 5mM AM at scan rate: 50 mV/s **(c)** CV of GLFO-5 at different scan rates. Inset: Calibration curve of GLFO-5 **(d)** DPV curve of GLFO nanocomposite in presence of 5m M AM.

4.3.5. X-ray Photoelectron Spectroscopy

In order to understand the mechanism of enhanced sensitivity of GLFO-5 towards ammonium, the elemental analysis of the composite was carried out using X-ray photoelectron spectroscopy. The O1 XPS spectra in Fig. 4.6 are asymmetric in nature and suggest the presence of more than two chemical states of oxygen binding energies. The peak at 528.9 eV in LFO is assigned to the lattice oxygen Fe-O and La-O in the perovskite structure as shown in Fig. 4.6 (a) [23,24]. The peak centered at 531.1 eV and 533.7 eV is due to the adsorbed oxygen and adsorbed water respectively [25,26]. But the lattice

oxygen peak exhibited a shift up to 529.9 eV according to the concentration of RGO in the composite. The chemical shift indicates the influence of RGO on nature of metal-oxygen bond within the lattice. The evolutions of peaks corresponding to non-lattice oxygen components in GLFO were also analysed. In the graphene nanocomposite, peak at 531.08 eV is assigned to the oxygen doubly bonded to the aromatic carbon. The peak at 532.1 eV corresponds to the oxygen singly bonded with aliphatic carbon and the peak at 533.2 eV is assigned to oxygen singly bonded to aromatic carbon. The presence of intercalated adsorbed water molecule can be seen at 534.4 eV [27].

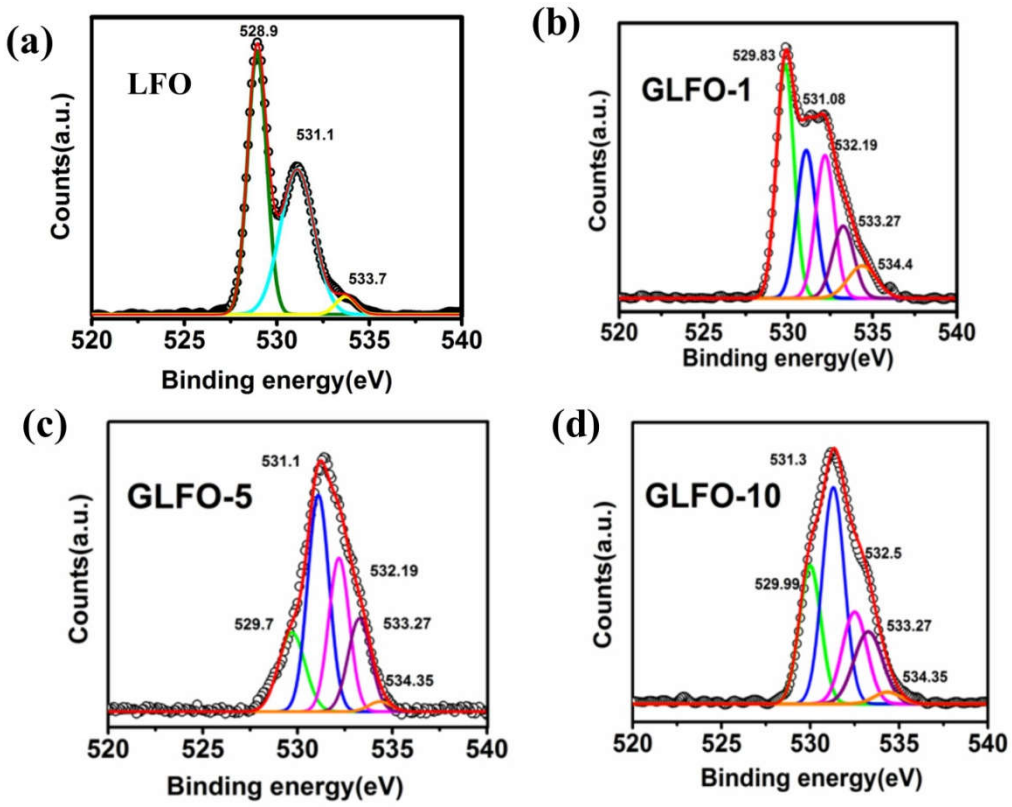

Fig. 4.6 The O1 core level XPS spectrum from (a) LFO, (b) GLFO-1, (c) GLFO-5 and (d) GLFO-10 nanocomposites.

4.4 Discussion

Therefore, GLFO nanocomposite shows a distinct RGO concentration dependence as observed in XRD and confirmed by Raman spectra results. Also, the dependence is clearly demonstrated by the electrochemical studies and XPS based elemental analysis on GLFO. A further task is to develop an understanding of underlying reasons for the highest dependence of RGO concentration on the intriguing behavior of GLFO-5.

Fig. 4.8 shows unit cell structure of LFO and various GLFO compounds plotted based on refined values from the Rietveld analysis. The analysis indicates that the incorporation of RGO played a critical role in tuning the extent of change in size, shape and co-operative tilting of octahedra. This change, in turn,can affect the electronic environment of ferrite metal ions in LFO.

4.4.1 Change in Fe-O Bond Length and Fe-O-Fe Bond Angle: The change in size and shape of octahedra was studied based on the change in Fe-O bond length and bond angle. The notations of different Fe-O bonds are shown in Fig. 4.7. The effect of RGO on the bond length of Fe-O as shown in Table 4.2 indicates a clear dependence of the size and shape on RGO concentration. The O^{2-} ligands attached with the Fe metal ion in LFO offer an electronic cloud distribution. In the case of LFO in GLFO composites, a cumulative effect of (1) electron rich functional groups in RGO and (2) the π electron cloud from sp^2 bonded carbon in RGO produces an additional electric field over the Fe metal ions. The change in bond length modifies the overlap between the 3*d* orbitals of ferrite ion and 2*p* orbitals of oxygen ions, leading to change in electronic conductivity. Other than shape changes of the octahedra, Fig. 4.8 emphasizes an inter-octahedral tilt and rotation through Fe-O-Fe in GLFO

compared to LFO. The angle $\Theta_{B\text{-}O\text{-}B}$ measures the tilting of the octahedron which is directly related to the cell distortion in the crystal structure. Ferrite ion is attached to six other octahedra through the Fe-O bond. So a small tilt in one FeO_6 octahedron leads to a distortion in the whole crystal structure of the perovskite material. Other than bond length, the tilting also affects the orbital overlapping. Table 4.2 consolidates the overall variation of $\Theta_{Fe\text{-}O\text{-}Fe}$ with the concentration of RGO. It indicates that GLFO-5 has the maximum deviation (decrease) in Fe-O-Fe angle and has a maximum rotation with respect to LFO. Fig. 4.8 (e) shows the individual O-Fe-O angles in single octahedron of GLFO-5 and LFO. It clearly demonstrates the enhanced distortion even in an individual octahedron of GLFO-5 in comparison to that in LFO. This enhancement is entirely contributed by graphene.

Table 4.2 Structural parameters of octahedron formed in LFO and GLFO composites

Nanocomposite				
LFO		GLFO-1	GLFO-5	GLFO-10
Bond length:				
Fe-O1(x2)	2.01	1.99	1.98	2.35
Fe-O21(x2)	2.02	2.05	1.97	2.19
Fe-O22(x2)	1.99	2.02	2.27	1.75
Bond angle:				
Fe-O-Fe	157.6	150.3	135.6	170.1

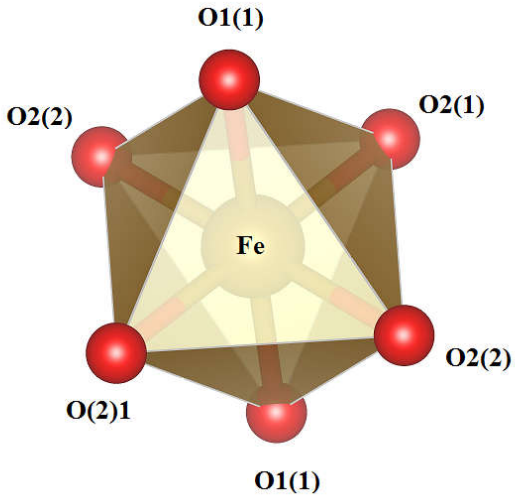

Fig. 4.7 Notations of different Fe-O bonds in octahedra.

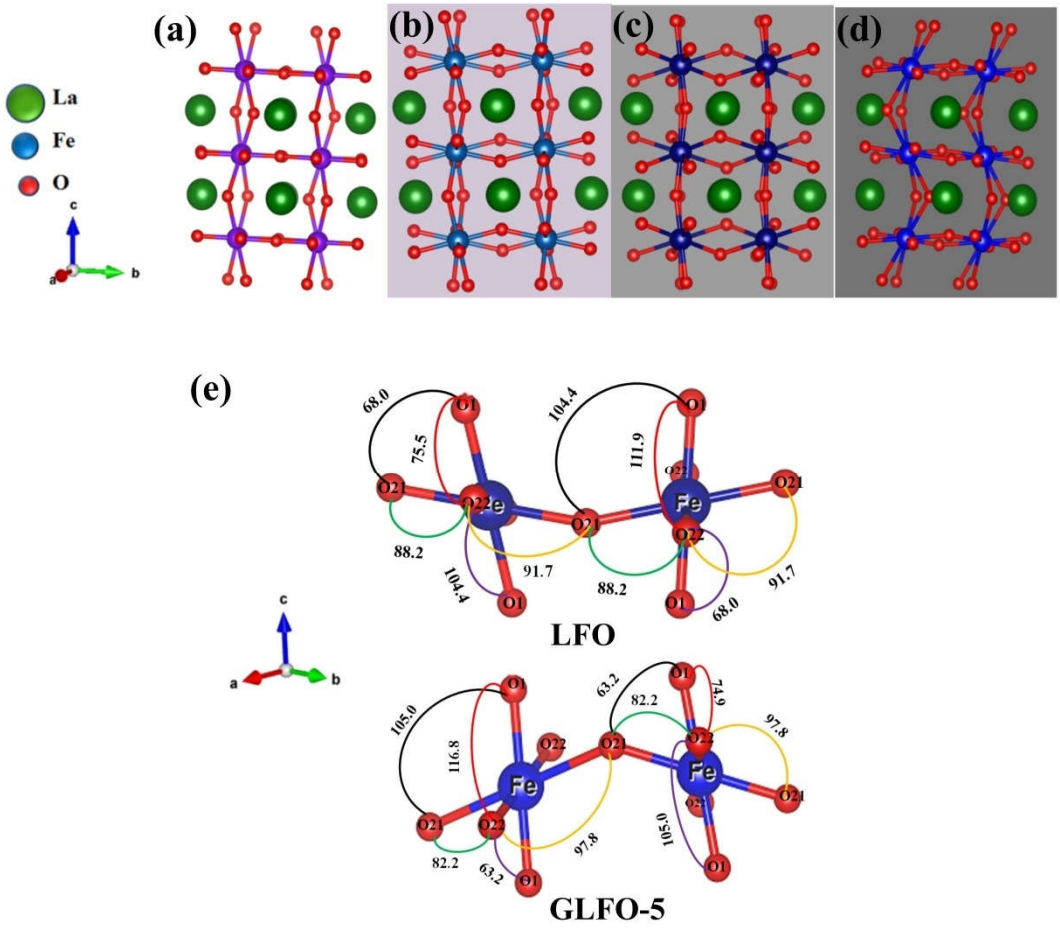

Fig. 4.8 Structure of (a) LFO (b) GLFO-1 (c) GLFO-5 (d) GLFO-10. (The darkness of the background symbolizes relative concentration of RGO) (e) O-Fe-O bond angles of individual octahedron in LFO and GLFO-5

The noted change in bond length and angle can together be categorised as a distortion of the LFO perovskite. This distortion is clearly dependent on the graphene concentrationand, therefore, this remarkable effect can be coined with a new phrase *"Graphenostortion"*.

4.4.2 Change in Bond Covalency: The electronic interactions play an important role in the distortion of a crystal lattice [28]. Based on the pseudo-JahnTeller effect an octahedral tilting could be implicitly generated by the change in bond covalency of the cation-anion bonds. Cammarata A. and Rondinelli J.M. report that the rotational angle and bond length imparts perturbations to the bond covalency of the composites [29]. Thus, the change in bond angle and bond length leading to an octahedral tilting simultaneously can lead to a change in bond covalency. Again, the bond covalency of the metal-oxygen bond is directly related to the bond valency [30]. The bond valency obtained for LFO, GLFO-1, GLFO-5 and GLFO-10 using SPuDS calculation is 3.12, 2.98, 2.70 and 3.08 respectively [31]. As noted, the GLFO-5 has the lowest bond valency among GLFO composites and therefore the exhibited highest conductivity is expected. On further analysis specifically on bond valencies of ferrite ion of different Fe-O bonds, it was found that within GLFO-5, the Fe-O(2)1 bond could offer the best conductivity path. Clearly, in GLFO, the charged atmosphere offered by RGO led to change in covalency of the dispersed phase.

4.4.3 Verification of Distortion by Raman Spectra: The frequency shift observed in Raman spectra (Fig. 4.3 (b)) can be ascribed to the fact that the structural distortion affects the phonon-phonon interaction. The broadening of B_{2g} mode at region 680 cm^{-1}(Fig. 4.3 (c) and (d)) could indicate the presence of different oxygen species in the lattice. This can induce a change in polaraisability of oxygen ions leading to deviation in bond covalency.

4.4.4 Distortion and Non-lattice Oxygen: Based on XPS, the effect of concentration of RGO is reflected in the concentration of lattice and non-lattice oxygen (Table 4.3). Further analysis of Fe 2*p* peaks gives an idea that the interaction of reactive sites of GO with LFO induces a conversion of Fe^{2+} into Fe^{3+}ions which is shown in Fig. 4.9 and consolidated in Table 4.3.The fluctuation in B-site metal cation in LFO implies the non stochiometric nature of the synthesized sample. The oxygen species from RGO attack the oxygen deficiency created by the Fe^{2+} ions within the crystal lattice. Mutually complementary effect of conversion of metal cation oxidation state and occupancy of non-lattice oxygen in the crystal influences the bond covalency of the metal-anion bonds. This affects a change in the size and shape of an octahedron. As noted in Table 4.3, the ratio of non-lattice oxygen to the lattice oxygen shows an increase with RGO concentration. This increase can be attributed to the oxygen offered by the functional groups of RGO. Beyond GLFO-5, the perovskite lattice can be assumed to be reluctant to accommodate more Fe^{3+}ions in the lattice. Indicating the effect, the XRD spectrum shows the presence of Fe_2O_3 in the GLFO-10 composite. Simultaneously one can assume the presence of new oxygen species interacting with the dispersed phase of GLFO-5 as indicated by broadening in the Raman spectrum (Figure 4.3 (c) & (d)). The new oxygen species can be identified with the non-lattice oxygen. As also indicated by Raman spectra metal–lattice oxygen (Fe-$O_{lattice}$) bond covalency must have been influenced by the occurrence of non-lattice oxygen. Thus, RGO concentration dictated the percentage concentration of non-lattice oxygen.

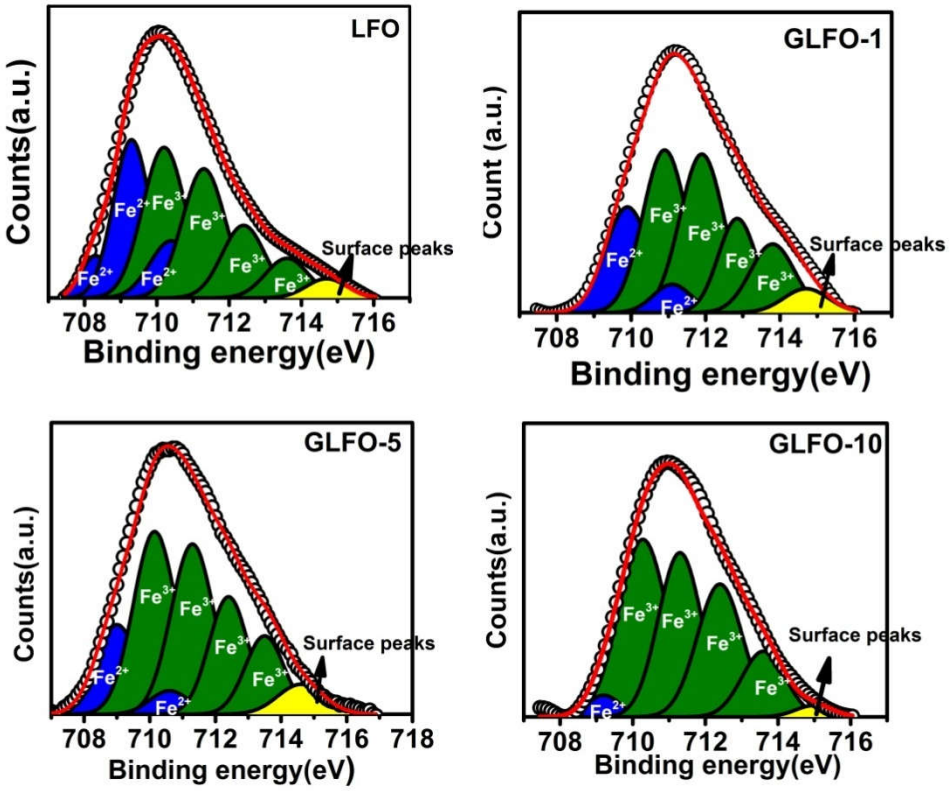

Fig. 4.9 The Fe (*2p*) core level XPS spectrum from (a) LFO (b) GLFO-1 (c) GLFO-5 and (d) GLFO-10 nanocomposites.

Table 4.3 RGO dependent elemental concentration in LFO and GLFO nanocomposite

Sample	Percentage concentration			
	Fe^{2+}	Fe^{3+}	lattice oxygen	non-lattice oxygen
LFO	36	64	49	51
GLFO-1	22	78	34	66
GLFO-5	17	83	17	83
GLFO-10	3	97	24	76

The schematic representation of possible mechanism for the distortion in LFO driven by graphene or "Graphenostortion" is shown in Fig. 4.10.

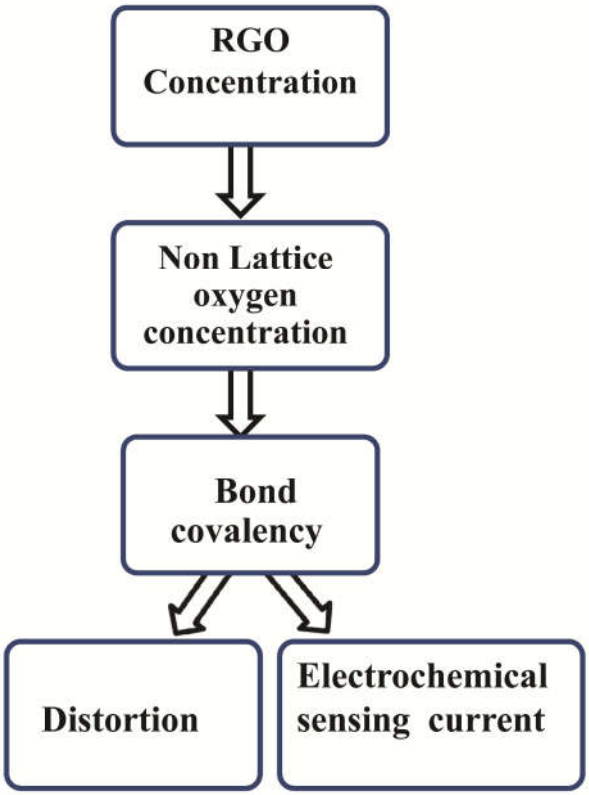

Fig. 4.10 Schematic representation of a possible mechanism for the distortion in LFO driven by graphene ("Graphenostortion").

4.4.5 Effect of Distortion on Electrochemical Conductance: Commenting specifically on ammonium sensitivity, the interaction of ammonium ions with the non-lattice oxygen within the composite determines the electrochemical activity. The interaction is in agreement with the following empirical formula of the reaction.

$$NH_4^+ + H_2O \rightleftharpoons NH_3 + H_3O^+$$

$$2NH_3 + 3O^-_{nonlattice} \rightarrow N_2 + 3H_2O + 3e^-$$

The XPS analysis paved the way to find a connection between the highest current sensitivity in GLFO-5, oxygen concentration and the distortion impelled by RGO. GLFO-5 has the highest amount of non-lattice oxygen (Table 4.3). Remarkably, Fig. 4.11 suggests proportionality between the concentrationof non-lattice oxygen and the sensing current. Therefore, the electrochemical conductance can be assumed to be fundamentally driven by the quantity of non-lattice oxygen in the composite.

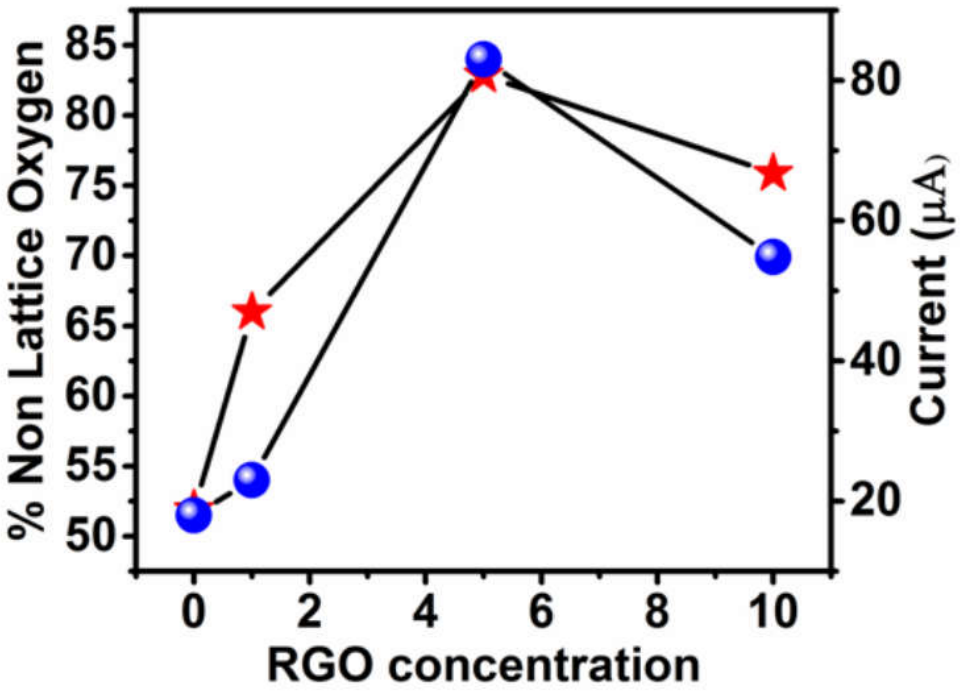

Fig. 4.11 Variation of sensing current (dot) and percentage of non-lattice oxygen (star) with a concentration of RGO.

The present work indicates a possible mechanism of RGO interaction on orthorhombic crystals. The change in the physicochemical properties of the graphene-LFO composite can be attributed to the structural features of LFO, distribution of LFO on graphene sheets and the interfacial bonding between RGO and LFO. The synergistic effect between graphene and LFO in GLFO-5 among other RGO varied nanocomposites are explained on the basis of

conversion of Fe^{2+} to Fe^{3+} ion created by the oxygen species. Thus, the modified bond covalency emerged due to the conversion of metal cation oxidation state, induced by the percentage of non-lattice concentration, has a key role in determining the distortion and regulation of electrochemical conductivity of the nanocomposite.

4.5 Conclusion

In summary, the distortion in perovskite $LaFeO_3$ is regulated by dispersing it over RGO matrix. Graphene induced structural distortion (Graphenostortion) on perovskite crystal structure is studied in detail. A series of graphene concentration varied interface were synthesized *via* hydrothermal method. The crystal distortion was indicated by XRD spectra and was verified by Raman spectroscopic studies. The structural deviations were quantified with the help of Rietveld refinement analysis and it indicates that the nanocomposite with 5:10 ratio of GO to LFO shows higher deviation compared to LFO. The effect of distortion was demonstrated using electrochemical sensing studies on ammonium. By analysis of the oxygen and Fe ion peaks of XPS, along with Raman spectra, a clear understanding of the concentration of GO dependent distortion process was developed. The environment for the graphenostrotion originated from the interaction of oxygen functional groups of RGO with LFO. The non-lattice oxygen influence a change in concentration of Fe^{2+} and Fe^{3+} ions within the GLFO composite. Thus, the variation in bond covalency influenced by the percentage concentration of non-lattice oxygen in the composite creates inter octahedral and intra octahedron distortion and dictates the electrochemical conductivity. Graphenostortion opens up a new pathway for understanding the dynamics of metal cations and oxygen anions in perovskite. In addition, RGO as a tool to control the distortion in metal oxide could facilitate new spheres in technological applications of graphene.

4.6 References

[1] M.A. Peña, J.L.G. Fierro, Chemical Reviews. 101 (2001) 1981–2018.

[2] Z. Xia, K.R. Poeppelmeier, Accounts of Chemical Research. 50 (2017) 1222–1230.

[3] I.H. Inoue, Semiconductor Science and Technology. 20 (2005) S112–S120.

[4] J.M. Rondinelli, S.J. May, J.W. Freeland, MRS Bulletin. 37 (2012) 261–270.

[5] I. Natali Sora, T. Caronna, F. Fontana, C. de Julián Fernández,Journal of Solid State Chemistry. 191 (2012) 33–39.

[6] K. Nomura, S. Tanase, Solid State Ionics. 98 (1997) 229–236.

[7] H. Hayashi, , Solid State Ionics. 122 (1999) 1–15.

[8] A.T. Zayak, X. Huang, J.B. Neaton, Physical Review B. 74 (2006) 1-11.

[9] V.S. Bhadram, D. Swain, R. Dhanya *et al.*, Materials Research Express. 1 (2014) 026111-12.

[10] D. Kan, R. Aso, H. Kurata *et al.*, APL Materials. 3 (2015) 062302-9.

[11] R. Aso, D. Kan, Y. Shimakawa *et al.*, Scientific Reports. 3 (2013) 2214-6.

[12] M. Zhang, Z. Wang, Applied Physics Letters. 102 (2013) 213104-5.

[13] Z. Li, Y. Shen, Y. Guan, Jornal of Material Chemistry A. 2 (2014) 1967–1973.

[14] Y. Yuan, Z. Dong, Y. Li *et al.*, Progress in Natural Science: Materials International. 27 (2017) 88–92.

[15] X. Feng, Y. Fan, N. Nomura, Carbon. 112 (2017) 169–176.

[16] G. Volonakis, F. Giustino, The Journal of Physical Chemistry Letters. 6 (2015) 2496–2502.

[17] L. Sangaletti, L.E. Depero, B. Allieri, Journal of the European Ceramic Society. 21 (2001) 719–726.

[18] M. Popa, Solid State Ionics. 154–155 (2002) 437–445.

[19] J. Andreasson, J. Holmlund, R. Rauer *et al.*, Physical Review B. 78 (2008) 23510-13.

[20] L. Martín-Carrón, A. de Andrés, The European Physical Journal B. 22 (2001) 11–16.

[21] Y. Zhu, W. Zhou, J. Yu, Chemistry of Materials. 28 (2016) 1691–1697.

[22] J.T. Mefford, X. Rong, A.M. Abakumov *et al.*, Nature Communications. 7 (2016) 11053-11.

[23] S. Thirumalairajan, K. Girija, V. Ganesh *et al.*, Crystal Growth & Design. 13 (2013) 291–302.

[24] S. Phokha, S. Pinitsoontorn, S. Maensiri, Journal of Sol-Gel Science and Technology. 71 (2014) 333–341.

[25] A. Celebioglu, S. Vempati, C. Ozgit-Akgun, RSC Adv. 4 (2014) 61698–61705.

[26] W. Ponhan, V. Amornkitbamrung, S. Maensiri, Journal of Alloys and Compounds. 606 (2014) 182–188.

[27] B. Gupta, N. Kumar, K. Panda *et al.*, Scientific Reports. 7 (2017) 1-14.

[28] P. Garcia-Fernandez, J.A. Aramburu, M.T. Barriuso *et al.*, The Journal of Physical Chemistry Letters. 1 (2010) 647–651.

[29] A. Cammarata, J.M. Rondinelli, The Journal of Chemical Physics. 141 (2014) 114704-10.

[30] Z.J. Wu, Q.B. Meng, Chinese Journal of Chemistry. 17 (2010) 108–113.

[31] http://www.unf.edu/~michael.lufaso/spuds.

CHAPTER 5

Effect of interface on optical properties of perovskite $LaFeO_3$

Here strain induced by an external matrix like reduced graphene oxide (RGO) on the crystal structure of $LaFeO_3$ (LFO) and its related optical properties are investigated. Variations in lifetime, fluorescence intensity and photocatalytic activity of GLFO composites are explained in terms of intermediate bands produced by RGO and associated radiationless transitions of photoexcited electrons.

5.1 Introduction

Perovskite nanomaterials are one of the promising materials in the 21stcentury. They are recently demonstrated as an emerging material in optoelectronics [1]. Their superior properties enable them to find application in photovoltaic and light emission applications. Moreover, among optical properties, the presence of broad absorption spectrum and tuneable intense emissions (quantum yield ~ 10-90 %),make them useful in multicolor biological imaging [2].

Ferrite materials are very active and highly reactive, among them, rare-earth orthoferrites with ABO_3 crystal structures are well known for their shape related material properties [3–5]. The size of the rare earth metal oxide in the perovskite has an important role. The size determines the octahedral tilting which leads to the strain in the crystal structure. As the ionic radius of rare-earth metal increases, the octahedral tilting angle also increases resulting in a less distorted structure. In comparison to cubic structure perovskites, the rare earth perovskites which adopt orthorhombic perovskite geometry, allows highly substitutable cation sites, widening its scope to be tuned for specific applications [6].

One of the members viz, Lanthanum orthoferrite, $LaFeO_3$ (LFO) has peculiar physico-chemical properties making it suitable for advanced technologies like solid oxide fuel cell, catalyst, chemical sensors, and biosensors. They exhibit mixed conductivity i.e., a combination of electronic and ionic conductivity significant for its performance in technological applications [7].Various properties of the perovskite LFO is also related to the crystal defects. La is the smallest element with ionic radius - 1.87 Å in the rare earth family. The size effect of La is also one of the reasons for the observed distortion in the synthesised LFO. Mainly the defects generate fluctuations between the oxidation states of the iron which leads to the

insertion of O_2 from the environment or creation of oxygen vacancies [8]. Their surface area along with the interfacial state makes it useful in catalytic applications [9]. LFO and its composites are explored widely as a visible-light active photocatalyst.

C. Bhandari *et al*., have theoretically predicted the strain induced variation in optical properties of a perovskite compound $NaOsO_3$. They reported that the epitaxial strain changes the crystal structure of octahedral symmetry by varying the octahedral rotation angle and Os-O bond length. The theoretical study suggests a shift in the band gap and associated optical transitions [10]. As we have reported in the previous work, the RGO can effectively introduce additional strain into LFO. There the RGO induced distortion in octahedral symmetry was evaluated utilising electrochemicalmethod.

In this chapter we are exploring the effect of strain on the optical properties of the perovskite, LFO using two relevant experimental techniques, UV-Visible spectroscopy, and fluorescence spectroscopy. In addition, the effect of the strain induced optical properties of perovskite on its photocatalytic efficiency is investigated.

5.2 Materials and Methods

The detailed description of the synthesis of GLFO nanocomposite is given in section Chapter 3 (section 3.1.1, 3.2.1 and 3.4.1). As detailed in section 3.4.1 the nomenclature of the different samples are GLFO-1, GLFO-5 and GLFO-10 where the mass ratio between GO to LFO is varied as 1:10, 5:10, and 10:10.

5.2.1 Characterisation

UV-Vis DRS reflectance spectra (JASCO-V-750 spectrometer) was used to evaluate the electronic transitions and the band gap of the materials. Fluorescence of the material was analysed using FLUROLOG (Horiba) with 325 nm as the excitation wavelength.

Photocatalytic activity studies: Degradation of rhodamine (RhB) was used to analyse the photocatalytic activity of the sample. The catalyst was dispersed at a concentration of 20 mgL^{-1} into 1.25 mgL^{-1} dye solution. The resulting solution was stirred in dark for one hour for attaining the adsorption-desorption equilibrium. The activity studies were performed under Xenon arc lamp (300 W) replicating the solar spectrum. The intensity spectra of Xenon-arc lamp is given in Fig. 5.1.

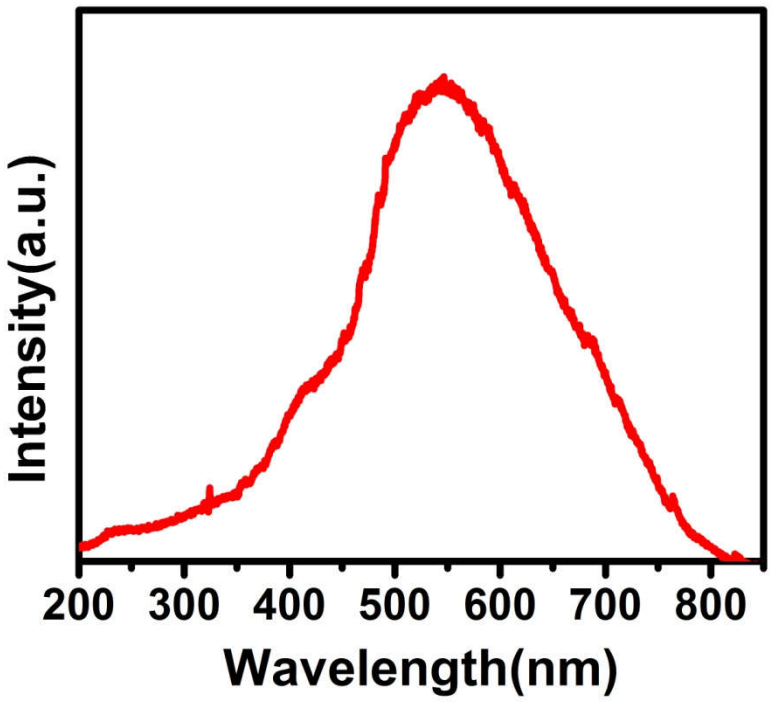

Fig. 5.1 Intensity spectra of Xenon-arc lamp used in this thesis work

5.3 Result and Discussion

5.3.1 Strain Calculation

The strain is an outcome of distortion associated with the crystal structure. Here the strain associated with the effect of the interface on the perovskite sample is assimilated. The Synthesised samples were characterised by XRD for phase analysis and crystalline purity is shown in section 4.3.1 (Chapter 4). The XRD plot of GLFO-10 sample shows an extra peak of Fe_2O_3. The peak shift and broadening corresponding to the highest intensity plane *viz*. (121) plane of the *pbnm* orthorhombic structure is shown in Fig. 5.2. Increasing the concentration of RGO led to a strain in the internal crystal structure of LFO and it is observed as a shift to higher 2θ value in the XRD pattern. The shift is most prominent in GLFO-5 sample. As mentioned, the theoretical study on the optical properties $NaOsO_3$ perovskite is reported to have a strong connection with the strain [10,11]. Therefore the observed shift in the peak position and broadening is investigated for its origin from size and strain effect.

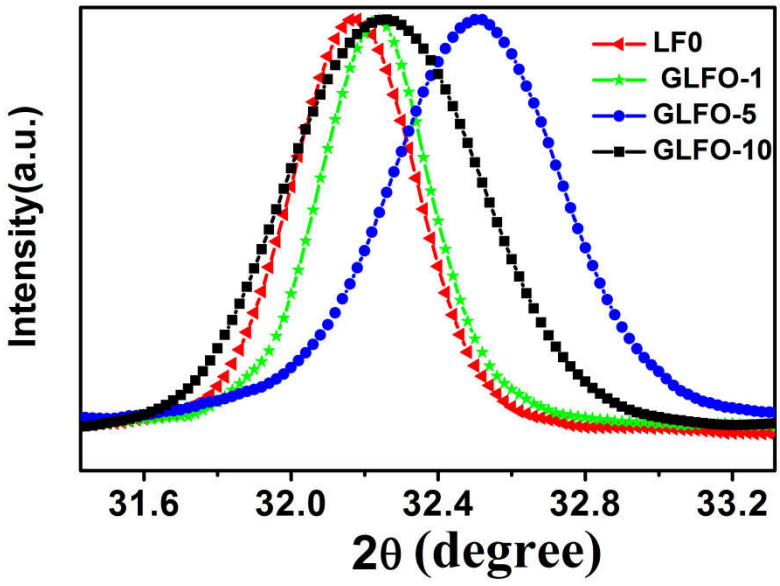

Fig. 5.2 Variation in (121) XRD peak of LFO,GLFO-1,GLFO-5, and GLFO-10

5.3.2 Particle Size and Strain Calculation- W-H method

The measured peak width ($\beta_{measured}$) observed in the composite is a combination of instrumental broadening and sample broadening. The instrumental broadening is calculated using the standard samples (eg. Silicon) [12]. The sample broadening β_{hkl} is estimated using the expression:

$$\beta_{hkl} = [\beta^2_{measured} - \beta^2_{standard}]^{1/2}$$

Williamson-Hall modified the Scherrer equation to relate the strain and the Bragg angle θ as $\varepsilon = \beta_{hkl} / \tan\theta$. The modified equation is $\beta_{hkl}\text{Cos}\theta = \frac{K\lambda}{D} + 4\varepsilon\,\text{Sin}\theta$, where the strain (ε) is isotropic in nature. This is called uniform deformation model (UDM) [13]. The W-H plot for all the samples are shown in Fig. 5.3. The size of the particle and strain is calculated from intercept and slope respectively. The tabulated strain is shown in Table 5.1.

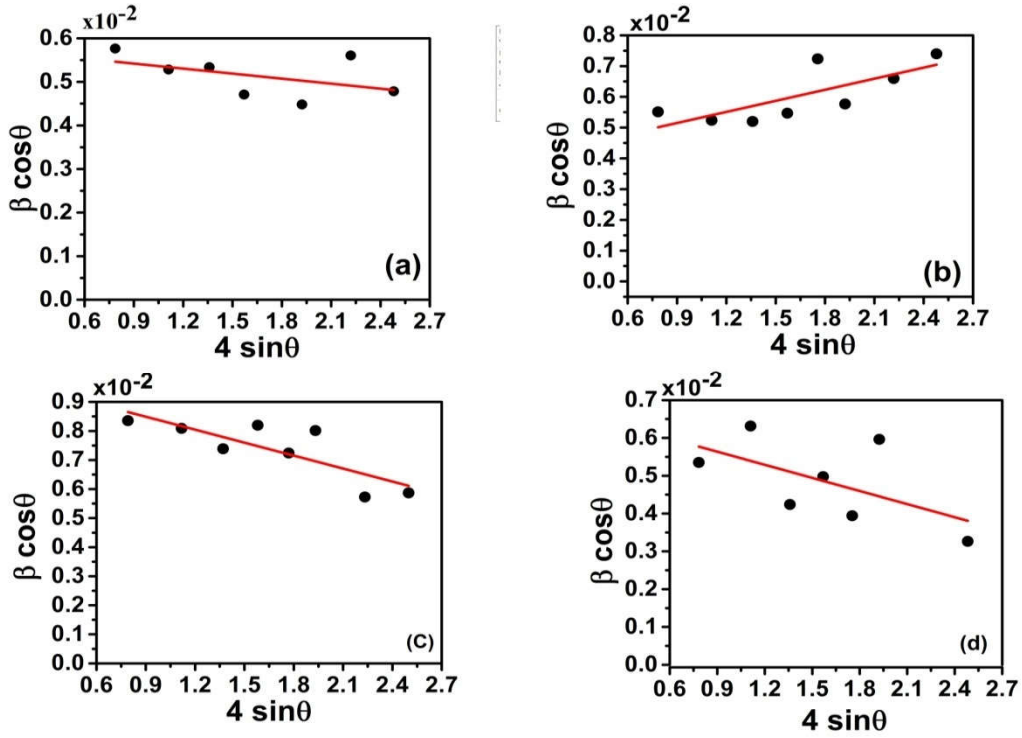

Fig. 5.3 W-H plot of (a) LFO (b) GLFO-1 (c) GLFO-5 and (d) GLFO-10

5.3.3 Size-Strain Plot (SSP)

Size-strain effect for an isotropic strain can be calculated from SSP using the following equation,

$$(d_{hkl}\,\beta_{hkl}\cos\theta)^2 = \frac{K}{D}(d_{hkl}^2\,\beta_{hkl}\cos\theta) + \left(\frac{\sigma}{2}\right)^2$$

Where K is a constant depending on the shape of the particle. The apparent strain is obtained from σ which is related to the root mean square strain as $\varepsilon = \sigma/(8\pi)^{1/2}$ [14]. The plot of $(d_{hkl}\,\beta_{hkl}\cos\theta)^2$ vs $(d_{hkl}^2\,\beta_{hkl}\cos\theta)$ is a straight line whose slope and the y-intercept gives the particle size and strain in the crystal respectively. The SSP for LFO and GLFO composites are shown in Fig. 5.4. The estimated strain in the samples is listed in Table 5.1. It can be inferred that the strain induced in the crystal structure is depended on the amount of RGO. Maximum strain is obtained for GLFO-5 sample, *i.e.*, the probability of crystal distortion is higher in GLFO-5 and it is evident from peak shift in XRD. But the observed lesser strain in GLFO-10 can be attributed to the relaxation offered by the formation of the extra phase of Fe_2O_3 during GLFO-10 synthesis. The variation in distortion and therefore the strain in the crystal structure can significantly alter the physico-chemical properties especially the optical properties of the material.

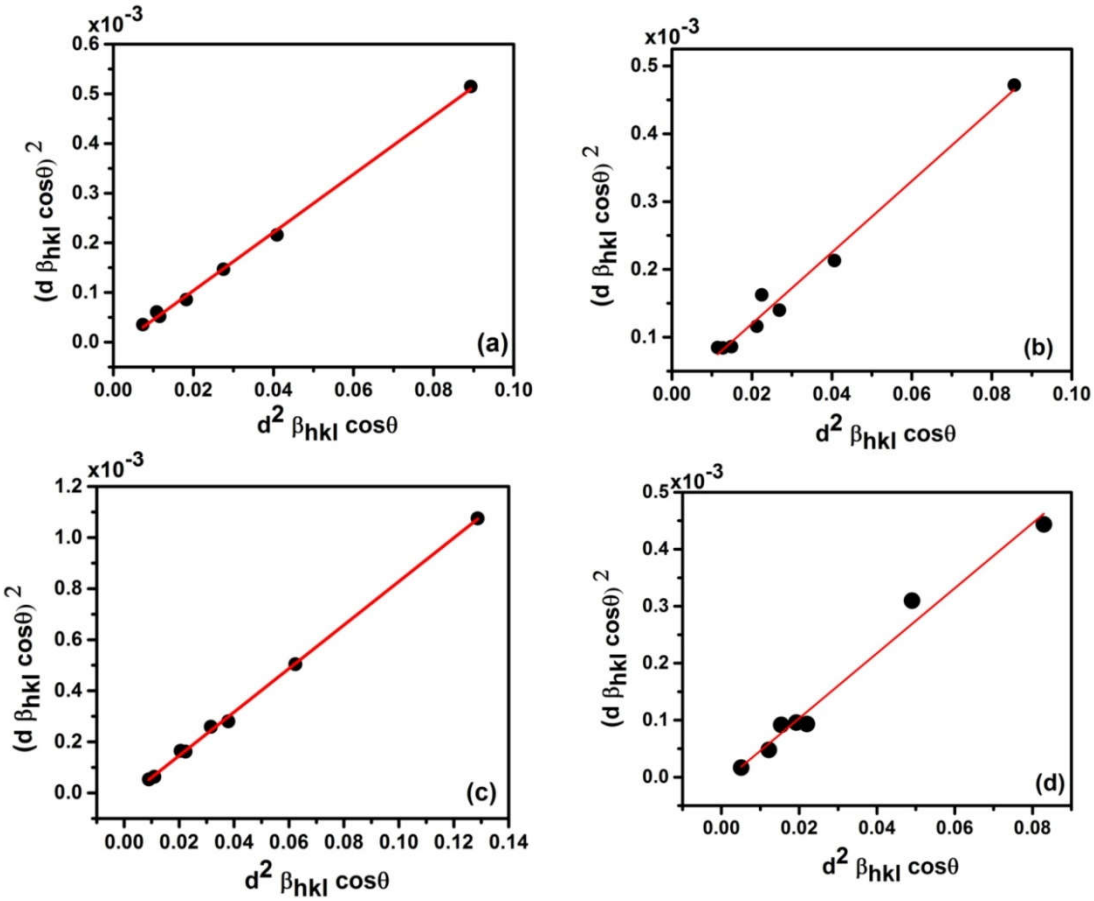

Fig. 5.4 Size-Strain Plot of (a) LFO (b) GLFO-1 (c) GLFO-5 and (d) GLFO-10

Table.5.1. Strain calculated from Size-Strain plot and W-H Plot

Sample	S-SPlot		W-H plot	
	D(nm)	Strain (no unit x10^{-3})	D(nm)	Strain (no unit x10^{-3})
LFO	22.8	1.46	23.7	0.38
GLFO-1	25.3	1.52	33.6	1.20
GLFO-5	15.6	1.89	13.9	1.50
GLFO-10	23.3	1.32	20.5	1.16

5.4 Optical Properties

5.4.1 UV-Vis Diffuse Reflectance Spectra

The UV-Vis Diffuse reflectance spectra of the samples are shown in Fig. 5.5 (a). Three types of electronic transitions are generally reported in optical absorption spectra of Fe^{3+} located in octahedral symmetry: (1) d-d inter-atomic transitions (2) *2p-3d* charge transfer and (3) pair excitations of adjacent Fe^{3+} ions [15]. The UV-Vis absorption peak in LFO generally arises due to the charge transfer in O (*2p*) →Fe (*3d*) electronic state. Moreover, in LFO, an additional absorption band at around 700 nm is clearly evident. These absorptions are usually associated with the promotion of an electron from the localised orbital of one atom to the higher energy level of the same atom. Therefore, it arises from the intra-atomic Fe *3d-d* transitions; that is $^6A_{1g} \rightarrow {}^4T_{2g}$ transition in octahedral Fe^{3+} [16]. With the increase in the concentration of RGO, the peak around 700 nm disappears, denoting a fluctuation in Fe^{3+} oxidation state while introducing RGO. The absorption peak around 500 nm arises due to the double excitation of Fe-Fe pair corresponding to $^6A_1 + {}^6A_1 \rightarrow {}^4T_1(^4G) + {}^4T_1(^4G)$ transitions [17].

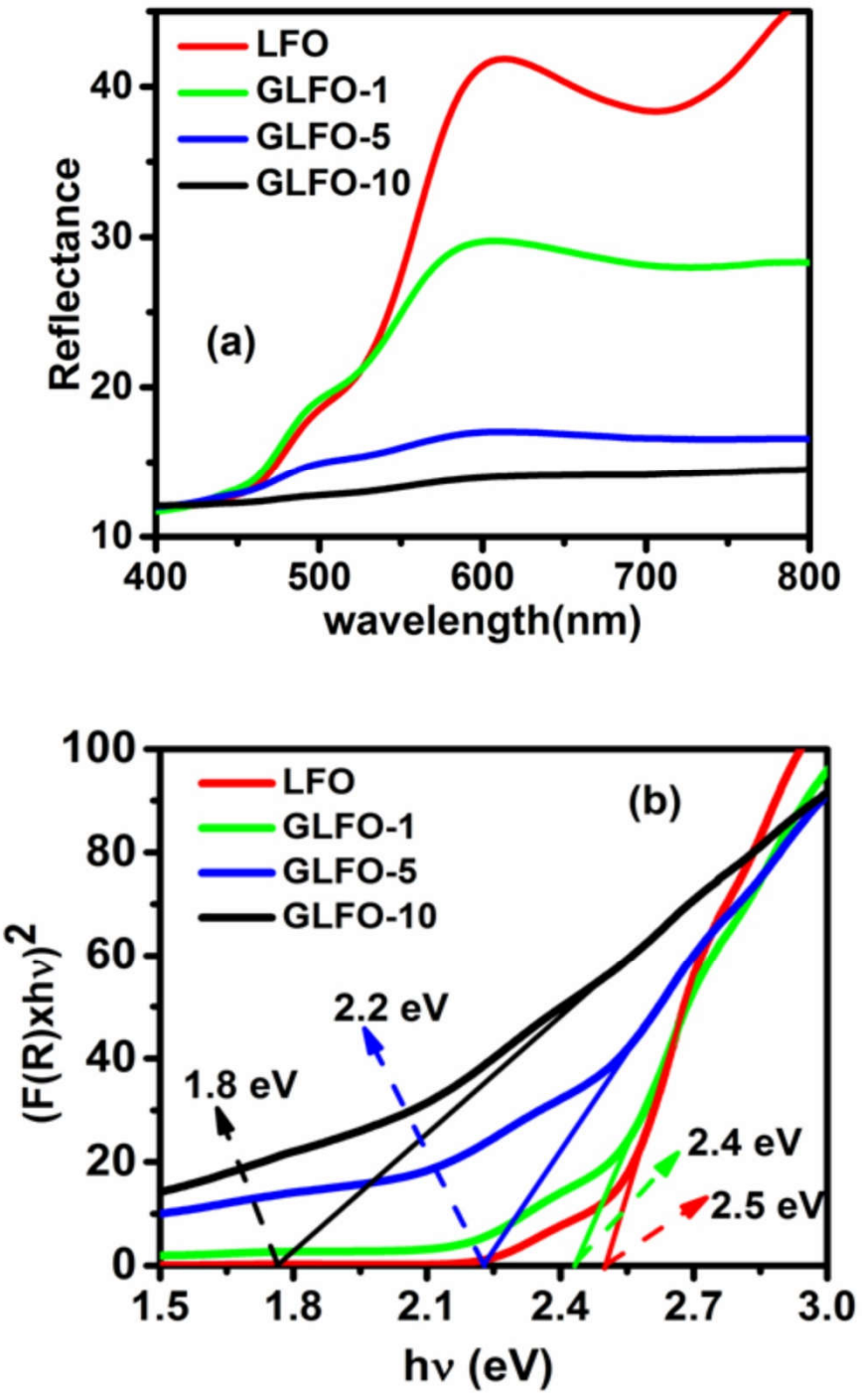

Fig. 5.5 (a) UV-Vis reflectance spectra of LFO, GLFO-1, GLFO-5, and GLFO-10 (b) Kubelka-Munk re-emission function for band gap calculation

The bandgap of the composites has been calculated using the modified Kubelka-Munk function, as shown in Fig. 5.5 (b). The direct band gap semiconductor LFO shows a value of 2.5eV from the plot. As the concentration of RGO increased, the bang gap value decreased from 2.5 to 1.8 eV. The strain on the crystal structure alters the overlapping of O(*2p*) and Fe(3d) orbitals which in turn changes the positions of valence band and conduction band of the GLFO composite [18]. In any case, the ratio of concentrations of RGO to LFO played a critical role in deciding the band gap [19]. It is to be noted that, the GLFO-10 has double the ratio of graphene with respect to GLFO-5. In addition, the difference of 0.4 eV in band gap between GLFO-5 and GLFO-10 might also be linked to the Fe_2O_3 levels. The reduction in band gap of GLFO composite can be understood in terms of defect bands that perturb the band structure in the form of a tail within the band gap. The tail is referred as Urbach tail and the corresponding energy value relates to the defect in the associated crystal structure [20]. Urbach energy is expressed by the formula

$$\alpha = \alpha_0 \ln\frac{E}{E_u}$$

Where E is the photon energy, E_u is the Urbach energy and α is the absorption coefficient. The *F(R)* (based on DRS model) Vs E (in eV) has been plotted for the calculation of E_u. Fig. 5.6 shows a straight line fit in the linear portion of the band gap of GLFO, and reciprocal of the slope of the fit gave E_u. The calculated value of band tailing energy for LFO, GLFO-1, GLFO-5, and GLFO-10 is given in Table 5.2. Higher E_u value for LFO originates from the non-stochiometric orthorhombic *pbnm* crystal structure, derived vacancy in lattice oxygen, and mixed oxidation state of the B-site metal cation. The Urbach energy increases with the concentration of RGO in the composite. The incorporated RGO creates added distortions in the crystal structure of LFO by

means of varying the lattice oxygen defects, resulting in generation of defect levels within the band gap. In order to understand more about the defect levels, fluorescence measurements were carried out.

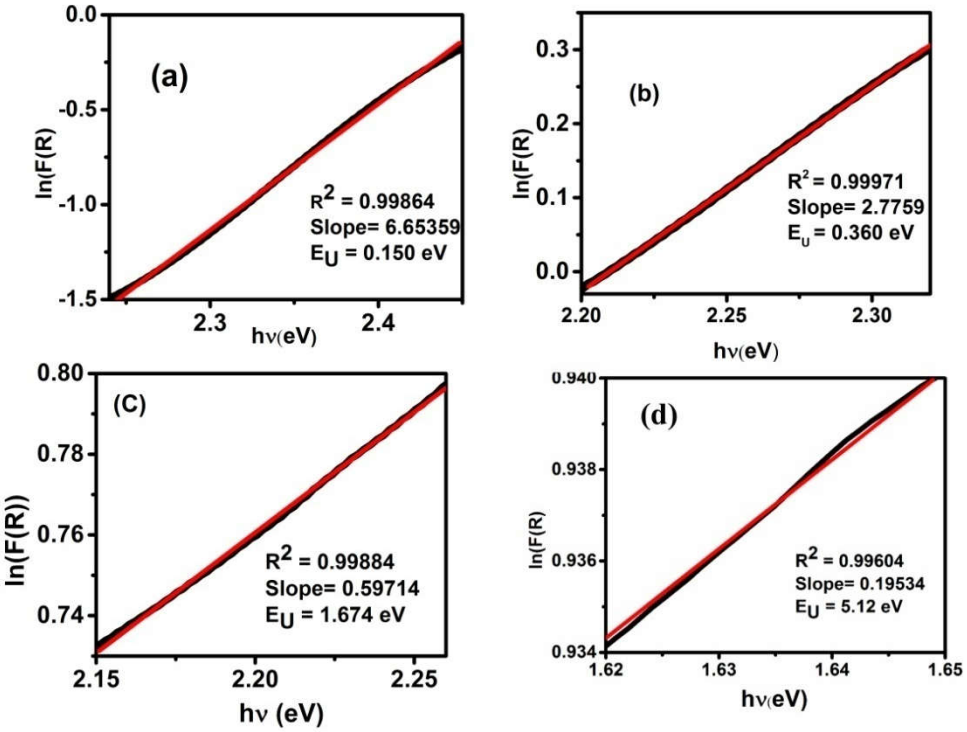

Fig. 5.6 Evaluation of Urbach energy for (a) LFO (b) GLFO-1 (c) GLFO-5 and (d) GLFO-10.

Table 5.2 Urbach energy values for LFO and GLFO composites

Sample	Urbach energy
LFO	0.150 eV
GLFO-1	0.360 eV
GLFO-5	1.67 eV
GLFO-10	5.12 eV

5.4.2 Fluorescence Studies

The fluorescence spectra of the samples are obtained at an excitation wavelength of 325 nm are shown in Fig. 5.7 (a). A broad peak centered at 450

nm is observed in the case of GO. In general, the broad FL peak arises due to the multiple components in the sample. The different oxygen functional groups serve as the fluorescent centers and produces a broad peak in the GO emission spectrum.

There are two types of emissions in GO related composites: (i) Radiation from the defect state leading to blue emission and (ii) the sp^2 cluster induced localised energy levels leading to longer wavelength (LW) emission representative of cluster size [21]. In the case of GLFO composites, the concentrations of different fluorophores present in RGO including LFO came into play.

In the case of LFO, the FL emission is influenced by the defect levels. F.H.Taylor theoretically predicted the defect formation energy corresponding to Fe^x_i neutral interstitials under the oxygen-deficient condition as 2.90 eV [22]. Here in the synthesized LFO, the peak at ~445 nm in the deconvoluted spectra corresponds to Fe neutral interstitial. The variation in the area of the 445 nm peak observed in GLFO composites originates from the fluctuation in Fe^{3+} oxidation state. It indicates the formation of more oxygen vacancies with defect centers as to maintain the stoichiometry of the crystal.

In Fig. 5.7 (a), the FL intensity of GLFO composites monotonically decreased with increasing concentration of RGO. It suggests a strong interaction between RGO and LFO [23]. In GLFO composites, the formation of heterojunctions lower the recombination probability of photogenerated carriers and it leads to a quenching effect in the emission spectrum.

The lower wavelength (LW) FL emissions of GLFO composites vary from 500 nm to 581 nm.These peaks are the result of the radiative recombination of e-h pairs localized in sp^2 clusters. The distribution of energy gap based on the size distribution of the sp^2 clusters leads to variations in LW

emissions [24]. The blue emissions arise due to the surface related structures and the wavelength centered at 450 nm in GO varies in GLFO composites. Synthesis technique has an important influence on the reduction of GO [25]. Hydrothermal synthesis was employed to functionalise the metal nanoparticle on the graphene sheet. It is reported that the hydrothermal synthesis produces smaller size clusters of RGO leading to a larger density of defect sites and therefore the sp^2 cluster size will have an impact on the current FL spectra [26].

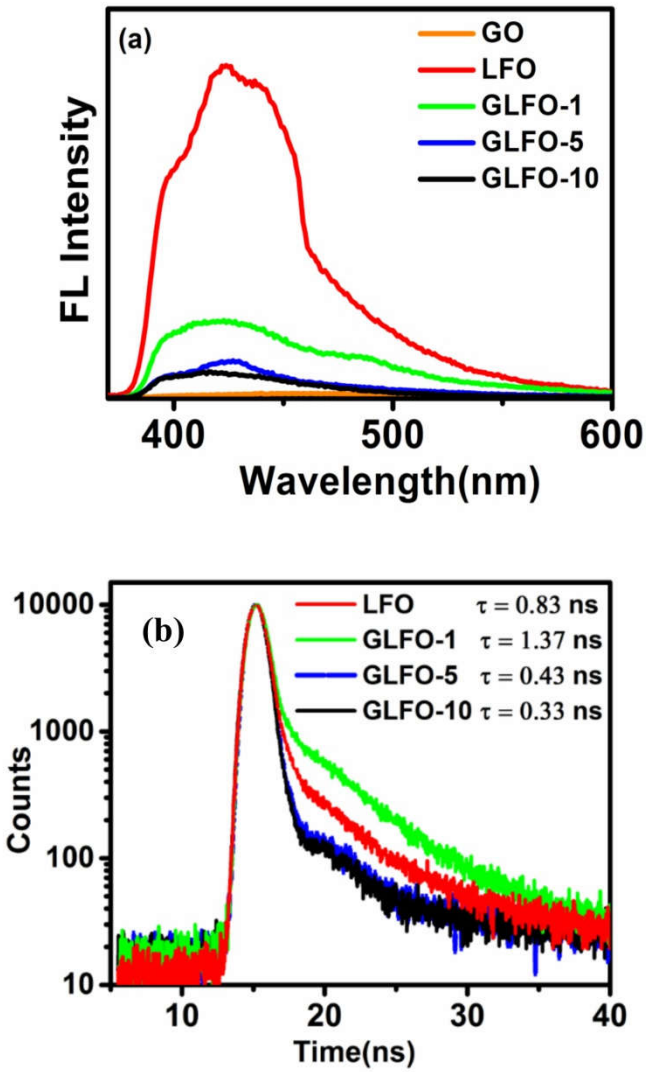

Fig. 5.7 (a) Fluorescence spectra of the entire composite (b) Lifetime curve of LFO, GLFO-1, GLFO-5, and GLFO-10

5.4.3 Lifetime Measurment

Time-resolved fluorescence spectroscopy is one of the powerful tools to probe the optical properties of the synthesised samples [27]. It provides an estimate on lifetime of the photogenerated carriers. The decay curve in Fig. 5.7 (b) was fitted with a triple exponential decay function and the corresponding average lifetimes obtained are given in Table 5.3. It is observed that the average lifetime of GLFO-1 is increased compared to LFO. The decrease in lifetime by increasing the interface can be attributed to the ultrafast decay of photoexcited charge carriers through the intermediated bands.

Table 5.3 Lifetime values of LFO and GLFO composites.

Sample	**Lifetime**
LFO	0.83 ns
GLFO-1	1.37 ns
GLFO-5	0.43 ns
GLFO-10	0.33 ns

5.4.4 Photocatalysis

Generally, the variation in FL intensity is one of the measures for the prediction of relative photocatalytic efficiency [28]. Here fluorescence intensity studies predict GLFO-10 having the lowest intensity as the most efficient photocatalyst. But the lifetime predicts GLFO-1 as efficient photocatalyst. In order to study this discrepancy, the photocatalytic ability of RGO/LFO was studied using the degradation of RhB.

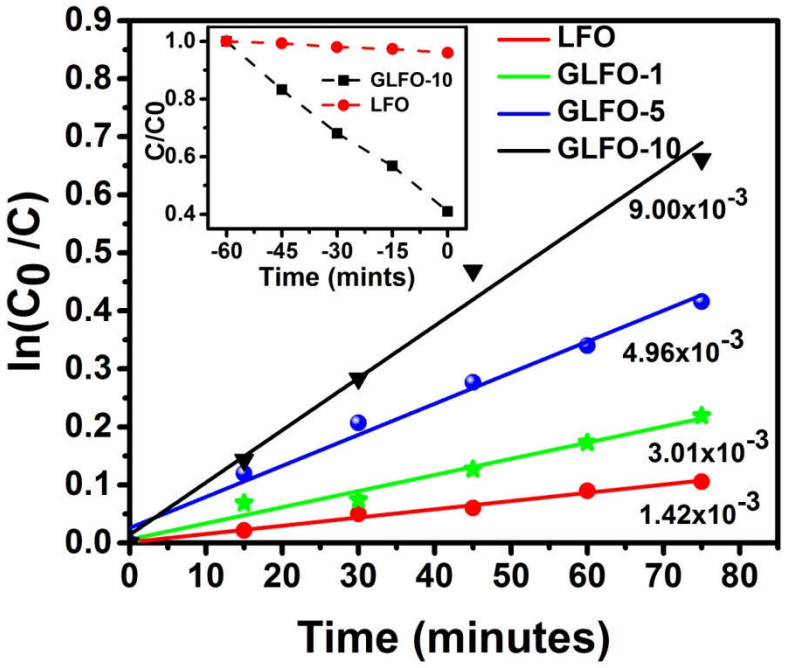

Fig. 5.8 Degradation rate of RhB with different GLFO composites (x10^{-3} s^{-1}). Inset: Adsorption during equilibration period.

The catalytic activity of the synthesised LFO is found to be low in comparison with GLFO composite. Fig. 5.8 shows the apparent rate constant of the composites. As we can see from the Table 5.4 the GLFO-10 shows the fastest degradation among the composites. Therefore, one can see that the photocatalytic activity followed the prediction based on fluorescence intensity. The disagreement with the lifetime measurements is explained on section 5.4.5.

Table 5.4 Photocatalytic rate constant of GLFO composites

Sample	Rate constant(x10^{-3})
LFO	1.42
GLFO-1	3.01
GLFO-5	4.96
GLFO-10	9.00

Among GLFO composites GLFO-10 has a higher concentration of GO to LFO. The presence of graphene aids photocatalytic activity in two ways: (1) Enhanced dye adsorption on the surface of RGO *via* π-π interaction. The increase in number of oxygen moieties in GLFO -10 increases the adsorption of dye on its surface. (2) RGO acts as an efficient support to adhere LFO nanoparticles such that it can effectively trap the photogenerated electrons and reduce the recombination of excitons [29]. This aspect of RGO as an electron trapper is clearly demonstrated by the relative fluorescence intensities (Fig. 5.7 (a)). Thus, one can clearly predict that GLFO-10 will have a higher activity than GLFO-5.

In order to find the mechanism of the photocatalytic ability of the GLFO composites, we have performed the reactive species test on GLFO -10 and the results are given in Fig. 5.9. Here P-benzoquinone was used as $O_2^{\cdot-}$ scavenger and Tert-butanol were used as $OH^{\cdot}$ scavenger. The effect of holes and electrons were investigated using EDTA (Ethylene diamine tetra acetic acid) and sodium sulfate respectively.

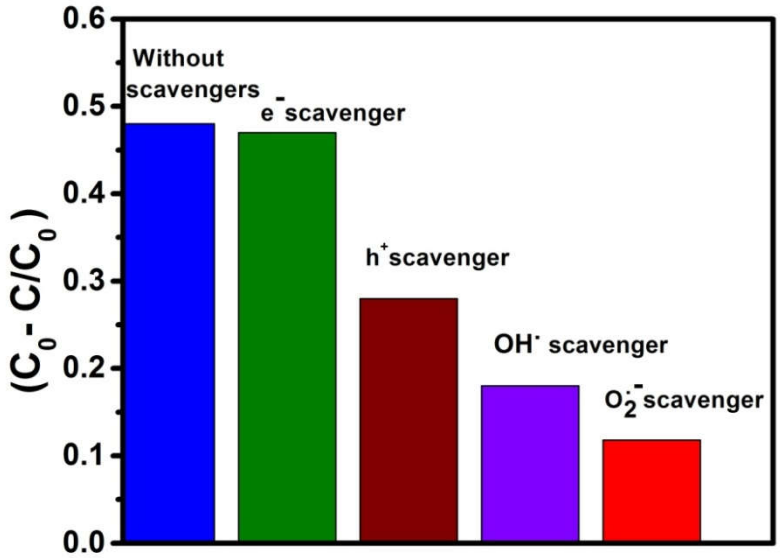

Fig. 5.9 Effect of reactive scavengers on the degradation activity of GLFO-10 photocatalyst towards RhB under Xe-arc lamp

Based on the reactive species test the possible mechanism for GLFO composite after illumination can be understood as follows:

Upon illumination, with the solar spectrum (Xe-arc lamp), the photoexcited electrons in the LFO reach the CB simultaneously creating holes in VB. Graphene act as an electron sink which traps the photoexcited electrons from LFO. Thus, graphene prevents the recombination of the e-h pair. The oxygen sites of RGO accept the electrons and undergo reduction reaction to form $O_2^{\cdot-}$. Ultrafast transportation of photogenerated electrons over the RGO sheet can directly reduce O_2 to produce $O_2^{\cdot-}$ radicals which lead to enhanced dye degradation [30]. The holes in the valence band directly take part in the degradation of dye. Similarly, hydroxyl radicals ($OH^{\cdot}$) can be created from superoxide radicals. The reactive species such as superoxide, hydroxyl, and holes are responsible for the degradation of RhB.

$$GLFO + h\upsilon \rightarrow RGO(e^-) + LFO_{VB}(h^+)$$

$$O_2 + e^- \rightarrow O_2^{\cdot-} \rightarrow \text{degrades the dye}$$

$$O_2^{\cdot-} + H_2O \rightarrow OH^- + OH^{\cdot}$$

$OH^{\cdot}/OH^-$ + RhB→ degrades the dye

Maria Magdalane *et al.* report that the reactive species necessary for the degradation of the organic pollutant on the catalytic surface is constant for a given light intensity, catalytic concentration and period of irradiation [31]. Here, within the mechanism, based on the origin of $O_2^{\cdot-}$ radicals, one can again assume that GLFO-10 with the highest concentration of RGO is having a better chance of formation of $O_2^{\cdot-}$ compared to GLFO-5. In addition, the increased amount of RGO provides more active sites to adsorb dye molecule on the surface of the nanocomposite resulting in an enhanced activity. We observed that nearly 60 % of the RhB got adsorbed onto the GLFO-10 during

the equilibration period (60 minutes in dark) whereas only 2 %, 5 %, and 19 % got adsorbed during dark in LFO and GLFO-1, GLFO-5 respectively. After the photocatalytic process, the solution is collected, centrifuged (4000 rpm for 30 mints), washed and dried at 60^0C. The recycle test showed that the efficiency of the GLFO-10 sample decreased from 50% in the first cycle to 12% within second cycle. It indicates that graphene can hold on to a sizable amount of dye as also previously reported by Subba Reddy *et al.* [32]. This aspect is also clear from the dark reaction plot shown in Fig. 5.8 (inset).

5.5 Summary of the Mechanism for Electron-Hole Pair Recombination in Graphene–LFO

The whole mechanism for electron-hole pair recombination in graphene–LFO nanocomposite and its impact in the photocatalytic activity can be understood as follows:

i) The size strain calculation shows that the orthorhombic perovskite has an inherited crystal distortion induced by the synthesis method. Among the samples, LFO shows the highest fluorescence emission intensity with an average lifetime of 0.83 ns. The RGO induced additional strain on LFO.

ii) The RGO can effectively act as an electron trapper in graphene nanocomposites. Therefore the occurrence of e-h recombination is reduced as RGO concentration increases. The corresponding reduction in FL intensity is noticed in Fig 5.7 (a).

iii) The order of lifetime of the nanocomposites is GLFO-1> GLFO-5> GLFO -10. In the case of the lifetime of the composites, the strain introduced by the RGO played a dominant role. As RGO concentration increased, the strain on the composite also increased (as observed in SSP). The strain led to the corresponding origin of intermediate band

tails which promoted radiation-less transitions of the photo excited electrons of LFO. The band tails made the e-h recombination faster and therefore smaller lifetime for excited charge carriers. It is to be noted that the RGO trapped electrons does not participate in the recombination responsible for lifetime calculation.

iv) Intriguingly, even though the GLFO-5 is having the highest strain, the GLFO-10 has the lowest lifetime. Between the GLFO-5 and GLFO-10, the strain in LFO is slightly relaxed with the formation of Fe_2O_3. But, the reduction in the concentration of band tails (strain induced) is compensated by the additional level of Fe_2O_3 in GLFO-10 promoting the faster recombination.

v) The order of photocatalytic rate in the samples is LFO < GLFO-1 < GLFO-5 < GLFO-10. The lower FL intensity (as in GLFO-10) and higher average lifetime (as in GLFO-1) constitute a good photocatalyst. But here, two critical features of RGO play a decisive role in deciding the order of photocatalytic reaction rate. (1) The electron trapping by RGO and (2) Adsorption of dye molecule on RGO. Both the factors together contribute to the highest removal of dye molecule with GLFO-10 having the highest concentration of RGO.

5.6 Conclusion

In summary, one-pot hydrothermal method is employed to disperse perovskite $LaFeO_3$ on the surface of RGO to form GLFO composites. The size-strain plot shows the highest strain for GLFO-5. Beyond GLFO-5, the increase in concentration of RGO causes reduction in strain by forming an additional phase of Fe_2O_3. Optical studies using UV-Vis DRS and steady state fluorescence spectra shows decrease in band gap and fluorescence intensity of the composite with increasing RGO concentration. The predominant

intermediate states originated from the influence of RGO induced strain promote faster radiationless transitions of the excited electrons to the ground state of LFO. The order of photocatalytic activity rate in the samples is LFO< GLFO-1< GLFO-5 < GLFO-10. The critical features of RGO played a decisive role in the case of lifetime and photocatalytic activity. The electron trapping and adsorption of dye molecule by RGO together contribute to the highest removal of dye molecule in GLFO composites. A detailed study on life time of charge carriers including the ultrafast transient absorption in GLFO composites might open potential applications in the field of solar cells and optoelectronics.

5.7 References

[1] M.V. Kovalenko, L. Protesescu, M.I. Bodnarchuk, Science. 358 (2017) 745–750.

[2] S. Seth, N. Mondal, S. Patra, A. Samanta, The Journal of Physical Chemistry Letters. 7 (2016) 266–271.

[3] Y. Mao, S. Banerjee, S.S. Wong, Journal of the American Chemical Society. 125 (2003) 15718–15719.

[4] C. Maria Magdalane, K. Kaviyarasu, A. Raja, M.V. Arularasu *et al.*, Journal of Photochemistry and Photobiology B: Biology. 185 (2018) 275–282.

[5] K. Kombaiah, J.J. Vijaya, L.J. Kennedy, K. Kaviyarasu, Materials Chemistry and Physics. 221 (2019) 11–28.

[6] J.R. Hayes, A.P. Grosvenor, Journal of Physics: Condensed Matter. 23 (2011) 465502.

[7] S. Thirumalairajan, K. Girija, I. Ganesh, D. Mangalaraj *et al.*, Chemical Engineering Journal. 209 (2012) 420–428.

[8] J. Qin, Z. Cui, X. Yang, S. Zhu, Z. Li, Y. Liang, Sensors and Actuators B: Chemical. 209 (2015) 706–713.

[9] Y. Ye, H. Yang, R. Li, X. Wang, Journal of Sol-Gel Science and Technology. 82 (2017) 509–518.

[10] C. Bhandari, S. Satpathy, Journal of Physics and Chemistry of Solids. (2017) 265-269.

[11] Z. Ma, K. Wu, R. Sa, K. Ding, Q. Li, AIP Advances. 2 (2012) 032170-6.

[12] R. Yogamalar, R. Srinivasan, A. Vinu, K. Ariga, A.C. Bose, Solid State Communications. 149 (2009) 1919–1923.

[13] A. Khorsand Zak, W.H. Abd. Majid, M.E. Abrishami, R. Yousefi, Solid State Sciences. 13 (2011) 251–256.

[14] T.M.K. Thandavan, S.M.A. Gani, C.S. Wong, R.M. Nor, Journal of Non destructive Evaluation. 34 (2015).

[15] O. Opuchovic, A. Kareiva, Ceramics International. 41 (2015) 4504–4513.

[16] L. Liu, A. Han, M. Ye, M. Zhao, Solar Energy Materials and Solar Cells. 132 (2015) 377–384.

[17] D.M. Sherman, T.D. Waite, American Mineralogist. 70 (1985) 1262-1269.

[18] G. Kotnana, S.N. Jammalamadaka, Journal of Applied Physics. 118 (2015) 124101.

[19] S. Acharya, D.K. Padhi, K.M. Parida, V, Catalysis Today. (2017).

[20] S. Paul, A. Choudhury, Applied Nanoscience. 4 (2014) 839–847.

[21] Z. Gan, H. Xu, Y. Hao, Nanoscale. 8 (2016) 7794–7807.

[22] F.H. Taylor, J. Buckeridge, C.R.A. Catlow, D Chemistry of Materials. 28 (2016) 8210–8220.

[23] X. Wen, P. Yu, Y.R. Toh, Y.C. Lee, K.-Y. Huang, *et al.*, Journal of Material Chemistry C. 2 (2014) 3826–3834.

[24] S. Vempati, T. Uyar, Physical Chemistry Chemical Physics . 16 (2014) 21183–21203.

[25] Z. Gan, S. Xiong, X. Wu, T. Xu *et al.*, Advanced Optical Materials. 1 (2013) 926–932.

[26] D. Pan, J. Zhang, Z. Li, M. Wu, Advanced Materials. 22 (2010) 734–738.

[27] A.S. Patel, P. Mishra, P.K. Kanaujia, S.S. Husain *et al.*, RSC Advances. 7 (2017) 26250–26255.

[28] Y. Wang, W. Wang, H. Mao, Y. Lu, J. Lu, J. Huang *et al.*, ACS Applied Materials & Interfaces. 6 (2014) 12698–12706.

[29] A.R. Nanakkal, L.K. Alexander, Journal of Materials Science. 52 (2017) 7997–8006.

[30] R. Vinoth, P. Karthik, C. Muthamizhchelvan, B. Neppolian, M. Ashokkumar, Physical Chemistry Chemical Physics. 18 (2016) 5179–5191.

[31] C. Maria Magdalane, K. Kaviyarasu, N. Matinise *et al.*, South African Journal of Chemical Engineering. 26 (2018) 49–60.

[32] Y. Subba Reddy, C. Maria Magdalane, K. Kaviyarasu *et al.*, Journal of Physics and Chemistry of Solids. 123 (2018) 43–51.

CHAPTER 6

Reduced Graphene Oxide–Perovskite Nanocomposite: A Prospective Material for Electrochemical Sensing Applications

In this chapter, electrochemical sensor as a potential application of graphene perovskite interface is explored. The cross sensitivity analysis shows GLFO could be a practical electrochemical sensor for the detection of H_2O_2. As a part of electrochemical analysis charge-discharge characteristics of GLFO is also investigated

6.1 Introduction

Perovskite with high chemical, thermal and mechanical stability as well as multiple functionalities is useful in many fields ranging from catalysis, gas separation to solar cells and high temperature sensors. The flexibility in electronic structures, distribution of electronic states and crystal geometry along with chemical adaptability of perovskite, facilitate to design an active catalyst with selectivity, stability, and high surface area for many of the chemical reactions [1]. One of the members in perovskite family, $LaFeO_3$ (LFO) shows good electrochemical properties [2,3]. But some of the inherent properties like low intrinsic conductivity limit its application in many fields. Also the aggregation of LFO particles during charge–discharge process decreases active surface area between the electrode and electrolyte and consequently restrains the electrochemical activity [4]. In order to improve the functionality of the perovskite, many methods have been adopted, in which one of the methods is partial substitution of metal cation with lower oxidation state at *A* and *B* site [5,6]. The manipulation of cationic and oxygen deficiency can lead to formation of new compound with tuned structural, catalytic as well as electronic properties. The other mechanism is modifying it with highly electrochemically active materials [7]. The difficulty associated with the substitution doping is that it changes the composition of the parent compound and converts it into a new class of materials. An emerging area of intensive research is on the development of composites of complex oxides to create new material interfaces and modulate the functionality of each component.

Controlled reduction of graphene oxide (RGO) provides functional sites which trigger the adsorption of the molecules on the surfaces and the restacked π-π interaction facilitates the increase in conductivity of the composites. The planar nature of the reduced graphene oxide along with the

combination of other functional nanomaterials provides opportunities for enhanced electrochemical sensing and capacitive activity [8,9].

It is already noted in Chapter 4 that inclusion of graphene on perovskite material can change the electrochemical conductance of the composite in acetate buffer for example see in Fig. 4.5 (a), this open up a path way for the applications of GLFO composite as an electrochemical sensor. So in this chapter, the utility of GLFO nanocomposite as an electrochemical sensor is investigated.

Electrochemical sensing action of the prepared samples were analysed by taking H_2O_2 as the model analyte. Hydrogen peroxide is an important biological material, which is involved in many intercellular pathways, biological as well as chemical reactions [10]. There are several methods proposed for the detection of H_2O_2 using enzymatic and non enzymatic materials [11]. Electrochemical sensing is used as one of the rapid response and sensitive technique for the detection of H_2O_2 sensors. Amelioration of the electrochemical non enzymatic sensing activity of individual graphene oxide and LFO towards H_2O_2 is made possible by utilising the interfacing properties of reduced graphene oxide by incorporating it with perovskite LFO.

6.2 Experimental Methods:

Perovskite modified RGO was prepared by hydrothermal method. A detailed description about the synthesis of graphene perovskite nanocomposite is given in chapter-2. The RGO varied composites were named as GLFO-1, GLFO-5 and GLFO-10 with concentration of GO to LFO is 1:10, 5:10, and 10:10 respectively.

Electrochemical measurements were carried out using “Biologic work station” with three electrode system. Pt and Ag/AgCl were used as counter and reference electrodes respectively. Further details of the equipment were

already discussed in section 2.6. The working electrode was prepared by drop casting 5 µl (2 mg/1ml) solution of the graphene nanocomposite on the surface of the electrode. In acetate buffer medium (0.1M), different concentrations of H_2O_2 were added successively and the current response with respect to time was noted.

6.3 Result and Discussion:

The synthesised samples were tested for phase purity and detailed structural evaluation using XRD, Rietveld refinement and Raman spectra. The detailed analysis was already given in Chapter 4 sections 4.3.1 and 4.3.2.

6.3.1 Electrochemical Detection of H_2O_2

In order to evaluate the electrochemical sensing activity of Graphene–perovskite nanocomposite for non-enzymatic detection of H_2O_2, the electrochemical amperometry technique was employed. The current vs. time graph as shown in Fig. 6.1 (a) shows significant response in current to successive addition of H_2O_2 into the acetate buffer (0.1M). The incorporation of RGO into the metal oxide framework enhances the current as well as the sensing activity. Expectedly, this enhancement might be due to the increase in defect density, electrical conductivity and surface area of the graphene nanocomposite. Fig. 6.1 (b) shows the variation in sensing action of the composite with respect to the RGO concentration. Here, GLFO-5 shows a superior sensing activity similar in nature with the electrochemical conductance study reported on ammonium solution in Chapter-4. Therefore, further studies were carried out on GLFO-5 sample.

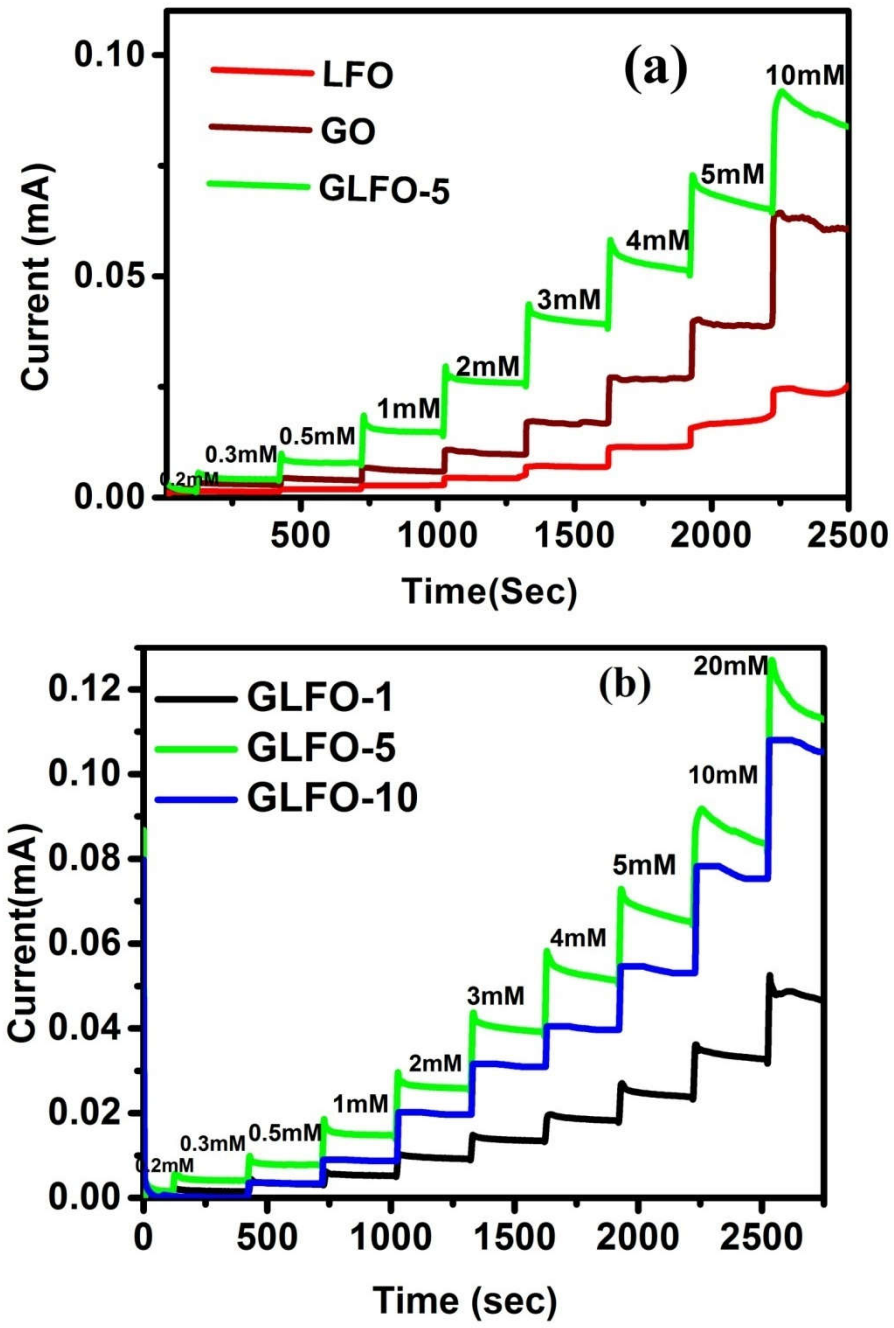

Fig. 6.1 Chronoamperometry studies on (a) GO, LFO and GLFO-5 (b) comparison between GLFO-1, GLFO-5 and GLFO-10

Experiments were carried out to measure the range, detection limit and sensitivity of the hybrid GLFO-5 electrode. To quantify the electrocatalytic ability, current response of GLFO-5 to the varying concentration of analyte is plotted in Fig. 6.2. As inferred from the figure, the linear range of detection for GLFO-5 is from 0.005 mM to 5 mM.

The detection limit of the composite is calculated using the equation $LOD = \frac{3\sigma}{slope}$ and $LOQ = \frac{10\sigma}{slope}$ where σ is the standard deviation of electrode without the analyte. The obtained value for lower detection limit is 28 μM and from the slope of calibration curve, the sensitivity of the electrode is estimated to be 94 μM.

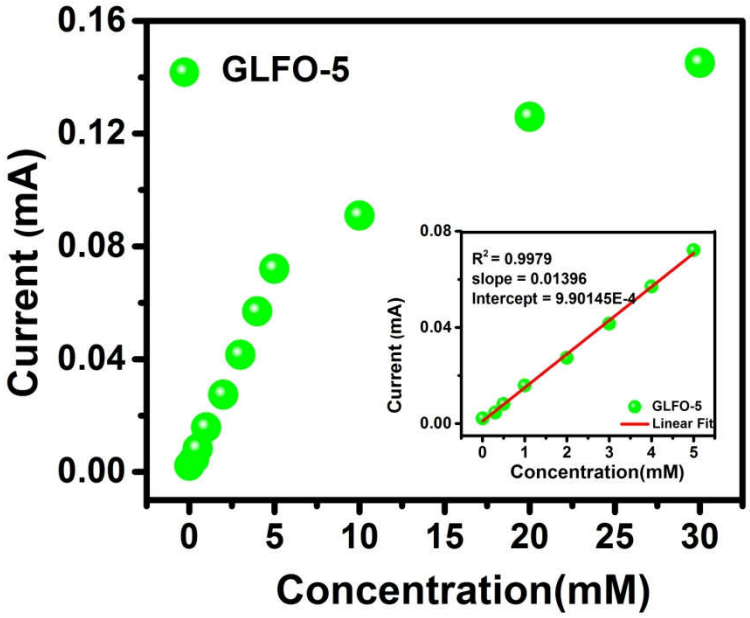

Fig. 6.2 Variation of current with concentration of H_2O_2 for GLFO-5. The inset shows Calibration plot for the range 0.005 mM -5 mM

6.3.2 Cross Sensitivity Analysis:

In the case of practical chemical sensors one of the important parameters is selectivity of the material. The cross sensitivity of the nanocomposite was examined in presence of interference material of H_2O_2. Fig. 6.3 shows the

amperometry response of the GLFO-5 electrode towards interference electroactive materials like Ascorbic acid, Urea, Glucose etc. In the experiment 5mM of H_2O_2 was first added and then subsequently ascorbic acid, glucose and urea were added. It can be noticed that the addition of the compounds other than H_2O_2 could not exhibit any significant current response in the spectrum; on the contrary the addition of H_2O_2 exhibits a significant response in current. The selectivity of the GLFO-5 towards non enzymatic detection of H_2O_2 is remarkable and it proves the application of GLFO composite as an excellent electrochemical sensor.

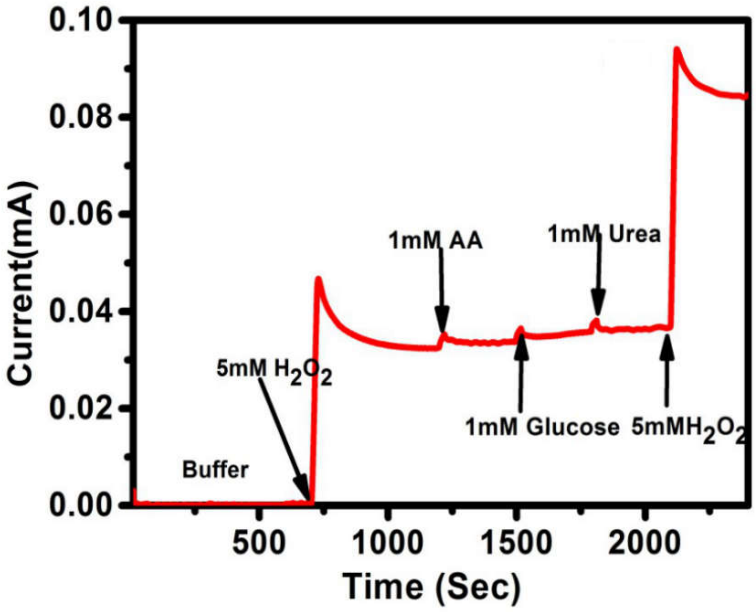

Fig. 6.3 Cross sensitivity studies on GLFO-5 with Ascorbic acid (AA), glucose and Urea

6.3.3 Charge–Discharge Characteristics:

The Graphene-LFO perovskite has been studied further by analysing the charge-discharge characteristics at a constant current. Fig. 6.4 (a) shows the CV curve of GLFO-5 at different scan rate within the potential window -0.1 to 0.4 volts. The specific capacitance of the material is calculated using the equation

$$C = \frac{\int IdV}{vmV}$$

Where I is the current density, v is the scan rate, m is the mass of the sample and V is the potential window used. Fig. 6.4 (b) shows the specific capacitance of GLFO-5 at different scan rates from 20 to 100mV/s. It can be observed that the capacitance decreases with increase in scan rate. This is because of the insufficient time for the diffusion of the ions and adsorption in the reactive sites [12].

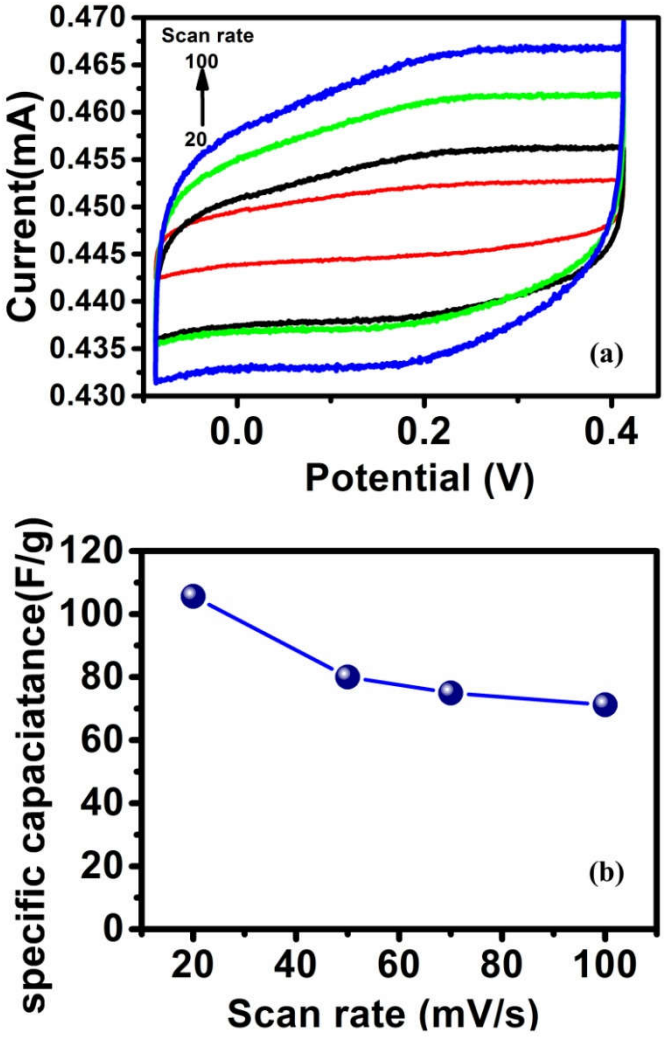

Fig. 6.4 (a) CV curve of GLFO-5 with a box range -0.1 V to 0.4 V range (b) Specific capacitance variation with respect to the scan rate

The galvanostatic charge-discharge curve of the material has been carried out at a constant current density and it is shown in Fig. 6.5 (a). The GLFO nanocomposites exhibit an asymmetric charge-discharge curve with sudden discharge. The charging time for GLFO-5 is 175 sec; whereas quite interestingly the discharging time is just 19.5 sec.

Among the charge - discharge curves of GLFO nanocomposite, GLFO-5 shows an enhanced activity. This is in tune with the result obtained in the amperometry studies of the nanocomposites. The impedance analysis (EIS) was used to investigate the internal resistance of the device (Fig. 6.5 (b)). The inner resistance was attributed to the ohmic resistance of the electrolyte and the charge transfer in the active material. From the Nyquist plot, equivalent series resistance evaluated is approximately 103, 100, 79.8, and 101 ohms for LFO, GLFO-1, GLFO-5, and GLFO-10 respectively as acquired from the intersection of the curve at the real-axis. The impedance is high of the order of 100 Ohm. This is responsible for the sudden discharge compared to charging in GLFO composite. This can be further reduced during cell fabrication by means of better electrolyte or by increasing the conductive additives in the electrodes.

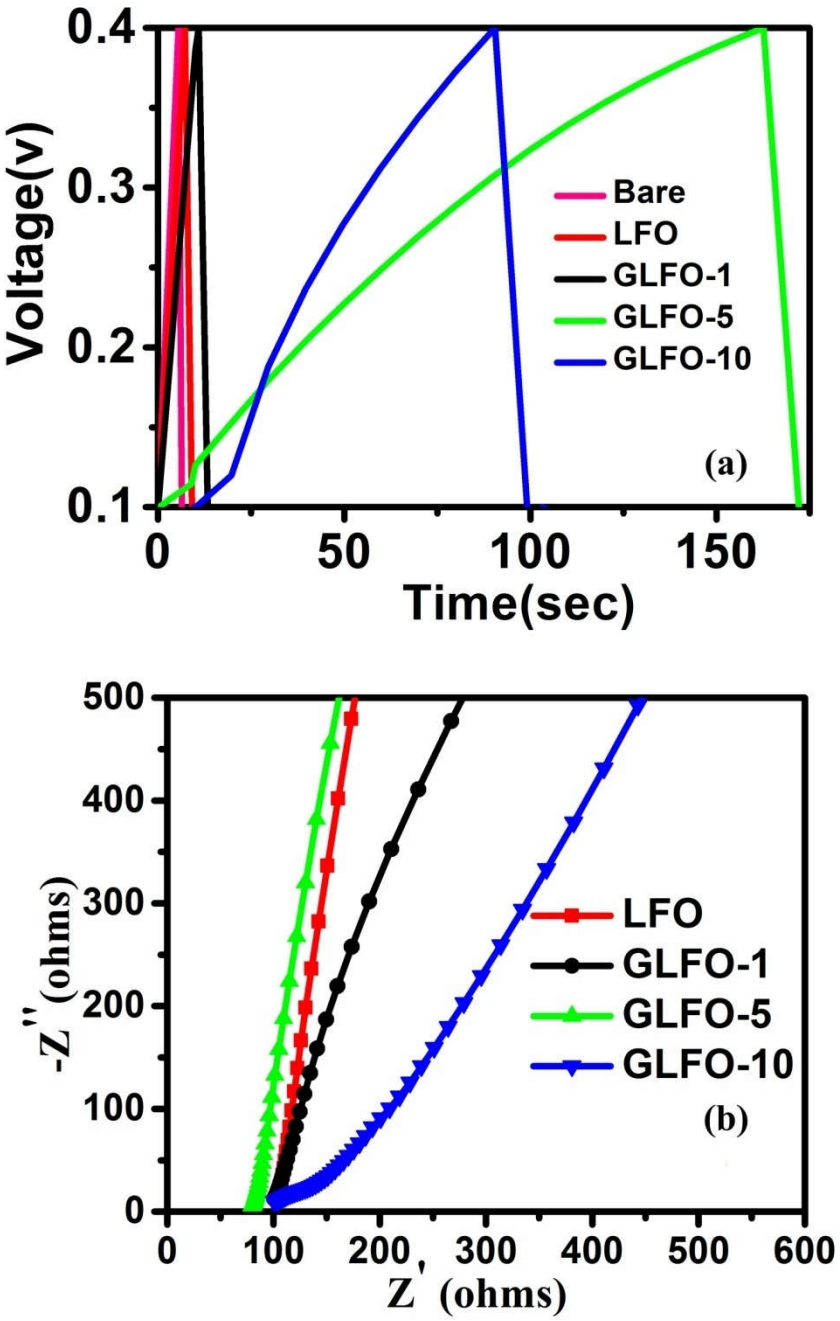

Fig. 6.5 (a) Galvanostatic charge-discharge curve of bare electrode, LFO, GLFO-1, GLFO-5, and GLFO-10 (b) EIS spectra of graphene nanocomposite

Synergistic effect between GO and LFO enables the compound GLFO-5 to show superior activity among other graphene LFO nanocomposite. Here the enhanced electrochemical activity of the as

mentioned composite is based on the interface effect between graphene and LFO. As we have discussed in Chapter 4, the composite GLFO-5 has a higher structural distortion due to the flacutation in the stable oxidation state of iron, which implement the insertion of oxygen ions from GO or creating oxygen vacancies in the crystal structure. Creation of defects changes the surface nature of the crystal and hence leads to the variation in electrochemical properties.

6.4 Conclusion

Relation between the distortion induced by reduced graphene oxide on perovskite LFO and the electrochemical activity has been investigated. An optimum concentration of GO to LFO changes the surface nature of the composite in such a way that the electrochemical activity of graphene perovskite nanocomposite is enhanced and shows a maximum. The sensing activity of GLFO composite towards H_2O_2 shows that it can act as good non enzymatic electrochemical sensor with good selectivity among interference materials. The galvanostatic charge discharge characteristics also show the variation which is in tune with the result obtained in the amperometry studies of the nanocomposites. The variation in defect density induced by the distortion varies the surface nature and electrochemical activity of GLFO composite.

6.5 References

[1] J. Hwang, R.R. Rao, L. Giordano *et al.*, Science. 358 (2017) 751–756.

[2] M. Lebid, M. Omari,Arabian Journal for Science and Engineering. 39 (2014) 147–152.

[3] N. Arjun, G.T. Pan, T.C.K. Yang, Results in Physics. 7 (2017) 920–926.

[4] Y. Yuan, Z. Dong, Y. Li, Progress in Natural Science: Materials International. 27 (2017) 88–92.

[5] G. Deng, Y. Chen, M. Tao, Electrochimica Acta. 54 (2009) 3910–3914.

[6] A. Benali, S. Azizi, M. Bejar, Ceramics International. 40 (2014) 14367–14373.

[7] Y. Pei, Y. Li, J.Y. Che, International Journal of Hydrogen Energy. 40 (2015) 8742–8749.

[8] D. Zheng, H. Hu, X. Liu, Current Opinion in Colloid & Interface Science. 20 (2015) 383–405.

[9] M.A. Pope, C. Punckt, I.A. Aksay,The Journal of Physical Chemistry C. 115 (2011) 20326–20334.

[10] Z. Yu, H. Li, X. Zhang *et al.*, Talanta. 144 (2015) 1–5.

[11] F. Xu, Y. Sun, Y. Zhang, Electrochemistry Communications. 13 (2011) 1131–1134.

[12] M. Sreejesh, N.M. Huang, H.S. Nagaraja, Electrochimica Acta. 160 (2015) 94–99.

CHAPTER 7

Overall Summary and Future Works

This chapter discusses overall summary of the thesis based on the four main objectives and future perspective of this work.

7.1 Overall Summary

The work discussed in the thesis entitled "Studies on Graphene-Perovskite $LaFeO_3$ Interface" aimed to utilize the amazing environment offered by graphene interface to tune the properties of a perovskite material and understand the mechanism of the interaction in detail. The thesis work is centered on the four main objectives as mentioned in Chapter 1. The objectives were centred on the behaviour driven by graphene-perovskite interface.

In order to study the mechanism of interaction between graphene and metal oxide, graphene perovskite nanocomposites were fabricated. The dispersing phase on the graphene surface was taken as $LaFeO_3$ or its derivatives. The partial substitution at *B* site of ABO_3 were done with two different elements Al and Cr. Varying concentration of graphene perovskite nanocomposites were synthesised using hydrothermal method- a green channel route for the effective functionalisation and reduction of graphene oxide. The structural characterisation using XRD gave the primary information about the linkage between graphene and the perovskite. The anchoring of dispersed phase of Lanthnaum based perovskite (*viz.* $LaFeO_3$, $LaFe_{0.8}Al_{0.2}O_3$, $LaFe_{0.8}Cr_{0.2}O_3$) on graphene sheets was imaged by FESEM analysis. On further analysis with Raman spectroscopy the peak shift as well as broadening of the peaks confirmed the effective functionalisation between graphene matrix and dispersing phase of Lanthanum based perovskite.

As a model compound this thesis attempts to analyze in detail the interfacing effect of Graphene-$LaFeO_3$ nanocomposite. The structural deviations of LFO were quantified with the help of Rietveld refinement analysis and it indicated that the nanocomposite with 5:10 ratio of GO to LFO (GLFO-5) shows higher deviation compared to LFO. The effect of distortion was demonstrated using electrochemical sensing with ammonium in acetate

buffer. An optimum current response was obtained for GLFO-5 sample. The recreated structure showed an enhanced variation in bond length and bond angle for GLFO-5 sample. An effective octahedral tilting indicated that graphene could induce distortion in the crystal structure of perovskite LFO. To study the detailed mechanism of interaction of graphene with LFO through the interface, XPS spectrum of the composite was analysed. The deconvoluted spectra of Fe (*2p*) showed a variation in the oxidation state of *B* site atom in LFO. The in depth analysis of the oxygen peak in XPS quantified the percentage of lattice and non-lattice oxygen associated with the GLFO nanocomposite. The increase in the concentration of RGO reduced the concentration of Fe^{2+}. The ratio of non-lattice oxygen to the lattice oxygen showed an increase with RGO concentration. This increase is attributed to the oxygen offered by the functional groups of RGO. Beyond GLFO-5, the perovskite lattice assumed to be reluctant to accommodate more Fe^{3+} ions in the lattice. This was indicated by an additional phase of Fe_2O_3 in the XRD spectrum of GLFO-10 composite. The variation in the oxidation state of B site atom and the presence of non-lattice oxygen changed the bond covalency associated with LFO. This imparts perturbation to the crystal structure and associated electrochemical conductance. The outcome of this study proves graphene can be an effective non-invasive tool to control the structural distortion in metal oxides.

This work includes a study on the effect of strain induced by graphene interface on the optical properties of perovskite LFO. The strain associated with the GLFO composite was investigated using size-strain plot. Among GLFO composite GLFO-5 showed an enhanced strain. The optical band gap of GLFO composite was evaluated using UV-Vis DRS data. The decrease in optical band gap of the GLFO composite was explained on the basis of band tailing energy. In order to study the defect levels and the resultant band tailing energy, the fluorescence steady state emission spectra of the LFO and GLFO

were carried out. Increase in concentration of RGO monotonically decreased the FL intensity in GLFO composite. The lifetime measurement showed a higher value for GLFO-1 compared to all other composites. The disagreement between FL intensity and lifetime value was explained on the basis of radiationless transitions mediated by intermediate bands associated with RGO concentration. In order to analyse the interface induced effect on photoexcited carriers, the photocatalytic efficiency of GLFO composites were tested. In the photocatalytic degradation of Rhodamine B (RhB) dye solution, GLFO-10 showed an enhanced activity. The effect of graphene interface as an electron trapper of photoexcited charge carriers as well as the medium for adsorption of dye on the surface resulted in the best photocatalytic degradation rate for GLFO-10 compared to other GLFO composites. The role of graphene interfaces on the photocatalytic efficiency of GLFO composite was explained on the basis of reactive species analysis and recycle test. This study proved that using graphene interface, the inherent fluorescence properties as well as the photocatalytic activity of perovskite could be modified.

As an application, the electrochemical sensing activity of the composite was analysed using H_2O_2 as the analayte. The sensing activity of GLFO composite towards H_2O_2 showed that it could act as a good non enzymatic electrochemical sensor with good selectivity in between interference materials such as Ascorbic acid, Urea, and Glucose. As a part of the electrochemical analysis, charge-discharge characteristics of the sample were evaluated. It also showed an enhanced activity for GLFO-5 but with sudden discharge characteristic. The higher internal resistance between the electrode and electrolyte resulted in the asymmetric behaviour observed in the GLFO composite.

This work investigated the effect of interface created by graphene platform on the properties of perovskite nanomaterials. Graphene acted as a

matrix over which the perovskite metal oxide is effectively anchored. To tune the properties of perovskite, the environment offered by graphene is successfully utilised. The mechanism of interaction of graphene and metal oxide revealed that graphene can change the bond covalency associated with the metal-anion bond leading to distortion in the crystal structure. Graphene created strain in the crystal geometry which is an outcome of distortion. The concentration of graphene in terms of intermediate bands influenced the lifetime of the charge carriers in the metal oxide.

This work added one more dimensionality to the application of graphene- as an effective tool to control the distortion of the metal oxide associated with it. This study also proves that electrochemical properties can be used as an indicator for the distortion properties connected with the metal oxide.

7.2 Future Scope

It is very clear that the environment offered by graphene can effectively tune the properties of a perovskite material. So the studies on graphene induced distortions can be extended to other metal complexes like spinels, garnets etc. to tune the material for functional applications.

Detailed theoretical analysis is needed for the graphene induced distortions in perovskite nanocomposites such that one can predict the exact point up to which the crystal can be stable and retains the basic properties of the parent compound without forming an additional phase. A detailed study by Mossbauer spectra will give more information regarding the crystal distortion associated with $LaFeO_3$.

Detailed study on the nature of variation in overlapping between the orbitals of metal cations and anions will help to improve the conductance and optical properties of the composite.

Moreover, this study deals with the lanthanum orthoferrite perovskite, it can be extended to other group members in rare-earth orthoferrites as well as other transition metal oxides. This could underline and advance the main novel findings made in the thesis such as distortion in metal oxide induced by graphene.